Transport in complex driven systems

Miedema, D.M.

Publication date
2015
Document Version
Final published version

Transport in Complex Driven Systems

Daniël M. Miedema

Transport in Complex Driven Systems

ACADEMISCH PROEFSCHRIFT

ter verkrijging van de graad van doctor
aan de Universiteit van Amsterdam
op gezag van de Rector Magnificus
prof. dr. D. C. van den Boom
ten overstaan van een door het college voor promoties
ingestelde commissie,
in het openbaar te verdedigen in de Agnietenkapel
op woensdag 30 september 2015, te 10:00 uur.

door

Daniël Maria Miedema

geboren te Leiderdorp.

Promotiecommissie

Promotores:	Prof. dr. P. Schall
	Prof. dr. B. Nienhuis
Overige leden:	Prof. dr. D. Bonn
	Dr. R. Sprik
	Prof. dr. S. Woutersen
	Prof. dr. ir. E. J. G. Peterman
	Dr. A. S. de Wijn
	Prof. dr. A. Schadschneider

Faculteit der Natuurwetenschappen, Wiskunde en Informatica.

Cover design by Niels Peereboom.

ISBN: 978-94-6259-816-4

The author can be reached at:
dmmiedema@gmail.com

The research reported in this thesis was carried out at the Van der Waals-Zeeman Institute/Institute of Physics, University of Amsterdam. The work was part of the Complexity program of the Nederlandse Organisatie voor Wetenschappelijk Onderzoek (NWO).

Contents

1

Introduction

1.1 Driven far from equilibrium

All physical systems which are not subject to an external driving force tend to reach a state called thermodynamic equilibrium. At thermodynamic equilibrium, most macroscopic physical observables, like pressure and density, remain constant over time. Bodies adapt shape, exchange particles, give up energy and change position to reach equilibrium. According to the second law of thermodynamics, each of these processes only occurs if the free energy of the system goes down or likewise increases the entropy of the system plus its environment. Thermodynamic equilibrium corresponds to the state with minimum free energy and maximum total entropy. The second law of thermodynamics and the tendency to thermodynamic equilibrium are empirical findings which are thought to be universal. While this concept of equilibrium presents one of the major achievements of (thermal and statistical) physics, many systems in nature are, however, far from equilibrium [1].

Systems can simply be so big, Fig. 1.1(a), that the equilibration process takes a very long time. For other systems, equilibration times can be very long, because they are stuck in a local free energy minimum, Fig. 1.1(b), and only slow relaxation allows them to eventually reach the global minimum. Glasses (Fig. 1.1(c))

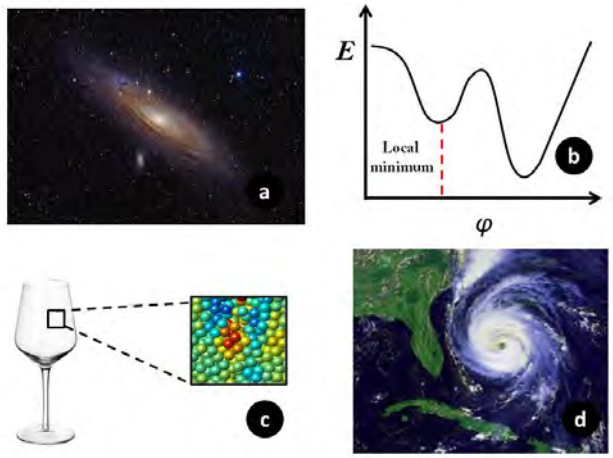

FIGURE 1.1: (a) Image of the Andromeda galaxy. (b) An energy landscape containing a local minimum. (c) A wine glass with the inset showing the disordered molecular structure of glassy materials. (d) Hurricane Fran approaching mainland United States.

are a well known example of a system trapped in a local free energy minimum. Rapidly cooling certain fluids below the melting point will form amorphous solids (glasses), instead of the crystalline ordered structures associated with the minimal free energy configuration. Structurally a glass is similar to a fluid, but the viscosity of a glass is many orders of magnitude larger than in the fluid phase [2]. Relaxation times become very long upon glass formation due to the increase of viscosity, trapping the liquid far from equilibrium, in a solid-like state.

The systems we discuss in this thesis are all subject to a driving force. The driving force constantly generates entropy and causes energy dissipation. Therefore, the standard techniques from equilibrium physics, based on free energy minimization and entropy maximization, are not applicable and new concepts are needed. Driven systems are not relaxing to equilibrium, but often develop towards a steady-state which is *far from equilibrium* by nature. Planet Earth is a beautiful example of a driven system. Rays of light from the sun continuously strike the Earth surface heating up the atmosphere, while an approximately equal amount of energy is radiated outward to space. The solar energy flux through the atmosphere gives rise to large scale transport of energy and matter, see Fig. 1.1(d).

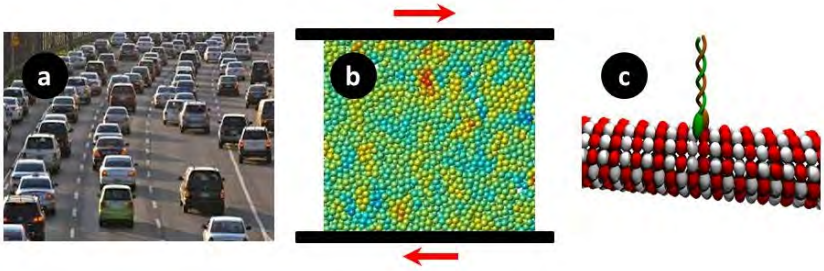

FIGURE 1.2: The driven systems studied in this thesis. (a) Highway traffic. (b) Sheared colloidal glass. (c) Molecular motor walking along the cytoskeleton.

In this thesis, we investigate transport in complex driven many-particle systems. The driven systems described in this thesis all develop towards a steady-state, but are diverse, including traffic such as daily encountered on highways, sheared colloidal glasses and molecular motor transport in biological cells, see Fig. 1.2. In all these cases, the driving force gives rise to collective motion of the constituent units, which we consider as transport through the system. Central questions are which steady-state arises, and how these macroscopic states result from the dynamic interactions of particles? Of particular interest are the density and current distributions in steady-state, which can be homogeneous or heterogeneous. We study how the steady-state, in which the probability distributions are time-independent, depends on the driving force, density, etc. We find common features of transport in these systems, and some indication of common underlying principles. Ultimately, this should contribute to a universal understanding of systems driven far from equilibrium.

1.2 States of matter

The physics far from equilibrium is diverse, complex and far from understood. No general framework exists to answer the above questions or how to find the steady-state distributions. The general approach to driven many-particle systems in this thesis is analogous to constructing a phase diagram for equilibrium systems.

Therefore, understanding the states of matter in equilibrium is useful to gain insight and draw analogies to driven systems. In everyday life we encounter three states of matter: solid, liquid and gas. The states of matter can be classified

according to their qualitative distinct properties on the macroscopic scale. A solid has an intrinsic shape. Liquids have no intrinsic shape, but do have a fixed volume. Gases are compressible, they neither have an intrinsic shape nor volume. Depending on the pressure and temperature a material is in a gas, liquid or solid phase. A typical phase diagram of a material in thermodynamic equilibrium is shown in Fig. 1.3. On the microscopic scale, molecules move past each other in gases and liquids; these phases are ergodic. As a result, the time-averaged structure of liquids and gases are both isotropic and homogeneous. The similarity between gases and liquids is reflected by the critical point, above which the distinction between gases and liquids can no longer be made. Molecules in a solid in thermodynamic equilibrium are fixed in a crystal structure. Solids and liquids remain distinct up to infinite pressure and temperature: no critical point exists for the transition between a liquid and a solid.

This equilibrium behavior can inspire classification schemes for systems far from equilibrium [3]. Traffic, which we will study in chapters 4 and 5, provides an intuitive example. At low density all cars are free flowing. Cars can change their speed and position freely in free flow. The freedom to change position and velocity without constraining other cars, makes the free-flow state analogous to liquids. Jams form at high densities due to velocity fluctuations and limited available space. Cars in a jam are highly constrained in their movement by the car in front.

Similarly to phase coexistence of equilibrium systems, jams and free flow can coexist in traffic. However, in contrast to equilibrium systems, where phase coexistence is not possible in one dimension, traffic exhibits phase coexistence even in one dimension [4, 5]. This highlights a striking difference with one-dimensional equilibrium systems. We will find that driven systems can develop intriguing non-equilibrium patterns, such as heterogeneous distributions of density and dynamics. The conditions for heterogeneous distributions of density or currents in a system, and the transition from homogeneous states, are of central interest in this thesis. In the next section we turn to the parameters that control the state of traffic and of the other driven systems.

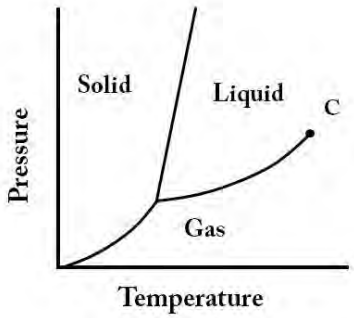

FIGURE 1.3: Phase diagram of a material in thermodynamic equilibrium. The critical point is denoted by a C.

1.3 Physical parameters of driven systems

In equilibrium systems the state is determined by external parameters. In Fig. 1.3, the parameters controlling the states gas, liquid or solid are the temperature and the pressure. These control parameters are of central importance in equilibrium systems. In driven systems, similarly there are parameters controlling the steady-state. Typical examples of such control parameters are the driving force, the particle density and particle interactions. While these parameters exist in some form in all systems we consider, their realization can be different in each system. Therefore, we briefly explain these parameters and their realization below.

Driving force: Obviously the driving force is an important parameter for driven systems - it is what makes them different from equilibrium systems. For sheared colloidal glasses, the driving force is the shear-force applied on the boundaries of the colloidal glass sample, see Fig. 1.2(b). In practice, we do not control the shear-force, but the imposed shear-rate. For models of cars and molecular motors, the intrinsic preference to go one way can be thought of as the driving force. The directional movement is powered by combustion of gasoline in cars and ATP hydrolization in molecular motors.

Interactions: The study of the driven systems discussed in this thesis include experiments and simulations. In the models used for simulations, all interactions between particles are approximated by hard-core interactions. That is, particles cannot occupy the same region of space, but do not interact otherwise. Also in

the experimental study of colloidal particles, which consist of hard plastic beads, so they cannot penetrate or overlap in space, hard-core interaction is probably a fair assumption. Similar restrictions exist in traffic, meaning that cars do not collide. Therefore, we use simulation models for traffic with hard-core interactions between cars. Molecular motors are complex nanometer-sized proteins, so that assuming strict hard-core interactions is probably an oversimplification, but nevertheless a useful first step in numerical studies of the collective behavior of these motors. We investigate the actual nature of the interactions between molecular motors experimentally in chapter 7.

Fluctuations: Colloidal particles are prone to thermal fluctuations. While the particles in a colloidal glass are frustrated by the surrounding particles leading to dynamic slow-down, thermal fluctuations still lead to relaxation and aging. In our colloidal shear experiments, we probe these relaxations by applying shear rates that compete with thermal relaxation times. In traffic, velocity fluctuations can result from drive style, interactions with other cars and a new song on the radio. A detailed description of all probabilistic processes is beyond the scope of most traffic models. Velocity fluctuations are typically assumed to be random, and can be described by a single stochastic parameter [6]. For molecular motors, the complex stepping process is largely unknown. In the experimental study on molecular motors described in chapter 7, we obtain insight into the stepping process as a function of crowding. Finally, in the simple model we use in chapter 8 to study the collective behavior of molecular motors, the only source of stochasticity is the random sequential order at which the particle dynamics is updated [7].

Density: Generally, the restricted space constrains the particles dynamically, and makes particle dynamics occur collectively. The particle density is thus a central parameter controlling particle dynamics and transport currents. In the colloidal experiments, the particle volume fraction, i.e. the fraction of volume occupied by particles with respect to the total volume, is of central importance. In the models for traffic and the models and experiments on molecular motors, density is a direct control parameter.

1.4 Steady-state currents and densities

In contrast to thermodynamic equilibrium, there is a current of mass or energy through driven systems; this steady-state current is an intrinsic property of driven systems. The steady-state current can be uniform throughout a system, or it can be heterogeneously distributed due to local structural or density differences. We explore the relation between the steady-state current and the particle distribution in this section, and use this relation between current and density to derive one from the other. The realization of this relation can be different for each system we study, we therefore discuss each system separately below.

Traffic: In traffic flow the formation and size of jams is of central interest [4, 8]. We analyze the conditions under which jams can be stable at long times in the steady-state of one-dimensional transport models, such as traffic models. The occurrence of stable jams in steady-state is rather detrimental: they can grow without bound, resulting in phase coexistence of free flowing and arrested traffic. By analyzing the steady-state inflow and outflow rates of jams we derive an analytic criterion that is necessary and sufficient for such dynamic phase coexistence to occur.

Sheared colloidal glasses: It is well-known that driven complex systems can exhibit flow heterogeneities [9, 10]. At low driving rates the flow is typically uniformly distributed throughout the material, while at higher driving rates flow heterogeneities can occur. We show that steady-state flow heterogeneities arise when the applied shear rate becomes faster than the intrinsic (relaxation) flow rate, which depends on particle density and structure. Such flow heterogeneities can organize in space to form spatially separated bands, known as shear bands.

Molecular motor transport along networks: In models of molecular motors moving along cytoskeletal networks, the steady-state current depends strongly on the structure of the network and the particle density [11]. At low particle densities, there is no jamming in the network, so each particle moves freely and contributes equally to the transport current. In this low-density regime, the structure of the network determines the distribution of particles among the network, and thus the distribution of currents. With increasing density the crossings in the network are the first to become jammed. For high global density, the current and density

distributions amongst the segments of the network in steady-state can be derived from the densities at the crossings [12].

1.5 Present thesis

This thesis presents a study of complex driven systems, consisting of many particles. The systems under study are simple models of highway traffic, experiments on sheared colloidal glasses and experiments and simulations of molecular motors moving along the cytoskeleton. In all cases, collective effects in transport arise, and we are interested in how the transport current and particle density organize in space. The widely different systems of our study will take us across dimensions: traffic is a 1D system, networks (quasi) 2D and colloidal glasses 3D. We will study particle dynamics in colloidal glasses and molecular motors experimentally using different microscopy techniques. Using simple models that specify the particle dynamics, we numerically study collective transport effects in molecular motors moving along networks and traffic on highways. In addition, we develop an analytical criterion for the occurrence of dynamic phase coexistence in one-dimensional transport models. This thesis aims to obtain detailed insight into the specific behavior of the mentioned systems, as well as find common principles of all these systems to contribute to a universal understanding of driven, far from equilibrium systems.

Chapter 2: We introduce the experimental systems and observation techniques in detail. As main technique we use optical microscopy, allowing us to follow the motion of colloidal particles and molecular motors. We use fluorescent labels to highlight the particles upon excitation with a laser. The molecular motors move along networks of microtubules - we give a short introduction to both and provide a detailed description of the setup and techniques used for this experiment. We give an introduction to colloids and their phase behavior. Details on the sample preparation of the colloidal glass, the shear cell used to apply the driving force and the data acquisition and processing to extract particle dynamics are given.

Chapter 3: This chapter is dedicated to introducing the (simulation) models. We introduce the models for simulating highway traffic and molecular motor motion along the cytoskeleton. We start with the Totally Asymmetric Simple Exclusion Process (TASEP), a paradigmatic model for driven transport in one-dimension.

The main results of TASEP are discussed. We introduce an extension to TASEP for traffic flow, the Nagel-Schreckenberg (NS) model. Finally, we extend the one-dimensional TASEP model to a network, to model the molecular motor motion along the cytoskeleton.

Chapter 4: Here we investigate the collective arrest in a traffic model in the limit of strong braking. We first establish an analogy between the arrest phenomena in traffic models and models used to study the dynamic slow-down of glasses. The glass models suggest a sharp transition in the limit where fluctuations disappear and motion freezes. We investigate the analogous limit in the NS traffic model - using tools developed to study the dynamics of glasses - and indeed observe a sharp transition similar to that in models of glasses. The sharp transition demarcates the onset of phase coexistence of moving and arrested traffic.

Chapter 5: Motivated by the sharp transition observed in chapter 4, we develop an analytical method to study when phase coexistence occurs. The analytical method is set up for one-dimensional transport models with a kinetic constraint and is based on flow rates in and out of traffic jams. We apply this method to the NS-model to analytically demonstrate that the sharp transition found in chapter 4 corresponds to the onset of phase coexistence. Moreover, we demonstrate that the condition under which the NS-model was studied in chapter 4 is the unique condition where phase coexistence occurs in this model.

Chapter 6: In this experimental chapter we study shear banding phenomena in a sheared colloidal glass. At low applied shear rates the colloidal glass homogeneously flows to accommodate the applied shear. Shearing faster than the intrinsic relaxation rate of the glass, splits the colloidal glass up in a slow and a fast moving shear band. We show that even this shear banding phenomenon can be understood as dynamic phase coexistence. Using a new dynamic order parameter, we characterize the dynamics in each band.

Chapter 7: In this experimental chapter, we investigate molecular motion along microtubules. We develop a new method to analyze the motion of molecular motors. The method is based on correlations of intensities from fluorescence microscopy data, and is designed to give a fast and accurate estimate of the dynamic parameters of molecular motors. Simultaneously, we measure the density of motors on a microtubule from the fluctuations in the spatially averaged intensities.

Using this method we study the velocity and run length of the microtubule specific molecular motors Kinesin-1, Kinesin-II and OSM-3 as a function of motor density. At high densities, the run length of all motors significantly decreases, while the velocity seems to depend only weakly on motor density. Crowding effects start to occur at surprisingly low densities for Kinesin-1, indicating long-ranged repulsive interactions. Kinesin-II and OSM-3 seem to have much smaller interaction lengths.

Chapter 8: In this chapter we numerically study the collective particle transport on networks by an extension of the TASEP-model to networks. The network structure in the simulations is inspired by our *in vitro* microscopy experiments of crossing microtubules. Recent experiments have shown that at crossings, motors tend to switch between microtubules. We include the preferred exit direction of a motor leaving a crossing into our simulation model. The preferred exit direction results in a density redistribution through the network. As a function of global motor density on the network, various stages of homogeneous and heterogeneous density distributions are identified.

2

Experimental systems and techniques

In this thesis we use experimental and simulation techniques to investigate driven systems. Our experimental systems include sheared colloidal suspensions and molecular motors moving over microtubule networks. In both experimental systems, individual "particles" are imaged using optical fluorescence microscopy. Colloidal particles are tracked in three dimensions using confocal microscopy, while the motion of microtubule bound molecular motors is imaged with total internal reflection fluorescence (TIRF) microscopy. Consumption of ATP is driving the dynamics of molecular motors. In contrast, we apply a surface force to the colloidal suspensions by imposing an external shear rate on the system. We provide details on the systems, microscopy techniques, materials and methods used.

2.1 Colloids

Colloids are nano- to micrometer sized particles that are dispersed in a continuous phase. Colloids are ubiquitous in nature and wildly diverse in appearance. The classification "colloid" only refers to the size of the dispersed particles; the particles themselves and the continuous phase can be in all states of matter. Examples of colloidal materials include: mist and hair-sprays (liquid particles dispersed in a gas), aerogel and styrofoam (gas in solid), blood and paint (solid in liquid) and milk and mayonnaise (liquid in liquid). An illustration of the colloidal domain on a logarithmic scale bar with some materials in this range is shown in Fig. (2.1).

Due to their small size colloidal particles exhibit Brownian motion. As a result particles explore phase space and exhibit states of matter similar to conventional molecular materials.

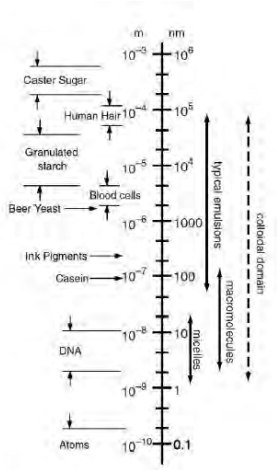

FIGURE 2.1: The colloidal domain on a scale bar. Examples of some materials that fall inside and outside the colloidal domain are shown. [13]

2.1.1 Hard-sphere colloids

The simplest system that mimics the behavior of atomic and molecular systems is probably a hard sphere system consisting of spherical non-penetrable particles

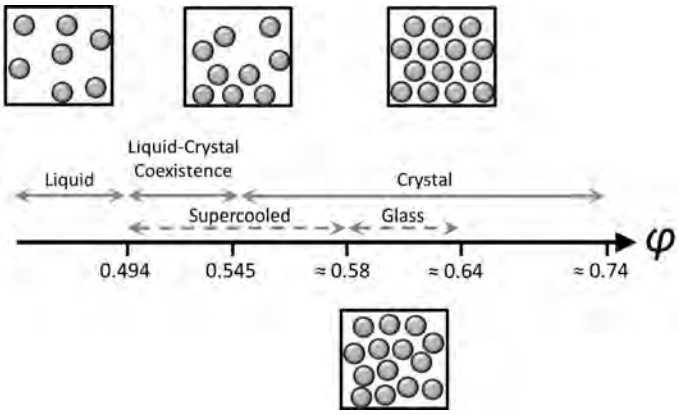

FIGURE 2.2: Phase diagram of uniformly sized hard spheres. Different phases of colloidal hard spheres are shown as a function of the volume fraction. There is a liquid phase for $\phi < 0.494$, a crystalline phase for $\phi > 0.545$, and coexistence between the two for $0.494 < \phi < 0.545$. If crystallization is avoided, for $0.545 < \phi < 0.58$, the system is a supercooled liquid, whereas for $\phi > 0.58$, the dynamics of the system becomes so slow that it is a glass. [15]

that interact only when they collide: they exhibit no interaction until they touch and the interaction is infinitely repulsive upon contact. The phase behavior of such hard sphere systems is uniquely governed by the volume fraction ϕ [14] which is defined as the ratio of the particles volume to the total volume of the system [15]. Hence, the presence of thermal fluctuations is sufficient to produce a variety of *phases* such as fluid, crystalline and glassy states of matter, analogous to the states observed in atomic and molecular physics. Yet, for colloids at much larger length scales and longer time scales, making colloids useful model systems for molecular and atomic systems, where the length- and time scales are experimentally mostly inaccessible [14].

Experimentally, the phase behavior of colloidal hard sphere systems has been studied by Pusey and van Megen using suspensions of sterically stabilized PMMA particles [14]. Fig. 2.2 shows a schematic phase diagram of mono-disperse colloidal hard spheres [14]. At low densities, there is a homogeneous fluid phase for volume fractions $\phi < 0.494$. A crystalline phase can form at high densities $\phi > 0.545$. For intermediate volume fractions $0.494 < \phi < 0.545$, the system shows coexistence between a fluid and a crystal phase. For volume fractions $\phi > 0.58$, depending on the preparation of the sample, polydispersity etc., either a crystalline phase or a colloidal glass can be found. [15]

2.1.2 Sheared colloidal glasses

The particle dynamics in a colloidal glass is constrained due to crowding. Individual particles can not move freely, but are trapped in a "cage" by the neighboring particles. As a result the relaxation time of particles increases and the glass is rigid. We probe the flow properties of colloidal glasses in chapter 6, by applying a shear to the glass and following the dynamics of individual particles by confocal microscopy.

The flow properties of a colloidal glass in the absence of shear can be characterized by the relaxation time of particles. The time required by a particle to move a distance equal to its own radius a through the solvent at temperature T with viscosity η_0 defines the Brownian timescale τ_B:

$$\tau_B = \frac{\pi \eta_0 a^3}{k_B T}\,, \tag{2.1}$$

where k_B is Boltzmann's constant. The above relation is valid for dilute systems. Interactions with other particles are not taken into account. In crowded environments like glasses, the diffusion timescale strongly increases due to interactions. One can describe the combination of solvent and particles with an effective viscosity η, which is typically much larger than η_0. By substituting η for η_0 in Eq. 2.2, the characteristic relaxation timescale of a dense colloidal system τ becomes:

$$\tau = \frac{\pi \eta a^3}{k_B T}\,. \tag{2.2}$$

The timescale associated with an applied shear rate of $\dot{\gamma}_a$ is simply $1/\dot{\gamma}_a$. If $1/\dot{\gamma}_a << \tau$ the colloidal suspension is dominated by thermal fluctuations. In the strongly driven limit $1/\dot{\gamma}_a >> \tau$ the applied shear dominates the system and will liquefy an otherwise glassy, solid colloidal suspension. We will probe the collective flow properties of a colloidal glass in chapter 6 around $1/\dot{\gamma}_a \sim \tau$.

2.2 Molecular motors moving along microtubules

We study the motion of molecular motors along microtubules, which are a basic component of the cytoskeleton of cells. The molecular motors, which move in steps with typically constant step width, allow us to study transport in a biologically relevant context: motor proteins fulfill a key role in intracellular transport. The motors carry cargo throughout the cell, for which diffusive processes are too slow.

The constant step width of motors allows for relatively easy simulations with lattice models of driven transport to study their collective behavior. We will introduce these lattice models in chapter 3. In this section, we introduce the basic properties of microtubules and the molecular motors we will study experimentally in chapter 7. Details on the experimental techniques can be found at the end of this chapter.

2.2.1 Microtubules

Microtubules are the most rigid component of the cytoskeleton giving shape to eukaryotic cells. Microtubules also play a central role in the dynamic organization and transport within cells. During cell division they bind to, and segregate, chromosomes. In this thesis we study the transport that happens *along* microtubules. Specific motor proteins bind to microtubules, exert force, bind cargo, and walk along the microtubule network as if it were a highway.

Microtubules are long hollow cylinders self-assembled from α/β-tubulin heterodimers, see Fig. 2.3. Tubilin polymerizes end-to-end with the β-subunit of one tubulin connecting to the α-subunit of another. The polymerization results in 'polarized' linear filaments of tubulin: at the plus end tubilin binds to the microtubule with the α-subunit and at the minus end tubulin binds with the β-subunit. A microtubule consists of multiple aligned filaments, all polarized in the same direction. *In vivo* a microtubule consists of 13 filaments. The outer diameter of a microtubule is 24 nm, very small compared to its linear size which can reach up to 50 μm. While microtubules elongate on both ends, the growth is

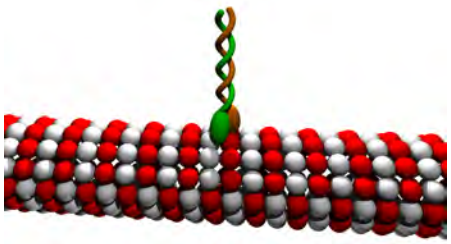

FIGURE 2.3: Schematic drawing of a kinesin motor attached to a microtubule.

much faster at the plus end. The polarization of microtubules is of vital importance for motor proteins like Kinesin-1: The polarization determines the motor's direction of motion.

2.2.2 Molecular motors

The founding member of the Kinesin superfamily, Kinesin-1, was discovered in the giant axon of squid, where it transports vesicles from the cell body to the synapses [16]. It is particularly in these long cells that diffusion does not work effectively and active transport is crucial. Diffusion is a random process, spreading a collection of molecules equally in all directions. When large distances need to be bridged in elongated cells, the directed motion of active transport is much more efficient than diffusion. Moreover, large particles experience significant drag in the viscous interior of the cell. The viscous drag slows down the diffusion process for large molecules. Molecular motors from the Kinesin families actively transport such large molecules and vesicles along microtubules with a hand-over-hand mechanism [17]. A sketch of a kinesin molecule on a microtubule segment is shown in Fig. 2.3. We study three types of Kinesin motors: conventional Kinesin-1, and from the Kinesin-2 family OSM-3 and Kinesin-II. Below we give a short description of the structure and functioning of kinesin motors, using Kinesin-1 as an example.

Kinesin-1 is a heterotetramer with two heavy and two light chains. The light chains are thought to regulate the binding to cargo. The heavy chains form the motor domain. They intertwine to form a coil, each ending with a head which binds to microtubules. The motor domain has a second binding site for ATP, the basic energy unit of cells. Upon hydrolization of ATP to ADP a motor head

unbinds and is believed to make a biased random search for re-binding to the microtubule in the direction of the plus end. Configurational changes during the stepping process inhibit the other motor head to bind ATP, preventing the dissociation of Kinesin-1 from the microtubule. Kinesin-1 makes up to 100 steps of 8 *nm* before unbinding.

A method to accurately and fast determine the dynamic properties of molecular motors from optical microscopy data is developed in chapter 7 of this thesis. With this method we study active transport by Kinesin-1, Kinesin-II and OSM3 along microtubules under crowding conditions.

2.3 Optical microscopy

Optical microscopy uses a combination of lenses to magnify small objects. Visible light emitted or reflected by a sample passes through lenses, making microscopic objects visible to the naked eye simply by magnification. Although the fundamental theory behind microscopy was only fully understood as late as the 1960s with the completion of Quantum Electrodynamics, optical microscopy has served as a crucial tool in the development of physics and biology since the 17th century.

The first optical microscope has been attributed to the Dutch spectacle maker Sacharias Jansen who lived in the early 17th century. Soon after, Antoni van Leeuwenhoek in Delft explored the unknown living world at the micro scale. With his microscopes (Fig. 2.4) Van Leeuwenhoek discovered, amongst other things, red blood cells and spermatozoa. In the 19th century the Scottish botanist Robert Brown discovered using microscopy that it is not only life that crawls at the microscopic scale; small inorganic particles also move. This "Brownian" motion was explained decades later by Albert Einstein in one of his famous 1905 papers [18]. Einstein pioneered the idea that the movement of Brownian particles is caused by random collisions with even smaller constituent particles of the solvent. This was the first convincing evidence of the molecular nature of liquids.

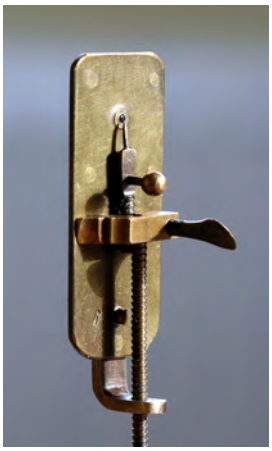

FIGURE 2.4: Microscope used by Antoni van Leeuwenhoek (replica).

2.3.1 Resolution

Today, optical microscopy still plays a major role in advancing science and microscopy techniques are continuously developed and refined. In particular, improving the resolution is of great interest, reflected by the 2014 Nobel prize in chemistry for super-resolved fluorescence microscopy [19]. The optical resolution of a microscope is the ability to distinguish particles as separate objects. High resolution means that particles can be distinguished at small spatial separation.

The image of a point-like source is a finite diffraction-limited pattern. This pattern is known as the *point spread function* (psf). The transverse cross section of the psf on the image plane is an Airy disc, see Fig. 2.5(a), whose size depends on the aperture of the objective lens as well as on the wavelength of the light source. Generally, two closely spaced luminous points in the sample plane result in overlapping discs leading to an intensity distribution with two peaks as shown in Fig. 2.5(b). A minimum separation is required between the discs to create a reasonable 'dip' in between, for the peaks to be resolved -this sets the maximum resolution of the microscope. Following the Rayleigh criterion, this separation is the full width half maximum (FWHM) of the airy disc (when the first minimum of an airy disc aligns with the central maximum of the second one) leading to a dip of about 26%, see Fig. 2.5(c). In modern optical microscopy a resolution of 250 nm can be obtained. [20]

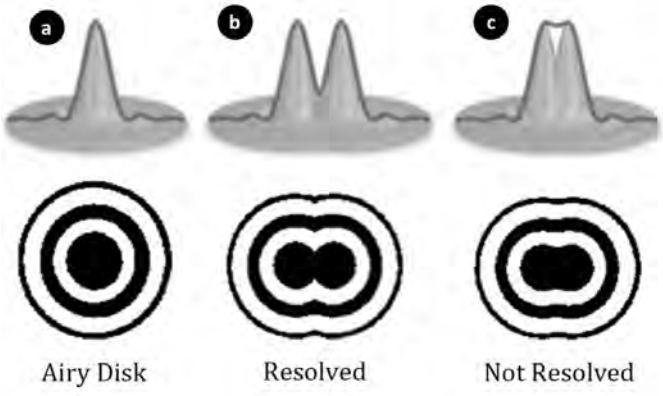

FIGURE 2.5: Resolution of microscope. (a) The airy disc of a single particle. (b) The overlapping airy discs of two closely spaced particles and (c) Rayleigh limit for identifying two particles as different objects. [20]

It is important to note that the precision of determining the position of an imaged object is different from the above discussed resolution. The position of an isolated fluorescent point-like source corresponds to the 'center of mass' of its spatially extended airy disc image. If the disc is about N pixels wide and each pixel is M micrometers across, the center of the disc can be estimated to roughly M/N accuracy, which is higher than the optical resolution. [20]

2.3.2 Fluorescence microscopy

In the quest to resolve ever smaller structures in complex environments fluorescence microscopy has been developed. Objects smaller than the wavelength of light can be observed using fluorescent labels. Fluorescence microscopy uses a light source to excite fluorophores in the sample. The fluorophores emit light upon relaxation to the ground state, typically with a longer wavelength than the illuminating light. By separating the weak fluorescence signal from the much stronger excitation light with spectral filters in the optical path, small fluorescent objects become visible with a fluorescence microscope, see Fig. 2.6. Control of the excitation light intensity over space and time in the sample makes fluorescence microscopy a powerful imaging technique.

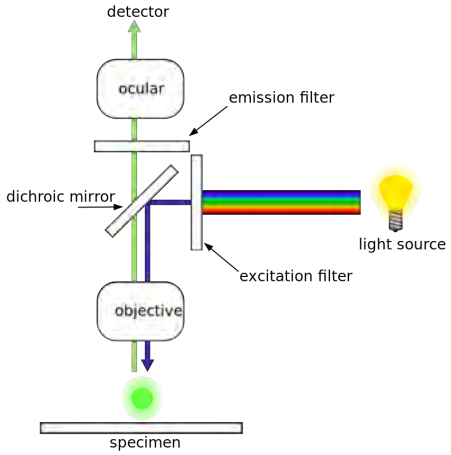

FIGURE 2.6: Sketch of the fluorescence microscopy principle.

2.4 Confocal microscopy: particle tracking in colloidal glasses

In regular, wide field microscopy the whole sample is illuminated at the same time, creating one image from the complete bulk and surface which can not be disentangled. In order to image in three dimensions, Marvin Minksky proposed a two-fold adjustment to wide field microscopy - point by point illumination of the sample as well as introduction of a pinhole aperture in the image plane eliminating all those rays emitted other than from the focal plane, Fig. 2.7(a). Light rays passing through the pinhole are measured by a detector such as a photomultiplier tube or avalanche photo-diode. Constructing the image of the whole specimen in $2D$ or $3D$ requires scanning over a regular raster in the specimen. While the first confocal microscopes used a translating stage, modern day confocal microscopes use lasers as light sources and scan it across the sample to visualize each point inside; this is called Laser Scanning Confocal Microscopy (LSCM) [21, 22]. Confocal microscopy of a transparent sample containing fluorophores allows for true 3D imaging by highlighting the specimen point-by-point and using optical filters to detect only at the fluorescent emission wavelength [20]. In the present study we use a LSCM (Carl Zeiss, LSM5, Fig. 2.7(b)) with a high speed line scanning technique to image solutions of fluorescently coated colloidal particles in the glass phase.

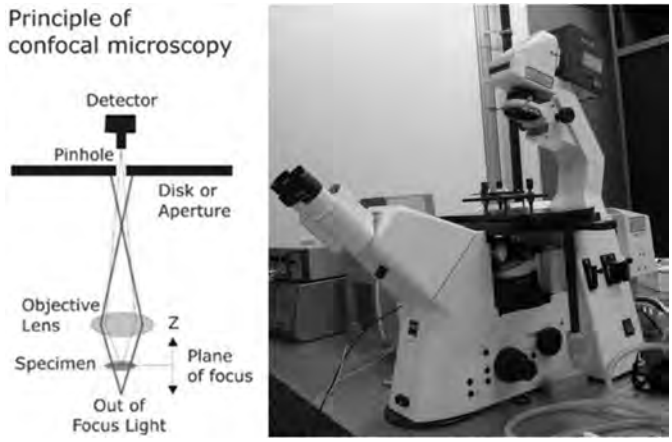

FIGURE 2.7: (a) Principal of confocal microscopy [20]. (b) The Carl Zeiss LSM5 microscope used in the colloidal experiments. [15]

2.4.1 Materials and Methods

The experiments on colloidal glasses described in this section were carried out by Vijayakumar Chikkadi during his PhD research in the group of Prof. Schall. Much of the experimental description below describes his work and can be found with more detail in [20].

Sample preparation

We prepare an amorphous suspension of PMMA particles that are 1.3 μm in diameter. They are suspended in a mixture of Cis-Decaline and Cyclo-Heptyl Bromide with a volume ratio of 1 : 3 in order to match closely the density and index of refraction of the particles with the solvent. The density matching of the particles and the solvent is needed to avoid sedimentation of the particles. The refractive index match provides a nearly transparent sample making it suitable to visualize the individual particles in the bulk of the suspension using an optical microscope. We add the organic salt TBAB (tetrabutyl ammonium bromide) to the suspension to further screen the possible residual charges. The quantity of salt added is based on the 1 mM concentration that is to be achieved. The buoyancy-matching is very sensitive to temperature changes; the thermal expansion coefficient of the solvent exceeds that of PMMA by about a factor of ten

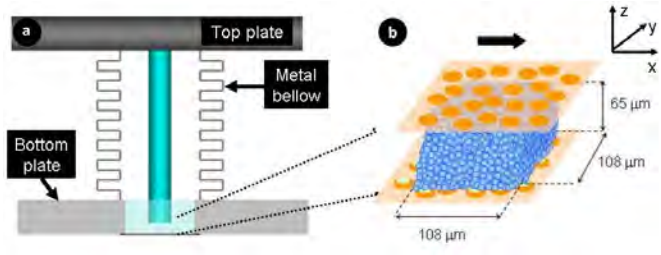

FIGURE 2.8: (a) Schematic drawing of a cross section of the shear cell. (b) 3D image of the colloids in the shear cell with the roughened glass plates that are used as boundaries. [20]

and a decalin-CHB mixture of a given composition will therefore match the particle density only in a very narrow temperature range. We exploit this fact to prepare suspensions of different volume fractions by centrifuging the suspension at a speed of $\sim 5000\ rpm$, and at a temperature $T > 35°C$, above the buoyancy matching temperature, to create a sediment that has a volume fraction close to random close packing ($\phi_{rcp} \sim 0.64$). A sample of desired volume fraction is obtained by diluting the sediment at random close packing using the density matched solvent. We typically prepare samples in the range $\phi = 0.58 - 0.60$ to study colloidal glasses. [20]

Shear cell

We probe the flow of glasses by imposing a constant shear rate, which is of the order of the inverse relaxation time of the glass. We use a home-built shear cell to apply small shear rates up to a total strain of 140 % to the colloidal glass. The shear cell is designed to be mounted directly on the confocal microscope.

The shear cell has an external frame that is assembled using a set of screws and springs; this arrangement provides a rigid frame for mounting the piezoelectric translation stage, and for securing the cell. A schematic cross section of the cell in Fig. 2.8(a) shows an arrangement of two parallel boundaries and a reservoir of colloidal sample. The cell essentially has two components - a T-shaped top plate and a bottom plate that has a hole drilled through it. The top plate of the cell is fixed to the piezoelectric translation stage and the bottom plate is fixed to the frame.

A piece of cover glass, whose surface is made rough by sintering a layer of polydisperse PMMA particles onto it, shown in Fig. 2.8(b), is glued to the top and the bottom plates. This prevents boundary induced crystallization, and ensures a no-slip condition at the boundaries. The hole in the bottom plate holds a reservoir of colloidal sample of approximately 400 μl. The top boundary, which is at the free end of the cylindrical part of the top plate, is immersed in the colloidal suspension. A metallic bellow, see Fig. 2.8(a), is used to provide a flexible coupling between the top and the bottom plates, while isolating the colloidal suspension from the environment, thereby preventing evaporation. A voltage of $0 - 150\ V$ is applied to the piezoelectric device using a digital oscilloscope, to linearly displace the top plate by $0 - 100\ \mu m$; this differential motion of the plates imposes a uniform shear rate on the colloidal sample confined between them. By adjusting the distance h between the boundaries, using the set screws, and ramping the voltage linearly from 0 V to 150 V, during a time interval t, we achieve a shear rate of $\dot{\gamma} \sim 100/(ht)$. The coordinate axes of the system are defined with respect to the direction of shear, as shown in Fig. 2.8(b); the x-axis aligns with the direction of displacement of the top boundary, the y-axis aligns with axis of shear, and the z-axis aligns with the shear gradient direction. [20]

Data acquisition

We image the colloidal particles using an objective that has a magnification of 63x and a numerical aperture of 1.4. The Zeiss LSM 5 microscope uses a line scanner to illuminate a section of the sample line by line, at a maximum of 120 frames per second (fps). The depth of the focal plane, Z, is controlled by a piezo−element mounted on the objective of the microscope [20]. For 3D imaging, $z-$stacks of 2D images are acquired by rapidly varying the height of the objective using the piezo and simultaneously taking 2D images at each z. We typically image a $106 \times 106 \times 70 \mu m^3$ volume by taking 350 images at a spacing of $0.20 \mu m$ in the z direction. At a scan speed of 8 fps, it takes $\sim 45 sec$ to acquire a $z-$stack. We typically acquire $1 - 2$ stacks every minute to follow the individual particle dynamics. [20]

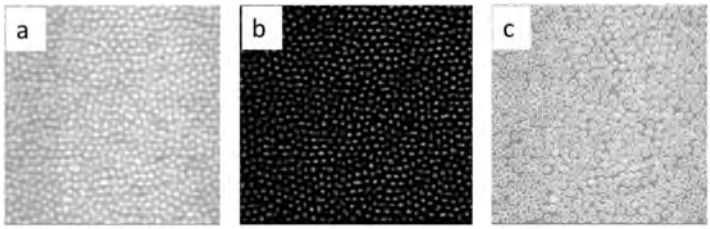

FIGURE 2.9: Image processing of confocal images. (a) Raw confocal image (b) Filtered image (c) Tracked image. [25]

2.4.2 Data processing

Image processing

To follow the particle dynamics under applied shear, we use particle tracking software [23]. The first step in the particle tracking algorithm is the identification of particles and their position. We determine the particle positions in each frame by using the most widely used algorithm in the colloidal community, developed by Crocker and Grier [23], with relevant software in the public domain [24]. The algorithm identifies the particles based on the assumptions that they appear as bright spherical spots against a dark background, and the intensity maxima of the spots correspond to the center of the particle. Since we have used PMMA particles that are labeled with fluorescent dye, they appear as bright spots in the raw images (Fig. 2.9(a)) [20, 25]. The undesired noise in the images is eliminated using a spatial band pass filter, which removes long wavelength contrast gradients and also short wavelength pixel-to-pixel noise (Fig. 2.9(b)). The particles are initially identified by locating the local intensity maxima in the filtered images. The particle coordinates are then refined to get the positions of the particle centers with sub−pixel resolution down to less than 1/10 of the pixel size (Fig. 2.9(c)). [20]

Particle positions

From the obtained particle positions we can construct the pair correlation function $g(r)$, that describes how the local density varies as a function of the distance r from a reference particle, Fig. 2.10. The pair correlation function provides information on the structure of a material. The structure measured with the

microscope, however, might be distorted by calibration or misalignment errors. To correct for distortion errors we find a coordinate transformation by studying a quiescent colloidal glass, which is known to be isotropic and homogeneous. Hence, we use the fact that the average distance between particles in an isotropic and homogeneous material should be independent of direction and angle.

We measure the displacement vector r_{ij} for each particle i with all its nearest neighbors j directly from the particle positions obtained with microscopy. Nearest neighbors of reference particle i are all particles within a distance $\|r_{ij}\| < r_{\text{cuttof}}$. We take the cuttof distance to be $r_{\text{cuttof}} = 2.1\mu m$, corresponding to the minimum after the first peak in the pair correlation function.

We use the tensor product of all particle distances to correct for possible alignment errors. Taking the tensor product of r_{ij} with itself and averaging over all nearest neighbors in the sample results in the following tensor:

$$G = \langle r_{ij} \otimes r_{ij} \rangle_{ij} \quad \text{with} \quad \|r_{ij}\| < r_{\text{cutoff}} \,. \tag{2.3}$$

For an isotropic material all off−diagonal elements of this matrix should be zero and all diagonal elements should be equal. We find that in our experimental case small deviations from this ideal behavior occur, indicating image distortions. To correct for these distortions, reflected in the G tensor, we find a matrix S to transform the coordinates into the ideal configuration where all off-diagonal components vanish and all diagonal components are identical:

$$SGS^{-1} = \lambda I \,, \tag{2.4}$$

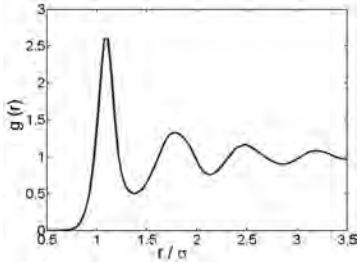

FIGURE 2.10: Pair correlation function for a colloidal glass. [15]

where the scalar λ is determined implicitly by

$$\|Sw\| = \|w\| \quad \text{with} \quad w = \begin{pmatrix} 1/\sqrt{(3)} \\ 1/\sqrt{(3)} \\ 1/\sqrt{(3)} \end{pmatrix}, \tag{2.5}$$

to preserve the absolute distance between particles under the coordinate transformation. Rescaling all particle coordinates with the matrix S, $r'_{ij} = Sr_{ij}$, then results in an isotropic set of coordinates. We apply the transformation matrix S to the particle positions obtained from shear experiments to correct for measurement related anisotropy.

Particle tracking

The hence corrected positions of the particles can now be linked to construct trajectories that describe the particle motion. We use the algorithm devised by Crocker and Grier [23] for linking the particle positions. The algorithm is based on the minimization of the sum of the squared displacements of particles in two successive frames. Repeating the minimization algorithm for successive frames to link the particle positions constructs the particle trajectories.

At low shear rates, $\gamma \sim 10^{-5}s^{-1}$, we typically acquire a z− stack every minute for a total time duration of 25 minutes. At higher shear rates, we reduce the time between subsequent z−stacks to 30 seconds. Above a certain shear rate, acquiring 3D data is no longer feasible because the particles move over a distance larger than their radius between successive stacks. This imposes a limit on the maximum shear rate to acquire 3D images. [20]

2.5 TIRF microscopy: motion of molecular motors on microtubules

Totally Internal Reflection Fluorescence (TIRF) microscopy is a technique to observe fluorescent particles at the surface of a sample. The exciting laser is totally internally reflected in the glass at the glass−sample(water) interface. No light penetrates the sample, only evanescent waves of light can excite fluorophores

immediately adjacent to the surface. The noise on the surface signal is low, because there are no excited fluorophores in the bulk of the sample. This makes TIRF microscopy a powerful tool for high−quality 2D imaging. We use a Nikon Eclipse TI microscope, equipped with custom TIRF optics, to observe the motion of molecular motors along the microtubule network.

2.5.1 Materials and Methods

In this section we describe the *in vitro* stepping assay experiments of molecular motors moving along microtubules. In a stepping assay, the microtubules are attached to a glass plate and the motors move along the microtubules. The microtubules are dynamically stabalized to stop their growing and shrinking. First, the microtubules are flown into a microfluidic channel and attach to the glass slide after sedimenting. After the microtubules have sedimented, a motility solution containing the molecular motors is flown into the microfluidic channel. The motors attach to the microtubules and start to move by consuming the ATP in the solution.

The experiments described in this section were all performed by Vandana Kushwaha and Seyda Acar in the group of Prof. Peterman at the VU University in Amsterdam. I acknowledge them for providing the detailed description of the experimental procedures below.

If not specially mentioned otherwise, all chemicals were purchased from Sigma. All concentrations given are final concentrations.

Microtubules Preparation

Tubulin was purified from bovine brain tubulin similar to as described previously [26]. Microtubules were polymerized from 5 μm of bovine brain tubulin seeds (5 mg/ml) in PEM80 [80mM PIPES pH 6.9, 1 mM EGTA, 2mM MgCl2 (Fluka analytical 63072)] buffer supplemented with 4 mM MgCl2, 1 mM GMPCPP (non hydrolysable GTP analogue, Jena Bioscience NU405S,) and 5

Motor proteins

The three motor proteins used in the experiments were *Drosophila melanogaster* Kinesin-1 (conventional kinesin) and *C. elegans* homodimeric OSM-3 and *C. elegans* heterodimeric Kinesin-II. These motors are processive motors and walk towards the plus-end of MTs.

Cloning, Purification and Preparation of Proteins
Kinesin-1 – The DNA sequence coding for the first 432 amino acids of conventional kinesin-1 from Drosophila melanogaster was amplified with the primers by polymerase chain reaction and cloned into pETDuet-1 vector (Addgene) generating pETDuet1-MCS1-Kin432. As fluorescent tag, the gene of monomeric super folded (sfGFP) and as purification tag, the Strep- tagII sequence was ligated to the C-terminal end of the kinesin sequence, resulting in the pETDuet1-MCS1-Kin432-sfGFP-StreptagII plasmid. This plasmid was transformed into Rosetta-gami^{TM} 2(DE3) pLysS competent cells (Novagen®). Protein expression was induced by addition of 0.4 mM IPTG to a 1.6L culture in the Erlenmeyer flasks. Expression was allowed to proceed for 6 hours at 22 $°C$, 250 rpm in a floor incubator. Expressed proteins were purified from the lysate using the Strep-tag® - Strep-Tactin® purification system (protocol adapted from QIAGEN website)

OSM-3 – Similarly, The DNA sequence coding for the first 444 amino acids of C. elegans OSM-3 was amplified with the primers by polymerase chain reaction and cloned into pETDuet-1 vector (Addgene) generating pETDuet1-MCS1-Osm-3. This construct also contained the sequence coding for a C-terminal sfGFP tag (pETDuet1-MCS1- Osm-3444-sfGFP) or mCherry tag (pETDuet1-MCS1- Osm-3444-mCherry). For purification, the Strep tagII sequence was ligated to the C-terminal end of the sfGFP, generating pETDuet1-MCS1- Osm-3444-sfGFP-StreptagII. Both construct were expressed and purified using the Strep-tag®-Strep-Tactin®purification system (protocol adapted from QIAGEN website) in our lab. Purified motor protein solution in buffer containing 20 % (V/V) glycerol was aliquoted and 10 μl aliquots were stored at -80 $°C$, after flash freezing in liquid nitrogen. The kinesin concentration was 2.2 mg/ml, the sfGFP-OSM-3 concentration was 1.3 mg/ml and the mCherry-OSM-3 concentration was 1.2 mg/ml, as measured using Bradford assays with bovine serum albumin as standard. [26, 27]

Kinesin-II – Kinesin-II construct has two different motor proteins, thus for this protein we cloned KLP-11 (357aa) and KLP-20 (345aa) constructs either with sfGFP (for fluorescently labeled) or with Snap tag (for unlabeled) and followed exactly the same procedure for OSM-3. These constructs also contained Kinesin-1 minimum part of stalk for dimerization. KLP-11 and KLP-20 constructs were cloned into multiple cloning site-1 (MCS-1) and multiple cloning site-2 (MCS-2) of the pETDuet-1 vector. For purification of the heterodimers we used two different affinity purification tags, 6xHis tag and Strep tag, on KLP-11 and KLP-20. The plasmids containing these double inserts were transformed, expressed and purified as stated for the Kinesin-1 construct. The concentration of unlabeled Kinesin-II and sfGFP-Kinesin-II were measured as 1 mg/ml and 0.29 mg/ml respectively using Bradford assays with bovine serum albumin as standard. [26, 27]

In Vitro Motility Assays

Glass surface preparation Hydrophobic surfaces were used for single-molecule motility assays in order to strongly adsorb antibodies against tubulin to the glass surface and to allow efficient surface blocking using amphiphilic Pluronic F127. Pluronic F127 is a polymer with a hydrophobic middle segment that that sticks to the hydrophobic glass, and two hydrophilic tails that was form a 'polymer brush', preventing unwanted protein (i.e. kinesin) adsorption to the surface.

Glass Cleaning Glass coverslips were loaded into teflon racks and microscope slides were loaded into multiple glass slide racks and then, the racks were placed in the plasma cleaner for 20 minutes. Afterwards, the holders with the coverslips and glass slide racks with microscope slides were incubated for 15 min in 0.1 M KOH. After another 1 min and 2 min wash sequence with nanopure water, the coverslips were blown dry with Argon gas.

Silanization 100 μl DDS (diphenyldimethoxysilane) was carefully dissolved in 250 ml TCE (trichloroethylene) in a glass beaker. The Teflon holder with the cleaned coverslips was incubated in this solution for 60 min at room temperature, followed by two steps of sonication for 5 min and for 15 min, both in methanol at room temperature. Finally, cleaned and hydrophobic slides and coverslips were blown dry using Argon gas and transferred into clean holders and stored in a closed glass box, sealed with parafilm.

Flow cells preparation Assays were performed in hydrophobic flow cells made of microscope slide (Menzel-Gläser, 76x26 mm, cut edges) attached to a coverslip (High Precision, Deckgläser, 22x22 mm, thickness 170±5 μm) with double-sided Scotch tape (70 μm inner height), resulting in flow channels with a volume of 5-8 μl.

Instrumentation Assays were performed at 21 $°C$ using Total Internal Reflection Fluorescence (TIRF) microscopy. Microscope images were acquired using a custom-built TIRF microscope operated by the Micro-Manager software interface (μManager, Micro-Manager1.4, https://www.micro-manager.org/), built around an inverted microscope body (Nikon, Eclipse Ti) fitted with a 100x oil-immersion objective (Nikon, CFI Apo TIRF 100X, N.A.: 1.49). Excitation light, provided by two diode-pumped solid-state lasers (Cobolt Calypso 50TM 491 nm DPSS; and Cobolt Jive 50TM 561 nm DPSS), was first passed through an AOTF (AA Opto-Electronics, AOTFnC-400.650-TN) for wavelength selection, next through a quarter wave-plate (Thorlabs, mounted achromatic quarter-wave plate, 400 – 800 nm, AQWP05M-600) to obtain circularly polarized light, and a dichroic mirror (Semrock, 405/488/561/635 nm lasers Brightline® quad-edge laser-flat, Di01-R405/488/561/635-25x36) was used. Power of 491 nm Cyan laser were estimated to be ∼1.3 mW in the image plane. Emission light was separated inside the Optosplit III using a dichroic long pass filter. The pixel size was 80 nm. Images were acquired continuously with 7 frames/sec, without delay in between and saved as 16-bit tiff files.

Kinesin-1–MT crowding assays:
To immobilize microtubules, the sample chambers were first incubated with 2 $\mu g/ml$ monoclonal anti-β-tubulin antibody in PEM 80 with 10 μM taxol. After 5-min incubation, excess antibodies were flushed out with PEM 80 with 10 μM taxol, followed by 15 min incubation with 1 % (wt/vol) Pluronic F-127 in PEM 80 with 10 μM taxol. To flush out excess Pluronic F127, the chambers were rinsed with PEM 80 with 10 μM taxol after 15 min incubation. Finally, sample chambers were incubated with 0.1 mg/ml microtubules in PEM 80 with 10 μM taxol and allowed them to attach to the surface via the antibodies for 10 min. After attaching the microtubules, the sample chambers were flushed with PEM12 buffer (12 mM PIPES pH 6.9, 1 mM EGTA, 2 mM MgCl2). PEM12, a low-salt buffer, was used for the experiments because in this buffer a 10 times lower kinesin-1 concentration was sufficient to generate the same number of events as

in PEM80. This significantly reduced the background caused by non-specific binding of kinesin-1 to the surface. In the final step, the sample chambers were flushed with motility solution supplemented with 10 μM Taxol, 2 mM additional MgCl2, 2 mM ATP (adenosine 5' triphosphate), 0.2 mg/ml casein in PEM12, an oxygen scavenging cocktail containing 200 $\mu g/ml$ glucose oxidase, 72 $\mu g/ml$ catalase, 22.5 mM glucose, and 10 mM of DTT (dithiothreitol) and an estimated final concentration of kinesin-1 were varied from 0.175 nM to 3 nM. Finally, the sample chambers were sealed with VALAP (1:1:1 vaseline, lanoline, paraffin) and moving motors can be observed under the TIRF microscope setup. Another set of crowding experiment was performed in higher ionic concentration, PEM 80, where sfGFP labeled to unlabeled Kinesin-1 motor proteins were kept 0.2:0, 1:0, 1:5, 1:10, 1:20, 1:40, 1:100 and 1:200 respectively where 1 was kept at 40 nM. The sfGFP-Kinesin-1 motors were illuminated by the 491 nm laser. Images were acquired continuously using an exposure time of 100 ms without delay.

OSM-3–MT crowding assays - Two-color motility assays:
In these assays, subsequent to all the steps until the microtubule immobilization, motility mix was added that contained a final concentration of 8 nM to 4040 nM OSM-3, 10 μM Taxol, 2 mM MgCl2, 2 mM ATP (adenosine 5' triphosphate), 0.2 mg/ml casein in PEM12, ATP regeneration system (Phosphocreatine 10 mM, Creatine phosphokinase 0.05 mg/ml), an oxygen scavenging cocktail containing 200 mug/ml glucose oxidase, 40 $\mu g/ml$ catalase, 22.5 mM glucose, and 10 mM of DTT (dithiothreitol)). OSM-3 motor protein motility was observed using TIRF microscopy. The mCherry-OSM-3 motors were illuminated with a 561 nm laser. Images were acquired continuously using an exposure time of 70 ms and 50 ms without delay in between and saved as 16-bit tiff files. Another set of crowding experiment was performed in lower ionic concentration, PEM 12, where the ratio of sfGFP labeled to unlabeled OSM-3 was kept 0.2:0, 1:0, 1:10, 1:20, 1:40 and 1:100 respectively where 1 was kept at 40 nM. The sfGFP-OSM-3 motors were excited with the 491 nm laser. Images were acquired continuously using an exposure time of 70 ms and 50 ms without delay in between.

Kinesin-II–MT crowding assays
In these crowding experiments, the ratio of sfGFP-Kinesin-II to unlabeled Kinesin-II was kept 0.2:0, 1:0, 1:10, 1:20, 1:40 and 1:100 respectively where 1 was kept at 40 nM. Experiments were performed in both PEM12 and PEM 80 buffers. The

sfGFP-Kinesin-II motors were illuminated with the 491 nm laser. Images were acquired continuously using an exposure time of 150 ms without delay.

2.5.2 Data processing

We develop an advanced analysis technique to extract quantitative motility parameters from the image sequences in an automated way. Correlation of the fluorescence intensities allows efficient determination of parameters such as motor velocity, randomness and average run length. This new technique allows a quicker analysis and requires less data than the commonly used single-particle tracking approach. Moreover, correlating intensities allows analysis of data obtained under conditions inaccessible for single-particle tracking, including those performed at high motor densities, which provides insight into traffic-jam-like interactions between motors. The correlation technique and its application to motors in crowded environments is discussed in detail in chapter 7 of this thesis.

3

Transport models

In this chapter we introduce the models we use later in this thesis to study traffic on highways and collective motion of molecular motors in biological cells. The totally asymmetric simple exclusion process (TASEP) model is a paradigmatic model in far from equilibrium physics, used to study transport in one-dimensional systems. We review the main results of TASEP along a one-dimensional chain for open and closed boundary conditions. The one-dimensional TASEP-model can be extended to networks to study transport in higher dimensional systems. We use this extension to model transport of molecular motors along the cytoskeleton. Further, we introduce the Nagel-Schreckenberg (NS) model for traffic flow. The NS-model can be thought of as an extension to TASEP which allows cars to have various velocities. We review the basic properties of the NS-model and discuss how it relates to the TASEP-model.

3.1 Introduction

Microscopic models of transport are typically build from a set of dynamical rules defining motion at the particle scale. The increase of computational power over recent years has allowed for an extensive study of these models, when analytic solutions are not available. These microscopic models of far from equilibrium systems have a fundamentally different approach than their equilibrium counterparts. In models of equilibrium physics interaction energies between particles are specified to form a Hamiltonian. The Hamiltonian can be used to derive the particle dynamics. Interaction energies and the Hamiltonian are often unknown in far from equilibrium transport. And instead, a set of dynamical rules at the particle scale take their place in microscopic models of driven transport.

The totally asymmetric simple exclusion process (TASEP) model is a simple stochastic microscopic model for driven systems in one dimension with hard-core particle interactions [7]. Particles progress uni-directionally with steps of size one along a segment of length L if the target site is empty and do not move otherwise. Particles are updated according to the above rule in random sequential order: each time step, a random particle is chosen and updated. The TASEP dynamics is illustrated in Fig. 3.1, where α and β represent the inflow and outflow rate, respectively, for a system with open boundaries.

Due to its simplicity and effectiveness, TASEP has become a paradigmatic model in far from equilibrium transport, much like the Ising model in equilibrium physics. TASEP was introduced to model the dynamics of RNA polymerization by ribosomes [7, 28]. Soon after it received wide interest from a fundamental point of view in statistical physics [29] and mathematics [30]. This resulted in a

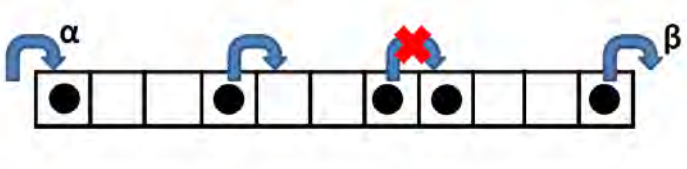

FIGURE 3.1: Schematic description of particle motion along a one-dimensional chain in the TASEP model.

detailed understanding of the model and analytical solutions for both open [31] and closed boundary conditions.

Applications of TASEP can be found in a wide range of physical and non-physical systems. In cell biology, TASEP turned out to be extraordinarily useful [11, 32]. Besides the initial application to RNA polymerization, the model has been used to describe the collective motion of molecular motors along the cytoskeleton [33, 34] and transport of macromolecules through membrane channels [35].

Vehicular transport is perhaps the most well-known application of TASEP outside physics. Because of its inherent exclusion rule, it captures the basic ingredient of vehicles avoiding collision. As a result, TASEP and many of its related models [6, 36] show jamming phenomena when the density of particles becomes high so that they interact significantly.

Other applications of exclusion processes include the movement of pedestrians [37], in particular useful for designing evacuation schemes. In condensed matter physics, TASEP models have been used to describe electron transport through a chain of quantum dots [38]. Recently the relevance of TASEP for describing transport of colloidal particles through microfluidic networks has been proposed [39].

In the next section we describe the Nagel-Schreckenberg model, an extension of TASEP to describe traffic flow we use in chapter 4 and 5 of this thesis. The main results of TASEP on a single segment are discussed in section 3.3. We describe how TASEP is generalized from a single segment to a network in section 3.4. We use TASEP on a network in chapter 8 to describe transport of molecular motors along the cytoskeleton.

3.2 Nagel-Schreckenberg model

The Nagel-Schreckenberg (NS) model was introduced in the early nineties to describe traffic as observed on a freeway [6]. In the NS-model, vehicles tend to accelerate to a maximum velocity v_{max}, under the condition that they have enough free space. They become constrained when the distance to the next car d_i is smaller than their velocity v_i: $d_i < v_i$. The constraint forces the cars to lower their velocity such that a collision is avoided. Note that we can compare velocity

and distance directly because time is measured in units of 1. The complete update scheme of the NS-model consists of the following rules, applied in parallel to all N cars:

1 *Acceleration*: $v_i \to \min(v_i + 1, v_{max})$.

2 *Avoiding collisions*: If $d_i < v_i$ then $v_i = d_i$.

3 *Randomization*: Decrease v_i obtained in the previous steps by 1, to a minimum of 0, with probability p.

4 *Position update*: $x_i \to x_i + v_i$, $d_i \to d_i - v_i + v_{i+1}$.

The stochasticity parameter p reflects the drivers' freedom to decelerate to a velocity below v_{max}. Cars all move during each time interval, i.e. the algorithmic update of vehicles occurs sequentially (in parallel).

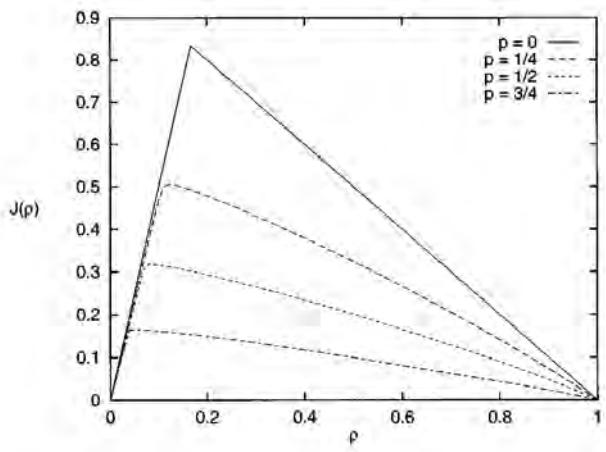

FIGURE 3.2: NS-model with $v_{max} = 5$ several values of p. [40]

The NS-model can be solved analytically for $v_{max} = 1$. Higher values of v_{max}, however, allow for a more realistic comparison with real traffic. As an example, the NS-model has been studied with $v_{max} = 5$ for several values of p. The resulting relation between current J and density ρ is shown in Fig. 3.2. The choice of $v_{max} = 5$ can be understood from a rough estimate of length and time scales: with a maximum velocity of 120 km/h on highways and a minimum distance between cars of 7.5 meters (the size of a lattice site), the update step corresponds to approximately 1 second [41], which is indeed the typical reaction

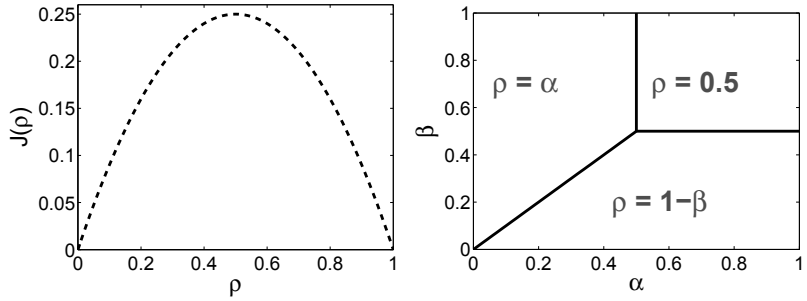

(a) (b)

FIGURE 3.3: (a) Diagram relating current and density for TASEP with periodic boundary conditions. (b) Phase diagram for TASEP with open boundaries.

time of a driver, and is thus the smallest relevant timescale. Nevertheless, it is commonly believed that all $v_{max} > 1$ are qualitatively similar [42, 43] and often $v_{max} = 2$ is taken in simulations for simplicity.

3.3 Results for TASEP in one dimension

In this section we briefly review the main results of TASEP on a single segment. Both for open and closed boundaries the model has been studied extensively. The results are useful when we study TASEP on a network in the next section and in chapter 8.

3.3.1 Periodic boundaries

For a closed system with periodic boundary conditions the relation between current and density can be derived with mean field theory. The current is given by:

$$J = \rho < v >, \tag{3.1}$$

where $< v >$ is the average particle velocity. Particles move with $v = 1$ if they are not constraint by the occupation of the downstream lattice-site. At very low densities the probability of a particle being constrained is approximately zero. With increasing density, the number of constraint particles increases and $< v >$ decreases. In mean-field, the probability that a particle is constrained, i.e. the

downstream lattice site is occupied, is simply ρ. Therefore, the probability that a particle can move is $1-\rho$, so $< v >= 1-\rho$ and:

$$J = \rho(1-\rho)\,. \tag{3.2}$$

The expression in Eq. (3.2) is exact for infinitely long segments. The corresponding fundamental diagram is plotted in Fig. 3.3(a). The mean-field approach resulting in Eq. (3.2) is valid for all homogeneous segments.

3.3.2 Open boundaries

For open systems, the results of TASEP are sensitive to the conditions at its boundaries. The entry rate α and exit rate β control the state of the system.

The entry rate α defines the probability that a new particle enters the system at the most upstream lattice site *if this lattice site is unoccupied.* The exit rate β defines the probability that a particle leaves the system from the most downstream lattice site *if this lattice site is occupied.* It should be noted that α and β are not flow rates through the boundaries. Rather, one can think of the lattice as being connected to two reservoirs: a reservoir with effective particle density α at the upstream boundary and a reservoir with effective particle density $1-\beta$ at the downstream boundary. Thinking of α and β in terms of reservoir densities on the boundaries of a segment is useful when we describe TASEP on networks as a collection of crossings and segments. In that case, the reservoir densities correspond to the densities at the segment crossings at the beginning and end of each segment.

For large segments the particle density for TASEP with open boundary conditions is given by [31]:

$$\rho(\alpha,\beta) = \begin{cases} \alpha & \alpha \leq \beta < 1/2 \quad \text{low-density} \\ 1-\beta & \beta \leq \alpha < 1/2 \quad \text{high-density} \\ 1/2 & \alpha,\beta \geq 1/2 \quad \text{maximum-current} \end{cases} \tag{3.3}$$

One can see from Eq. (3.3) that the open boundaries result in three homogeneous phases, see Fig. 3.3(b). A low-density phase if the entry rate is smaller than the exit rate. If the exit rate is smaller than the entry rate, the limited outflow

forces the density into a high-density phase. The third phase is known as the maximum current phase. In contrast to the low- and high-density phases the density in the maximum current phase is insensitive to changes in α and β. The density $\rho = 1/2$ in the maximum current phase corresponds to the maximum of the current for homogeneous segments, see Fig. 3.3(a). In all three phases the density distribution in a segment is homogeneous. Therefore, Eq. 3.2 can be applied to calculate the current through a segment within each phase. Only at the phase boundaries the density distributions might not be homogeneous and Eq. 3.2 cannot be directly applied.

The maximum-current phase is connected to the low-density and the high-density phase, see Fig. 3.3(b). The density on both boundaries of the maximum-current phase is $\rho = 1/2$ and changes continuously while crossing over into the low-density or high-density phase. It follows from Eq. 3.3 that: the maximum density $\rho = 1/2$ of the low-density phase is reached on the boundary with the maximum-current phase, similarly the minimum density $\rho = 1/2$ of the high-density phase is on the boundary between the high-density and the maximum current phase. As the density in the maximum-current phase is also 1/2, we conclude that the density changes continuously on the boundaries of the maximum-current phase. The transition between the low-density and high-density phase, however, is discontinuous. This transition is positioned at $\alpha = \beta$, see Fig. 3.3, with $\rho = \alpha$ in the low-density phase, and $\rho = 1 - \beta$ in the high-density phase. The density changes discontinuously from $\rho = \alpha$ to $\rho = 1 - \beta = 1 - \alpha$ at the transition.

3.3.3 Relation to NS-model

The NS-model can be thought of as an extension to TASEP. The models share the key ingredients: uni-directional motion and an exclusion principle to avoid collisions. In the NS-model, however, cars can have several velocities, not only 1 or 0. Moreover, cars on a road all move in parallel, so a parallel update scheme is more appropriate for traffic modeling than the random-sequential update scheme of TASEP.

With maximum velocity $v_{max} = 1$, the only difference between NS and TASEP thus arises from the update order, which is parallel in the NS-model and random-sequential for TASEP. The parallel update scheme of the NS-model, together

with the kinetic constraint, creates order. Cars move simultaneously and cannot occupy the same region of space during an update cycle. Therefore, the lattice site a moving car is departing will be unoccupied at the end of a time step under NS dynamics. In contrast, random-sequential update does not put restrictions on the possible configurations and can be analyzed with a pure mean-field approach [41].

3.4 TASEP on networks

We apply TASEP to study the transport of molecular motors along the cytoskeleton. Originally formulated for one-dimensional systems, TASEP has recently been extended to networks [11]. For example, Neri *et. al.* used TASEP on highly connected networks to model transport along cytoskeleton assemblies [12].

We model cytoskeleton assemblies with a two-dimensional network of intersecting segments. The two-dimensional network topology allows for comparison with *in vitro* experiments, where the cytoskeleton is typically grown by sedimenting segments on a glass plate (Fig. 3.4(a)). A similar network topology in our simulations is created by projecting lines with random positions and directions on a square, see Fig. 3.4(b). We create periodic boundary conditions by connecting the beginning and end of every line at the boundaries of the square, thus creating a closed network. The resulting network is characterized by the number of vertices N_v, number of segments $N_s = 2N_v$ and total number of sites $M_s = (2L-1)N_v$, where L is the segment length. The network is subsequently populated with motors at a global density ρ, defined as the ratio between the total number of motors and the total number of sites M_s.

The dynamics of the motors is specified by TASEP. A crossing in the network is simply a single site shared between two filaments. When a motor arrives at a crossing, it continues along one segment with probability γ, and along the other outgoing direction with probability $1-\gamma$ (Fig. 3.4(c)). In chapter 8 we investigate the density distribution and current through such a network as a function of probability γ and particle density. We examine the case when the choice of the outgoing segment does not depend on the incoming segment and the probabilities γ are defined for every crossing upon network creation.

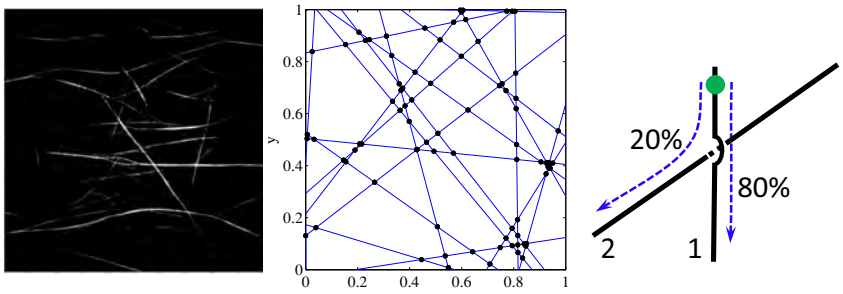

FIGURE 3.4: (a) Experimentally obtained microtubule network. (b) Simulated network. (c) Sketch of crossing with probabilities for particle paths corresponding to $\gamma = 0.8$.

On the closed networks we consider, the total number of particles is conserved. The number of particles on each segment, however, is not conserved and changes at the boundaries. Therefore, a description of the network using results from TASEP with open boundaries for each segment of the network, with the vertices working as the particle reservoirs controlling the inflow and outflow of the segments is useful.

4

Far from equilibrium: an analogy between glasses and traffic

Dynamic arrest is a general phenomenon across a wide range of driven systems including traffic flow and dynamics in cells, but the universality of dynamic arrest phenomena remains unclear. We explore similarities in dynamic arrest far from equilibrium by comparing traffic to glass forming liquids. The glass transition, i.e. the sharp increase of viscosity in glass forming liquids, is a widely studied example of dynamic arrest. Glasses are far from equilibrium systems with complex structures and dynamics. In this chapter we connect the emergence of traffic jams in a simple traffic flow model directly to the dynamic slow-down in kinetically constrained models for glasses, to highlight the universal aspect of dynamic arrest far from equilibrium. In kinetically constrained models, the formation of glass becomes a (sharp) transition in the limit $T \to 0$. Similarly, using the Nagel-Schreckenberg model to simulate traffic flow, we show that the emergence of jammed traffic acquires the signature of a sharp transition in the deterministic limit $p \to 1$, corresponding to overcautious driving.

4.1 Introduction

Dynamic arrest, the slow-down of driven systems with increasing density or interaction potential, is a central phenomenon in complex driven systems across biology, geology, material science, transport and traffic. The dynamic arrest is important for material stability and memory, but it is rather detrimental in traffic or transport, where congestion freezes motion. The underlying principle of dynamic arrest in condensed materials and traffic, however, might be of similar origin.

In this chapter, we start to explore the universality of dynamic arrest in far from equilibrium systems by comparing traffic and the much studied glass transition - the sharp increase of the viscosity of glass forming liquids. Important insight into dynamic arrest of glasses comes from kinetically constrained models (KCMs), a class of discrete models with stochastic dynamics that are used to describe the glassy behavior and increasing relaxation time scales in supercooled liquids [44]. As the defining ingredient, KCMs have a kinetic constraint that allows local activity only if a local condition is met.

A constraint that is directly analogous to those in KCMs exists in traffic flow: cars can accelerate only if the distance to the car in front is sufficiently large. A well-studied model that incorporates a number of basic dynamical properties of real traffic is the Nagel-Schreckenberg (NS) model [6], a lattice-gas-like model with discrete position, time, and velocity. The NS-model describes the formation of traffic jams, and there has been much discussion about the physical nature of the arrest phenomenon and the size of traffic jams [45–47]. There are a number of other models that describe traffic flow more realistically, including some that are extensions of the NS-model [48, 49]. Here, however, we focus on the most basic version of the NS-model to draw a direct connection to the dynamics of glasses.

The key in the correspondence between these far from equilibrium systems is the kinetic constraint, both present in KCM's of glasses and in all models of traffic in which collisions are avoided. We use tools from glasses to study dynamic heterogeneity in the traffic model, to explore possible divergences of traffic jams; by doing so we establish an analogy between glasses and traffic.

4.2 NS-model

As explained in chapter 3, the NS-model simulates traffic flow in discrete space and time. Cars accelerate towards, and maintain, a maximum velocity v_{max}, if they are not constrained by another car. Furthermore, cars spontaneously reduce their velocity by 1 with probability p. This probability is the central fluctuation parameter of the model. Jams start to emerge when the car density ρ increases and car interactions become dominant. In the simulations described in this chapter, we have propagated $2^{14} = 16384$ cars under periodic boundary conditions. A steady-state was produced by propagating the system for 5×10^7 time steps. Averages were calculated over a further 5×10^8 time steps.

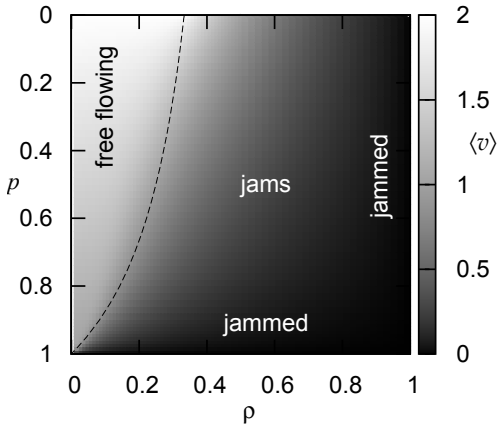

FIGURE 4.1: Phase diagram of the Nagel-Schreckenberg model showing $\langle v \rangle$ for the case of $v_{\max} = 2$ (see gray scale on the right). The dashed line marks the transition between freely flowing traffic and traffic with jams shown in Eq. 4.1.

We explore the dynamic arrest in the NS-model in Fig. 4.1, where we show the average velocity $\langle v \rangle$ as a function of ρ and p for $v_{\max} = 2$. Traffic exhibits free flow at low density. Here, the average velocity is the velocity of free flow. With increasing density, cars interact and decelerate according to the kinetic constraint, leading to the formation of jams that coexist with free flow, and a concomitant decrease of $\langle v \rangle$.

The transition density ρ_{tra} between free flow and traffic with jams can be estimated from the balance of the outflow and inflow rates of a jam, as required for its

stability [50]: The outflow rate of a continuous sequence of jammed cars is $1-p$, corresponding to the probability of acceleration of the car at the head of the jam. Because cars approach the rear of a jam with average velocity $v_{\mathrm{f}} = v_{\max} - p$, and the rear of the jam itself travels backwards at a speed equal to the inflow/outflow rate, this yields the transition density [50]

$$\rho_{\mathrm{tra}} = \frac{1-p}{v_{\max}+1-2p} \ . \tag{4.1}$$

The transition density shifts to smaller densities for larger values of p and reduces to $\rho_{\mathrm{tra}} \propto 1-p$ for small $1-p$; the stochasticity parameter p determines the onset of jammed traffic.

We relate the stochasticity parameter p to the temperature T of KCMs to explore interesting regimes in the dynamic arrest in traffic flow. For glasses and KCMs [51–53], it has been shown that the dynamic arrest becomes singular at $T = 0$, where the dynamics become deterministic. The case $T = 0$, where the dynamics of glasses freezes entirely, corresponds to the case $p = 1$, where cars always decelerate, and traffic flow arrests. In the limit of $T \to 0$ and $p \to 1$, the systems become deterministic. Although the NS-model has been studied extensively in the deterministic limit $p \to 0$ and for $0 < p < 1$, so far no complete study of the limit where cars always decelerate $p \to 1$ exists. This is what we provide in this chapter. We introduce some mathematical tools to study dynamic heterogeneities developed for glasses, and then apply them to the NS-model in the deterministic limit $p \to 1$ of the traffic model.

4.3 Dynamic susceptibility

A characteristic property of the glass is its dynamic heterogeneity. Dynamically active regions separate from dynamically less active regions in space and time, leading to increasing dynamic heterogeneity of the system. This dynamic heterogeneity is quantified by the dynamic susceptibility [54–56]. In analogy, we define the dynamic correlation function of traffic flow using

$$G_4(i,t) = \langle c(i;t)c(0;t)\rangle - \langle c(0;t)\rangle^2 \ , \tag{4.2}$$

where we take the mobility of car i as $c(i;t) = (1/(t+1)) \sum_{t'=0}^{t} v_i(t')$, its average velocity during the time interval $[0,t]$. We find that near $p = 1$, dynamic correlations become indeed increasingly long-ranged when the density approaches $\rho_{\rm tra}$. To investigate this increase in the correlation length, we define the dynamic susceptibility

$$\chi_4(t) = \frac{1}{\langle v^2 \rangle - \langle v \rangle^2} \sum_{i=0}^{N-1} G_4(i;t) \tag{4.3}$$

that measures the number of cars that move cooperatively on the time scale t. The dynamic susceptibility χ_4 indicates the size of regions of correlated mobility, and has been much used to measure dynamic heterogeneity in glasses and granular materials [57–60]. While in glasses maximum cooperative motion arises at intermediate time scales, at which the particles escape their dynamic confining cages, in traffic, the maximum dynamic susceptibility arises at the shortest time interval, see inset of Fig. 4.2(a).

4.4 Criticality at $p \to 1$

To explore the growth of correlations, we focus on $t = 0$, and show $\chi_4(t = 0)$ as a function of density in Fig. 4.2(a). Indeed, increasing maxima develop at $\rho \sim \rho_{\rm tra}$ as p approaches unity, indicating increasing dynamic correlations. The divergence of the dynamic susceptibility is clearly seen in Fig. 4.2(b), where we plot the maximum value of χ_4 as a function of $1 - p$. The figure shows data for various $v_{\rm max}$; in all cases, the maximum of χ_4, $\chi_{4,\rm max} \propto (1-p)^{-\nu}$, indicating that the number of cars that move cooperatively diverges. In the NS-model, the exponent appears to increase weakly with $v_{\rm max}$ changing from $\nu = 0.53$ to $\nu > 0.70$. This divergence indicates that traffic flow becomes truly critical in the limit $p \to 1$. The divergence is analogous to the one observed in KCMs at $T \to 0$, and indicates that the deterministic limits $p \to 1$ and $T \to 0$, are dynamical critical points of the systems. The divergence occurs at the onset of the jammed regime; to show this, in Fig. 4.2(c), we compare the location of the maximum of χ_4 (symbols) with the limiting ($p \to 1$) behavior of $\rho_{\rm tra}$ according to Eq. 4.1 (dashed lines).

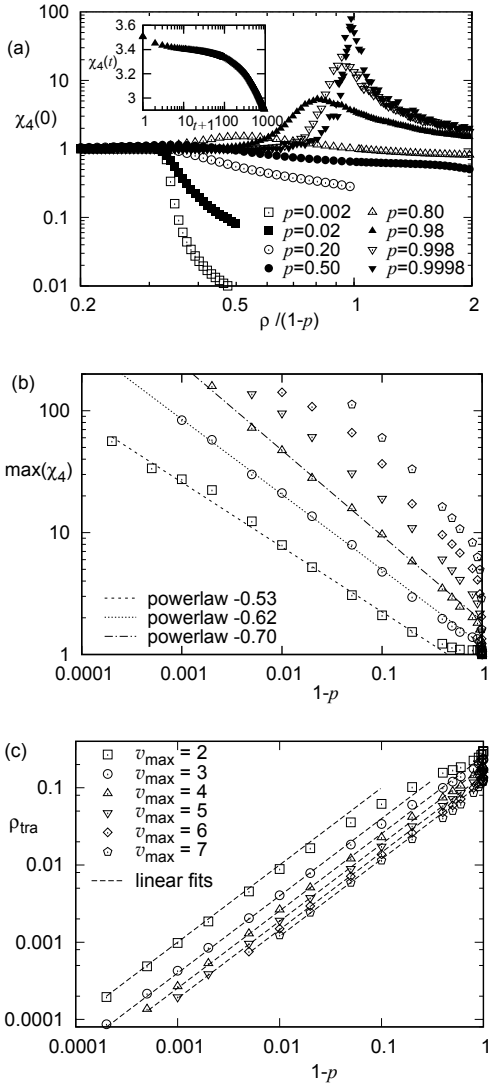

FIGURE 4.2: Dynamic susceptibility of traffic flow in the NS-model. (a) The value of $\chi_4(0)$ as a function of rescaled density for a range of probabilities p at $v_{\max} = 2$. The peak sharpens markedly as $p \to 1$. Inset: $\chi_4(t)$ as a function of time shows that the largest value occurs at $t = 0$. (b) Maximum value of $\chi_4(t = 0)$ as a function of the rescaled density, plotted vs. $1 - p$, for a set of $v_{\max}$ (symbols explained in (c)). Power-law behavior (dashed lines) indicates the divergence of the dynamic susceptibility on approach of the critical point $p = 1$. (c) Density of maximum dynamic susceptibility as a function of $1 - p$ for various values of $v_{\max}$. The position of the maximum is well described by the limiting behavior of (4.1), $\rho_{\text{tra}} = (1-p)/(v_{\max}-1)$ indicated by the dashed lines.

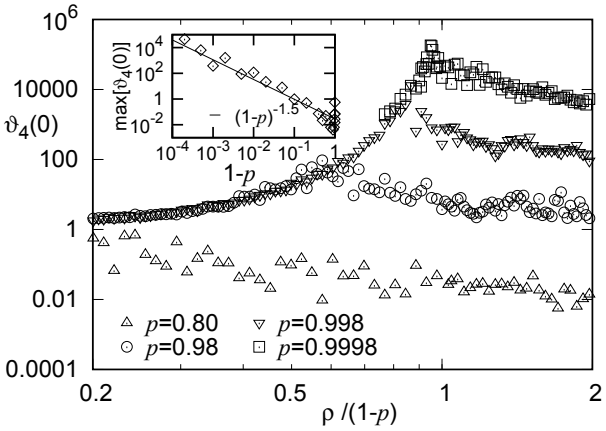

FIGURE 4.3: Residence time of cars in jams as a function of reduced density for various values of p at $v_{\max} = 2$. As $p \to 1$, the correlation time becomes more sharply peaked. Inset: Maximum residence time as a function of $1 - p$ shows power-law divergence of the correlation time for $p \to 1$.

Further evidence of critical behavior comes from measurement of the correlation *time* scale. To estimate the typical persistence time scale, we make use of a quantity similar to χ_4, where we interchange time and car index in the definition of $c(i;t)$ and in the sum appearing in Eq. 4.3, to obtain $\vartheta_4(i)$. The temporal susceptibility ϑ_4 indicates the correlation time scale of the system, and measures the typical residence time of a car in a jam. We plot this correlation time as a function of reduced density in Fig. 4.3. A strong increase of the maximum of ϑ_4 suggests that in addition to the divergence of the correlation length, there is also a divergence of the correlation *time* scale. This is confirmed by plotting the maximum values of ϑ_4 as a function of $(1 - p)$ in the inset. Similar to the spatial correlations, the correlation time scale diverges as a power law $\vartheta_{4,\max} = (1 - p)^{-\mu}$ as $p \to 1$, confirming that the system behaves critically along the time dimension. We determine the exponent to be $\mu \sim 1.5$. For real traffic, such diverging correlation time can have unpleasant consequences, as it indicates diverging persistence times of traffic jams.

4.5 Phase coexistence

We thus find a dynamical critical point characterized by diverging length and time scales. This critical point separates free flowing traffic from coexisting free flowing traffic and jams. This situation appears similar to equilibrium phase transitions, where the coexistence of phases is terminated by a critical point. To explore this analogy, we monitor the length of jams as a function of time, and find that indeed in the limit $p \to 1$, jams always coalesce in time to form a single jammed phase, coexisting with a single free flowing phase, analogous to the coarsening of equilibrium phases.

We explore this analogy further by defining the dynamical order parameter [61]

$$M = \frac{v_{\mathrm{f}} - \langle v \rangle}{v_{\mathrm{f}}} \ , \tag{4.4}$$

the normalized deviation of the average velocity from that of free flow. We show M as a function of the rescaled density in Fig. 4.4 for $v_{max} = 2$. It exhibits an increasingly sharp kink as $p \to 1$, but remains continuous at the transition $\rho = \rho_{\mathrm{tra}}$, indicating a singular point in the limit $p \to 1$. If we assume simple coexistence in the two-phase regime, we can predict the function $M(\rho) = (\rho - \rho_{\mathrm{tra}})/\rho$, which we indicate as a dashed line in Fig. 4.4. Indeed as $p \to 1$, there is strong evidence that the data converge to this simple function, supporting our picture of jam and free flowing traffic as coexisting phases. The functional dependence of this order parameter has an exponent $\beta = 1$, corresponding to a Bose condensate, and to condensates found in typical zero-range models [62]. We explore this condensate transition in general one-dimensional traffic and transport models further in the next chapter.

4.6 Conclusions

We established an analogy in the dynamic arrest of glasses and traffic, by identifying similar kinetic constraints in models of both systems. Inspired by this analogy between far from equilibrium systems, we demonstrated that the simple one-dimensional Nagel-Schreckenberg model for traffic flow exhibits hallmarks of a dynamic phase transition analogous to that of kinetically constrained models

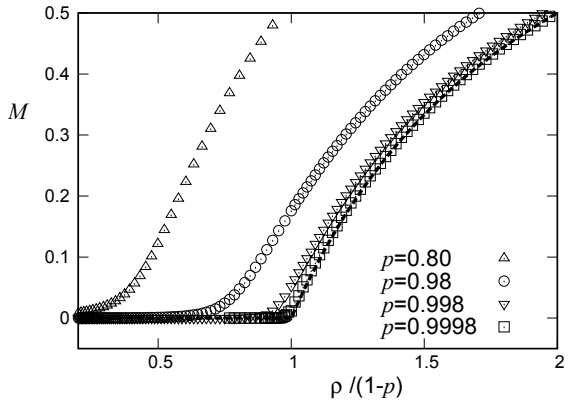

FIGURE 4.4: Order parameter M as a function of reduced density for various values of p at $v_{\max} = 2$. As $p \to 1$, the transition at $\rho = 1-p$ becomes singular. The dashed line shows the theoretical prediction $M = (\rho - \rho_{\mathrm{tra}})/\rho$.

for glasses. We identified a dynamical critical point in the deterministic limit $p \to 1$ and $\rho \to 0$ of the traffic model, marking the onset of coexisting jammed and free flowing traffic. The hallmark of this transition is the divergence of both correlation length and time scales. The direct analogy to KCMs of glasses points out the universality of dynamic arrest phenomena in systems far from equilibrium.

5

A criterion for dynamic phase coexistence in one-dimensional traffic and transport models

In the previous chapter we have demonstrated an analogy in the dynamic arrest of glasses and traffic. We found critical behavior at the onset of coexistence of jammed and free flowing traffic, where all jammed traffic condensates into a single region. Condensation is observed in various models of driven systems, but only understood in certain exactly solvable models. In this chapter we study this condensation in one-dimensional transport models, such as the Nagel-Schreckenberg model discussed in the previous chapter. We develop an analytic criterion for its occurrence. The kinetic constraint central to these models results in clustering of immobile vehicles; these clusters can grow to macroscopic condensates, indicating the onset of dynamic phase coexistence of free flowing and arrested traffic. We investigate analytically the conditions under which this occurs, and derive a necessary and sufficient criterion for phase coexistence. By applying this criterion to the Nagel-Schreckenberg model of traffic flow, we find that true phase coexistence only occurs when acceleration out of jammed traffic happens in a single time step, in the limit of strong over-braking. This provides deeper insight into the critical behavior of the NS-model we found in chapter 4.

5.1 Introduction

Dynamic arrest in driven systems can result in strong dynamic heterogeneities, where mobile and immobile particles separate in space: immobile particles tend to cluster and form high density regions. An intriguing question in this context is how big a cluster of immobile particles can be. In the previous chapter, we measured the cluster size of correlated mobility in a traffic model by calculating the dynamic susceptibility. The size of clusters was found to diverge in the limit of overcautious driving. In this chapter we set out to understand why the cluster size diverges for overcautious driving. We do this by describing the cluster growth, creation and shrinkage in one-dimensional driven transport models from the microscopic particle interactions and dynamics. These rate equations allow us to conclude whether clusters of slow particles can become infinitely large, that is: condensation occurs. These condensates in real space do typically not occupy all of space, but coexist with free moving particles, therefore the criterion for condensation derived in this chapter is equivalently a criterion for phase coexistence.

Whether and how dynamic condensation occurs remains a largely open question. So far, it can only be addressed analytically in certain exactly solvable models [62–65]. In these models, the dynamics of particles is typically specified per lattice site: particles can accumulate on a given site while hopping from one site to the next. It has been shown analytically that these systems exhibit condensation and symmetry breaking, even in one dimension. In traffic models the situation is, however, different since vehicles must follow each other and cannot accumulate on any site. In these models, the vehicle dynamics are set by a kinetic constraint between neighboring particles that guarantees vehicles do not collide. The question is how condensation occurs in these models, and how it can be analytically predicted based on the microscopic interactions of the vehicles or particles. Although some attempts have been made to connect traffic models with exactly solvable models [66, 67], a general analytic treatment of condensation in one-dimensional transport models is lacking.

In this chapter, we present an analytic criterion of condensate formation in traffic models, applicable both to traffic and more general driven systems. We establish

a criterion for the occurrence of extensively large jams as a function of the microscopic interactions of the traffic model. Because of the generality of the equations used, the criterion is generally applicable to traffic and transport models. We gain insight into the dynamics of jam creation, lifetime and size. We apply this criterion to the Nagel-Schreckenberg (NS) [6] model and related models of traffic flow to investigate analytically if and how condensation occurs, hence answering the longstanding question of dynamic condensates in these models [68]. We indeed confirm analytically that condensates form in the limit of high braking probability, as studied by simulations in the previous chapter. In all other cases, arrested clusters either dissolve or split up. We illustrate the growth dynamics of these arrested clusters using long simulation runs, and demonstrate the similarity to the dynamics of a diffusion process.

5.2 Criterion

5.2.1 Class of Models

Like in the previous chapter, we consider kinetically constrained one-dimensional transport models that are defined by mass-conserving local dynamical rules. Here we consider in general models with the following defining dynamics: particles move unidirectionally over a discrete lattice in discrete time. A particle can move freely when it is out of the interaction range of other particles, but becomes kinetically constrained when it closely approaches particles. The kinetic constraint can, for example, be a hard-core repulsion between neighboring particles, like in the glass and traffic models discussed in the previous chapter, but "softer" constraints with longer range are also possible, as long as the order of the particles is conserved. Once the kinetic constraint is released, particles accelerate with a certain probability to become free flowing. We call the free flowing particles "active", and the kinetically constrained or dynamically arrested particles "inactive". To derive the criterion for condensation, we consider the bulk of an infinitely extended lattice.

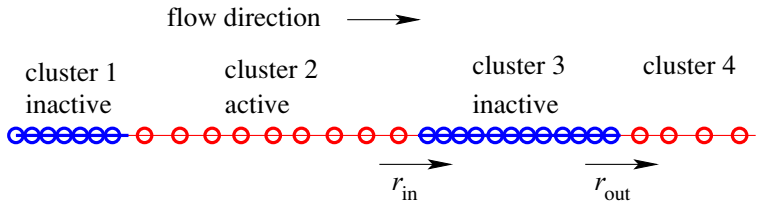

FIGURE 5.1: Schematic of particle clustering and flow rates in mass transport models. The dynamic particle interactions lead to clustering of immobile (inactive) particles. These inactive clusters coexist with clusters of mobile (active) particles. A few coexisting clusters are shown, as well as the inflow and outflow rate r_{in} and r_{out} of particles at the upstream and downstream boundary of an inactive cluster. The average distance between particles in active clusters must be larger than the interaction distance, while the distance between inactive particles is typically smaller than the interaction distance.

5.2.2 Derivation of Criterion

Inactive particles form clusters due to their dynamic interaction. Here, we define a cluster as a sequence of particles in the same state (active or inactive). A typical particle configuration consists of several coexisting active and inactive clusters as shown in Fig. 5.1. These clusters can grow and eventually reach macroscopic size. We call an inactive cluster a condensate, if in the limit of infinite system size, the cluster contains an infinite number of particles. Here, we allow short-lived interruptions in the sequence of inactive particles that exist on a timescale much shorter than the typical timescale of growth or shrinkage of the cluster. We call such small and short-lived interruptions bubbles, in analogy to fluctuations in an equilibrium liquid phase.

We investigate the conditions under which condensation occurs in the stationary state in an infinitely extended system, by analyzing the growth dynamics of inactive clusters. The control parameters are the global particle density ρ and the fluctuation parameter(s). We deduce the dynamics of clusters of particles from the microscopic dynamics of the particles.

There are several competing processes that lead to growth or shrinkage of clusters. Clusters can grow one by one by particles leaving or entering at the boundaries (see cluster 3 in Fig. 5.1). Clusters can also split up into two by particles changing their state inside a cluster. Finally, two clusters can merge when the cluster that separates them shrinks to zero.

Below we will analyze these cluster processes in detail to find the condition for condensation. The idea is as follows: 1. Inactive clusters must be unable to split up to become infinitely large. 2. Inactive clusters must grow, i.e. their growth rate must be at least as large as their shrink rate. The growth of existing clusters is, however, reduced by any new inactive cluster that forms upstream; such a new inactive cluster takes up particles and reduces the inflow to existing downstream inactive clusters.

These two conditions have to be met independently: because the split-up rate of clusters scales with the cluster size, while the growth rate of clusters does not (it is always limited to maximum 1 particle per time-step), the two processes cannot balance, and both conditions must be fulfilled simultaneously.

Splitting up of inactive clusters

We first investigate the split-up of inactive clusters. Split-up occurs when the distance between inactive particles increases spontaneously releasing the kinetic constraint. Such split-up is detrimental for condensation. Below, we identify two alternative conditions that prevent split-up. One of these must be satisfied to guarantee split-up does not occur.

First, if the density inside active clusters is maximum, $\rho_{\mathrm{ina}} = \rho_{\max}$, so that density fluctuations inside the cluster do not occur, then split-up cannot occur. For hard-core repulsion, we have $\rho_{\max} = 1$ [1].

Second, if ρ_{ina} is lower than $\rho_{\max}$, density fluctuations do exist, but condensation will still occur if these density fluctuations are short-lived, i.e. no stable active cluster can form within an inactive cluster. This is the case when the density of inactive clusters is much larger than that of active ones, i.e. when $\rho_{\mathrm{act}}/\rho_{\mathrm{ina}} \to 0$. In this case, any active "bubble" requires an infinite amount of space; that much space is not available inside inactive clusters; as a result inactive clusters do not split up.

We thus obtain the following condition for condensation:

$$\rho_{\mathrm{ina}} = \rho_{\max} \quad \text{OR} \quad \frac{\rho_{\mathrm{act}}}{\rho_{\mathrm{ina}}} \to 0 \ , \tag{5.1}$$

[1] It is possible to construct systems that have a range of densities that make fluctuations impossible. In this case, by $\rho_{\max}$ we mean any density in this range.

where the limit here and in all equations below is taken with respect to the fluctuation parameter for a given particle density ρ. We note that this condition also implies that inactive clusters cannot merge.

Growth versus creation of inactive clusters

We now consider the processes that grow and shrink the inactive cluster due to in- and outflow of single particles. An inactive cluster grows due to particles entering at the upstream boundary at rate r_{in}, while it shrinks due to particles leaving the cluster at the downstream boundary with rate r_{out}, see cluster 3 in Fig. 5.1. These two processes grow and shrink the inactive cluster, respectively, with rates r_+ and r_-. Because by definition $\Delta t = 1$, rates equal probabilities, and we can write:

$$r_+ = r_{\text{in}}(1 - r_{\text{out}}) \ , \tag{5.2}$$

$$r_- = (1 - r_{\text{in}})r_{\text{out}} \ . \tag{5.3}$$

In steady-state, $r_+ > r_-$ is not possible due to particle conservation. A steady-state with cluster rates $r_+ < r_-$ is possible, but implies that all inactive clusters have a finite size and lifetime. This leaves us with $r_+ = r_-$ as the only possible condition with a condensate in the steady-state. This means, for condensation to occur, the difference $\Delta r = r_- - r_+$ must vanish relative to the absolute value of r_+ or r_- that sets the typical time scale of the system. Hence

$$\frac{r_- - r_+}{r_-} = \frac{\Delta r}{r_-} \to 0 \ . \tag{5.4}$$

The task is now to find an expression for Δr in terms of basic dynamical quantities. We rewrite Δr using Eqs. (5.2) and (5.3) to relate it to the in- and outflow rate of particles,

$$\Delta r = (1 - r_{\text{in}})r_{\text{out}} - r_{\text{in}}(1 - r_{\text{out}}) = r_{\text{out}} - r_{\text{in}}. \tag{5.5}$$

Here, the inflow rate r_{in} of the inactive cluster (cluster 3 in fig. 5.1) is given by the average flow rate through the upstream active cluster (cluster 2 in Fig. 5.1), i.e. the average velocity $\tilde{v}$ of particles in the active cluster times their average density $\tilde{\rho}$. Because the boundary between both clusters moves itself with (negative)

velocity v_c, this increases the relative velocity of inflowing particles to $(\tilde{v} - v_c)$, and the inflow rate becomes

$$r_{in} = \tilde{\rho}(\tilde{v} - v_c). \tag{5.6}$$

The average density $\tilde{\rho}$ itself depends on the outflow rate of the next upstream inactive cluster (cluster 1 in Fig. 5.1): the outflow rate, r_{out}, of cluster 1 equals the velocity, v_{act} of active particles, times the density, $\tilde{\rho}$ [2]. This allows us to find a corresponding relation for the boundary between cluster 1 and cluster 2, which we rewrite to obtain for the density $\tilde{\rho}$ in cluster 2:

$$\tilde{\rho} = \frac{r_{out}}{v_{act} - v_c}. \tag{5.7}$$

Due to fluctuations, new inactive clusters may form inside the active cluster (technically splitting up the active cluster). This reduces the velocity of particles in this region. To obtain an expression for the resulting average velocity $\tilde{v}$ in this region, which now consists of active and inactive clusters, we introduce the fraction $\tilde{f}$ of inactive particles. We can then write

$$\tilde{v} = \tilde{f} v_{ina} + (1 - \tilde{f}) v_{act} \ . \tag{5.8}$$

By inserting Eqs. (5.6) - (5.8) in Eq. 5.5, we find that

$$\Delta r = r_{out} - \frac{r_{out}}{v_{act} - v_c}[\tilde{f}(v_{ina} - v_c) + (1 - \tilde{f})(v_{act} - v_c)] \ , \tag{5.9}$$

$$= r_{out}\tilde{f}\frac{v_{act} - v_{ina}}{v_{act} - v_c} \ , \tag{5.10}$$

which relates Δr to the particle velocities and outflow rates. Finally, we express the fraction $\tilde{f}$ of inactive particles in terms of the creation rate u per particle of inactive clusters, their average lifetime, T, and their average length, n. In steady-state this fraction is

$$\tilde{f} = uTn \ . \tag{5.11}$$

[2] Here we have used that in steady-state, the outflow rates of inactive clusters 1 and 3 are the same.

Using Eqs. (5.10) and (5.11), our criterion for the growth rate of clusters (Eq. 5.4) then becomes

$$\frac{\Delta r}{r_-} = \frac{r_{\text{out}} uTn(v_{\text{act}} - v_{\text{ina}})}{r_-(v_{\text{act}} - v_{\text{c}})} \to 0 \ , \tag{5.12}$$

which simplifies to

$$\frac{r_{\text{out}} uTn}{r_-} \to 0 \ , \tag{5.13}$$

because $v_{\text{act}} > v_{\text{ina}}$ and $v_{\text{c}} < 0$, and all velocities are finite. Eq. 5.13 provides the second criterion for condensation. It ensures that the growth rate of inactive clusters is at least as large as their shrink rate, so that inactive clusters can be stable [3].

We thus arrive at a twofold criterion for condensate formation, consisting of Eqs. (5.1) and (5.13). The first equation guarantees that inactive clusters do not split up; the second equation assures that the growth of inactive clusters is not hindered by the formation of new inactive clusters. Together, these two equations provide a necessary and sufficient condition for condensation.

5.3 Application to traffic model

We now apply the criterion, Eqs. (5.1) and (5.13), to specific traffic models to demonstrate the occurrence or absence of dynamic condensates. In particular, we continue our study of the Nagel-Schreckenberg model [6].

5.3.1 Nagel-Schreckenberg model

A detailed description of the NS-model can be found in chapters 3 and 4. Cars in the NS-model tend to accelerate and maintain a maximum velocity v_{max}. Collisions are avoided by a hard-core kinetic constraint. Depending on the values of the fluctuation parameter p and the car density ρ the dynamics results in phases consisting of free flowing traffic or free flow coexisting with jams. Here,

[3] We note that in order to derive Eq. 5.13, we assumed high density. For $\rho < \frac{r_{\text{out}}}{v_{\text{act}} - v_{\text{c}}}$, it follows from Eqs. (5.7) and (5.8) that $r_{\text{in}} < r_{\text{out}}$, so no condensation can occur.

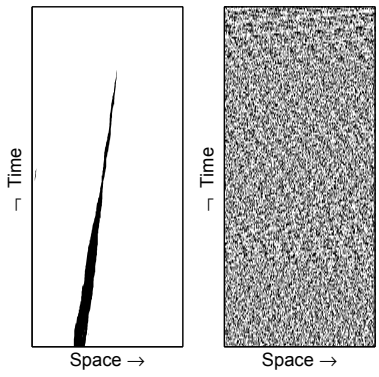

FIGURE 5.2: Space-time diagram of vehicles in the two deterministic limits of the NS-model, for $p = 0.9998$ (a) and $p = 0.0002$ (b). Inactive vehicles are indicated in black. The horizontal axis represents the car index. The simulations are performed at densities 20 % above the transition density ρ_{tra}.

we analytically address the spatial organization of traffic jams with the criterion introduced above: for which values of p and ρ does condensation occur?

From simulations the idea has emerged that no sharp transition between free flow and jammed traffic occurs for finite stochasticity $0 < p < 1$. [45–47]. This implies that there is no condensate. Condensates might, however, form in the deterministic limits $p \to 1$ and $p \to 0$ of the model. Numerically, no such condensation has been found in the limit $p \to 0$. Our results in chapter 4 do suggest that condensation occurs in the limit $p \to 1$, at least for $v_{\max} = 2$ [69]. To appreciate the strikingly different behavior in the two deterministic limits, we show space-time diagrams constructed from simulations for $v_{\max} = 2$ in Fig. 5.2. In the limit $p \to 1$, a condensate forms as illustrated by the thick black line in Fig. 5.2(a). A jam nucleates and grows into a condensate that contains all excess particles above the critical density. In contrast, in the limit $p \to 0$, there are many small jams (Fig. 5.2(b)) that do not coalesce, and no macroscopic condensate forms. Some jams disappear and new jams are created. Below we investigate analytically the formation of condensates for all different cases of p, starting with $v_{\max} = 2$.

5.3.2 Nagel-Schreckenberg with $0 < p < 1$ ($v_{max} = 2$)

Simulations suggest that for finite stochasticity, $0 < p < 1$, there is no condensate. Indeed we will show that in this case, the second condition (Eq. 5.13) is not fulfilled. To see this, we first note that for finite p, vehicles slow down randomly, and the average velocity is smaller than v_{max}. Hence, the inflow rate of jams, r_{in}, is smaller than 1. Since we can rewrite $r_{\text{out}}/r_{-} = 1/(1 - r_{\text{in}})$ using Eq. 5.3, we conclude that the first factor in Eq. 5.13, $r_{\text{out}}/r_{-} > 0$.

Furthermore, also $u > 0$: due to velocity fluctuations at finite p, the distances between cars varies and cars can come within the interaction range with finite probability. Hence, new jams are formed even at arbitrarily low density and $u > 0$.

Because the remaining factors in Eq. 5.13, T and n, are always larger than zero (a jam always exists for at least one time step and consists of at least one car), we conclude that Eq. 5.13 is not fulfilled and thus there is no condensate. This is in agreement with the consensus in the literature about the absence of a sharp transition between free flowing and jammed traffic for $0 < p < 1$ [45–47].

5.3.3 Nagel-Schreckenberg in the limit $p \to 1$ ($v_{max} = 2$)

In the limit $p \to 1$, cars almost always over-brake. To determine whether condensation occurs in this limit, we analyze the scaling of all quantities in Eqs. (5.1) and (5.13) as a function of the vanishing distance to the deterministic point: $\Delta p = 1 - p \to 0$.

With $v_{max} = 2$ and $p \to 1$, free flowing traffic has average velocity $v_{max} - p = 1$, and jammed traffic has velocity 0. Hence, cars accelerate in a single step out of the inactive cluster, and the outflow rate equals the probability of acceleration, $r_{\text{out}} = \Delta p$. According to Eq. 5.7, it then follows that the density in active clusters scales as $\rho_{\text{act}} \sim \Delta p$. Meanwhile, the density of a jam, ρ_{ina}, is bounded from below due to the finite interaction range, and must be higher than $1/v_{\text{max}}$. Consequently, the second part of Eq. 5.1 is fulfilled, meaning that inactive clusters do not split up.

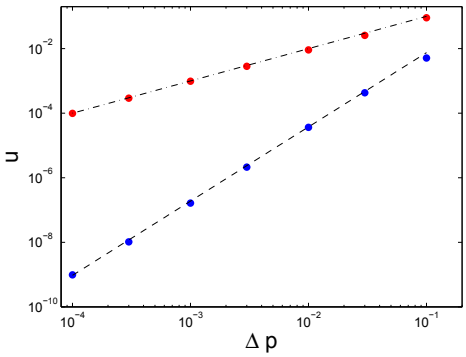

FIGURE 5.3: Creation rate per car of new jams as a function of the distance Δp to the deterministic point $p \to 0$ (red points, $\Delta p = p$) and $p \to 1$ (blue points, $\Delta p = 1 - p$). The dashed lines have slope 1 (red data points) and slope 2.3 (blue data points).

To check the second part, Eq. 5.13, we note that because $r_{in} \to 0$ in the limit $p \to 1$, we can approximate $r_- = (1 - r_{\text{in}}) r_{\text{out}} \approx r_{\text{out}}$. We thus find that

$$\frac{r_{\text{out}} u T n}{r_-} \to u T n \ . \tag{5.14}$$

reducing the criterion to the scaling of u, T and n.

The scaling of u can be estimated as follows: The distance between cars behaves as a diffusion process. Hence, we can estimate the creation rate u of new jams from the time τ it takes for the root mean square of the change Δd of the distance d between subsequent cars to grow to the average distance itself: $\Delta d \approx \langle d \rangle$. For a random walker, the number of changes necessary to accumulate a change of $\langle d \rangle$ is $\langle d \rangle^2$, while for ballistic motion, the number of changes is $\langle d \rangle$. We will allow for a general power $\langle d \rangle^\beta$. Because the time to change the distance between two cars by one is of order $(\Delta p)^{-1}$, we obtain

$$\tau \sim \Delta p^{-1-\beta}. \tag{5.15}$$

Because $u \approx 1/\tau$, we obtain $u \approx \Delta p^{\beta+1}$. With simulations we find $u \sim \Delta p^{2.3 \pm 0.1}$ (Fig. 5.3), and hence $\beta = 1.3$, an exponent between random walk and ballistic motion. The quantity u thus vanishes on approach of the deterministic point.

We now consider the scaling of n. A divergence of n by definition means that condensation occurs, since n indicates the number of cars in a jam. Therefore,

the maximum scaling of n that does not *a priori* indicate condensation, is that n is constant. We will take this maximum scaling, and will show below that, nevertheless, condensation occurs.

The scaling of T, the average lifetime of jams, can be estimated from the average time it takes for a car to accelerate out of a jam; this time diverges as $1/r_{\text{out}} = 1/\Delta p$. Hence, the average jam lifetime scales as $T \sim \mathcal{O}(\Delta p^{-1})$ if n is constant; any faster decrease would imply that the number of cars in a jam grows and thus again that a condensate forms.

With the scaling obtained for u, n and T, Eq. 5.14 becomes

$$uTn \sim \Delta p^{\beta} \ . \tag{5.16}$$

This quantity goes to zero in the limit $\Delta p \to 0$, thus meeting the requirement for condensation. We therefore expect condensation to occur in the limit $p \to 1$, in agreement with the simulation results shown in Fig. 5.2 and in the previous chapter.

It is interesting to investigate the time dependence of the condensation process. In Fig. 5.4, we plot the number of jams and the growth of the largest jam as a function of time. For p close to 1, the number of cars in the largest jam increases with a power of 1/2, while the number of jams decreases accordingly. This power-law scaling is reminiscent of the diffusive dynamics of the random-walk process, in which the probability of attachment of a car equals that of detachment. Indeed, we have shown above that a necessary criterion for condensation is $r_+ = r_-$, i.e. inactive clusters increase or decrease with equal probability. This analogy between the size of jams and the position of a random walker was pointed out before by Nagel and Paczuski for the cruise control limit of the NS-model [49], and our analytical model predicts it as a necessary condition. We thus find that our criterion concludes correctly on the existence of dynamic condensates, and predicts the dynamics of their growth through a random-walk process.

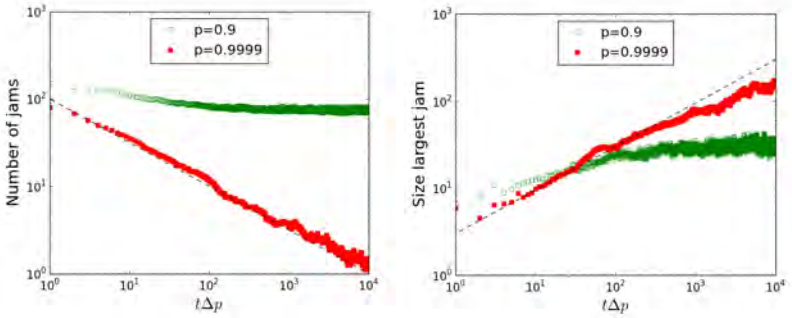

(a) (b)

FIGURE 5.4: Time evolution of jams for p approaching 1. (a) Number of cars in the largest jam versus time. The dashed line has slope $-1/2$. (b) Number of jams versus time. The dashed line has slope $1/2$. The jam size diverges and the number of jams decreases over time indicating condensate formation.

5.3.4 Nagel-Schreckenberg in the limit $p \to 0$ ($v_{max} = 2$)

Simulations suggest that in this limit, no condensate forms [40, 61]. We will address this issue with the criterion starting with Eq. 5.13. For $p \to 0$, the braking probability p is vanishingly small. As a result, the outflow rate of jams $r_{\text{out}} = 1-p$. Using $r_{\text{in}} = r_{\text{out}} - \Delta r$, we can hence approximate $r_- = r_{\text{out}}(1-r_{\text{in}}) \approx p + \Delta r$. *A priori* we do not know which term dominates the scaling of r_- when p vanishes: p or Δr. If Δr determines the scaling, we immediately see that the left-hand side of Eq. 5.12: $\Delta r/r_- = \Delta r/\Delta r \neq 0$ and there is no condensation. If p determines the scaling, we can simplify Eq. 5.13 as follows: Because the outflow rate is close to unity, the density of free flow is high and any random slow down of a car immediately causes the upstream neighbor to become kinetically constrained. Because this happens with probability p, the jam creation rate per car is $u \sim p$, as is also shown by the simulation results in Fig. 5.3. With $u \sim p$, $r_- \sim p$ and $r_{\text{out}} \approx 1$, Eq. 5.13 becomes:

$$\frac{r_{\text{out}} u T n}{r_-} \sim T n \ . \tag{5.17}$$

Since both $T > 0$ and $n > 0$, we conclude that there is no condensation in the limit $p \to 0$, in agreement with the simulation results [40, 61].

5.3.5 Nagel-Schreckenberg with $v_{\max} > 2$

It is frequently assumed that the NS-model behaves qualitatively similar when changing $v_{\max}$ [42, 43]. Here, we will investigate this analytically and find that in the limit $p \to 1$ there is a qualitative difference. Surprisingly, for $v_{\max} > 2$, there is no condensation in this limit, in contrast to $v_{\max} = 2$.

To see this, we note that for $v_{\max} = 2$ acceleration from jam to free flow occurs in a single step. Therefore, an accelerating car immediately leaves the jam, keeping the density of the jam finite. In contrast, for $v_{\max} > 2$, the acceleration needs multiple steps in the limit $p \to 1$. A car leaving the jam is still part of the jam until it reaches the maximum velocity. This lowers the density of jams, and leaves Eq. 5.1 unfulfilled. In the spaces created inside the jam, new free flow can emerge that splits up the jam. This mechanism prevents the formation of an infinitely large jam.

We demonstrate the split up of jams in the space-time diagram obtained in simulations, see Fig. 5.5. The simulation starts from random initial car positions; after a jam has nucleated, it grows, but shortly after that, the first free flow starts to appear inside the jam. This becomes most obvious in Fig. 5.5(b), where we show a magnified section at early times. All free flow 'bubbles' inside the jam clearly emerge at the downstream boundary of the jam. This free flow is persistent and covers larger regions at later times. These pictures demonstrate that there is no single macroscopic condensate for $v_{\max} > 2$.

We confirm the absence of condensation for $v_{\max} = 3$ numerically by studying the number of cars in the largest jams in simulations, see Fig. 5.6. In contrast to $v_{\max} = 2$ (Fig. 5.4(b)), the number of cars no longer diverges as p approaches 1, i.e. the data is not any more approaching the asymptotic line. The curves for all p overlap, demonstrating the absence of condensation, and the qualitative difference to $v_{\max} = 2$.

To complete the analytical discussion of the NS-model we shortly comment on the limits $0 < p < 1$ and $p \to 0$ for $v_{\max} > 2$. In both cases, the argument is similar to that of $v_{\max} = 2$. For $0 < p < 1$, fluctuations in velocity create fluctuations in distances between free flowing cars. As a result, the creation rate of jams $u > 0$. In the limit $p \to 0$ the creation rate of jams vanishes with p, $u \sim p$, but the growth rate of jams vanishes just as quickly, so there is no condensation.

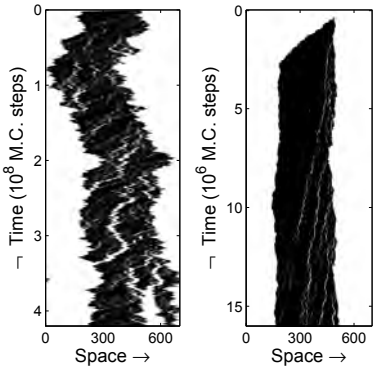

(a) (b)

FIGURE 5.5: Space-time diagram of vehicles in the NS-model with $p = 0.9998$ and $v_{\max} = 3$. (a) Entire simulation run and (b) enlarged section at early times. Inactive cars are shown in black. Horizontal axis represents car index; to follow the evolution of jams, we plot the space-time diagram in a frame co-moving with the speed of jams. Time is measured in Monte Carlo (M.C.) steps. The emerging white regions inside the jam indicate a split up of the original jam that becomes more pronounced at later times. The enlarged section in (b) shows that this split-up emerges at the downstream boundary of the jam.

In summary, the surprising conclusion of our analytical treatment of the NS-model is that only in the case $v_{\max} = 2$ (limit $p \to 1$) there is a true condensate transition.

5.3.6 Application to Velocity Dependent Randomization model

An extension of the Nagel-Schreckenberg model is the Velocity Dependent Randomization (VDR) model, in which there are *two* fluctuation parameters instead of *one*: p_{f} controls the fluctuations in free flow, while p_{j} controls the fluctuations of jammed traffic. This model takes account of the fact that drivers may behave differently depending on the traffic context, free flowing or jammed. We will show that in this model, where we have two control parameters, one for the creation rate and one for the growth rate of clusters, there is a condensate even in the limit $p_f, p_j \to 0$.

To do so, we use simulations to determine the size of the largest jam as a function of p_j and p_f. To incorporate both p_f and p_j, we modify the NS-model update

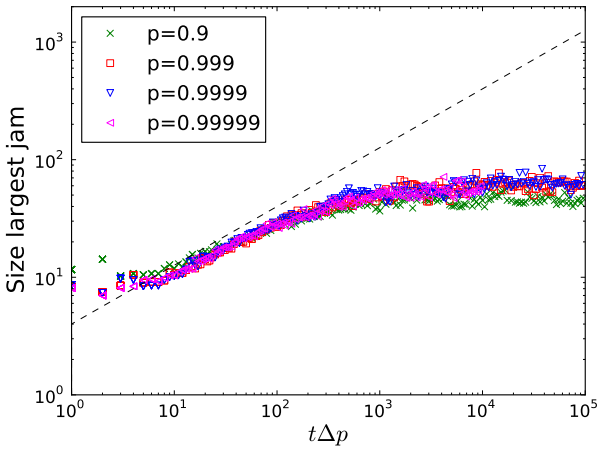

FIGURE 5.6: Time evolution of the number of cars in the largest jam for $v_{\max} = 3$, for values of p approaching 1. The dashed line has slope 1/2. The jam size does not diverge; the data for all p approaching 1 overlap.

scheme by adding an extra step before the randomization step 3. If car i is jammed ($v_i < v_{\max}$ after step 2) then $p = p_j$, and if car i is free flowing ($v_i = v_{\max}$) then $p = p_f$. Further, the update scheme is identical to the NS update scheme. We plot the number of jams in a two-dimensional contour plot in Fig. 5.7. This plot shows to which extent jams cluster and that all jammed cars form a condensate if

$$\frac{p_f}{p_j} \to 0 \ . \tag{5.18}$$

This numerical finding is indeed in line with the qualitative argument that the creation rate of new jams, controlled by p_f, must vanish faster than the growth rate of jams, controlled by p_j. This finding thus again demonstrates the principle of the criterion for condensation.

5.4 Conclusions

We have derived a criterion for condensation in one-dimensional transport models with a kinetic constraint that causes clustering of dynamically arrested particles. Whether this clustering leads to macroscopic phase coexistence depends on two

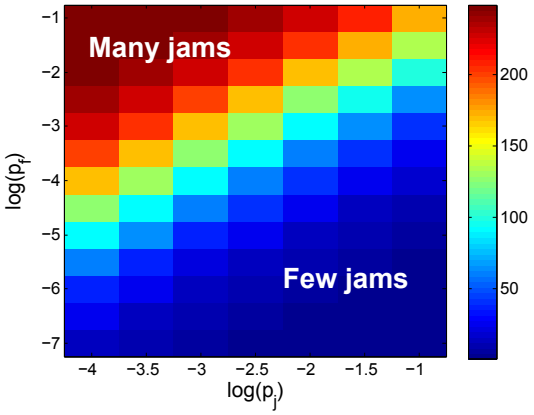

FIGURE 5.7: Diagram illustrating the number jams (see color bar) as a function of p_f and p_j in the velocity-dependent randomization model. Simulations were performed with 1000 cars at density $\rho = 0.4$. The diagram is plotted in the region close to $p_f \to 0$ and $p_j \to 0$. Whether a condensate forms depends on how the limit to zero is taken. The decreasing number of jams in the limit $p_f/p_j \to 0$ shows that a condensate forms in this limit.

factors: Firstly, density fluctuations in inactive clusters must be small enough to prevent the split-up of inactive clusters. Secondly, the growth rate of inactive clusters must dominate the formation rate of new inactive clusters since those reduce the inflow of existing clusters downstream.

The latter condition means that condensation is only possible if the growth rate of inactive clusters equals their shrink rate. This establishes a generic analogy of the size of inactive clusters to the position of a random walker, that was previously found by Nagel and Paczuski [49] and Barlovic *et al.* [70] for specific models. With this analogy we can explain the growth dynamics of condensates as well as the distribution of lifetimes and sizes of inactive clusters upon condensation.

We have applied the criterion to the well-known Nagel-Schreckenberg traffic model and confirmed that a condensation transition occurs in the limit $p \to 1$ with $v_{\max} = 2$, as suggested by the numerical study of this limit in the previous chapter. In all other cases traffic jams are finite. We note that nevertheless, there can be a discontinuity in the mean velocity of cars [61] or its derivative, reflecting a sudden onset of jams.

A wider applicability of the criterion is demonstrated by analyzing condensation

in the Velocity Dependent Randomization model, in which the creation rate of new traffic jams is controlled by two stochastic parameters, one for the fluctuations of free flowing traffic (p_f), and one for those of jammed traffic (p_j). Exploring both parameters, we demonstrated a new condensate transition in the limit $p_f, p_j \to 0$ if p_f vanishes faster than p_j, in agreement with the idea behind our criterion for condensation.

6

Shear banding of colloidal glasses - Observation of dynamic phase coexistence

In this chapter we study shear banding in a colloidal glass driven by a shear force. Particles with different flow rates spatially separate into two dynamic bands. In the preceding chapter we found analytical conditions for phase coexistence of slow and fast particles in one-dimensional driven systems, based on the intrinsic flow rates of a system. In this chapter, we show three dimensional microscopy observations of phase coexistence in a colloidal glass. By following the particle dynamics as a function of the driving field, we identify a critical shear rate at which the transition from homogeneous to heterogeneous flow occurs. We relate the critical shear rate for the driven glass to the intrinsic flow rates of the system, to rationalize when phase coexistence occurs. Using a new dynamic order parameter, we characterize the dynamics in each band. We demonstrate that although the transition is mostly of dynamic origin, small structural changes occur.

6.1 Introduction

Application of stress on an amorphous material results in rich flow behavior, which is extensively studied in the field of rheology. While stress-strain relations have been studied extensively due to the large application potential of glasses, only recently is the microscopic mechanism of flow being slowly uncovered. A particularly intriguing but well-known phenomenon is that of shear banding [10, 71–75], where the shear localizes in bands that flow at much increased rate. This phenomenon has long been recognized in metallic glasses [71], for which intriguing liquid vein patterns have been observed along the shear bands [72]. Despite its importance to a wide range of amorphous materials including metallic and soft glasses, a fundamental understanding of shear banding is lacking.

Phenomenologically, shear banding is associated with non-monotonous flow curves [9, 10]: the stress to maintain a steady-state flow of the material varies non-monotonically with applied strain rate. This leads to two (or more) flow rates that coexist at the same applied stress, analogous to the Van der Waals description of coexisting gas and liquid. While such non-monotonous flow curves have been recently measured in colloidal glasses [76], the microscopic origin of shear banding remains unclear; in particular it is unclear whether and how shear banding is related to structural and dynamic properties of the glassy state. Structural differences between different glassy states are small, often below the resolution limit, and direct observation of the atomic dynamics in molecular glasses is prohibitively difficult.

Colloidal glasses allow direct observation of single particle dynamics, offering particle trajectories to be followed at long time and large length scales [77, 78]. The constituent particles exhibit dynamic arrest due to crowding at volume fractions larger than $\phi_g \sim 0.58$, the colloidal glass transition [14, 79]. These systems exhibit glass-like properties such as non-ergodicity and aging [80]. Recent work has shown that when sheared slowly, (colloidal) glasses show long-range correlations in their dynamics [81], demonstrating the high dynamic susceptibility of the sheared material, much like the flowing, dense traffic close to the onset of jamming discussed in the previous chapters. Moreover, recent combined rheology and structure measurements [76] have revealed non-monotonous flow curves and steady-state shear banding in these systems. The onset of shear banding

occurred at shear rates of around the inverse structural relaxation time of the glass. The connection between the rate imposed by the driving force and the intrinsic dynamic properties is analogous to that in one-dimensional driven systems identified in the previous chapter. This suggests a deep connection between the intrinsic and external rates of driven systems.

In this chapter, we use direct observation of single particle dynamics in a colloidal glass to investigate this intriguing dynamic transition. We demonstrate the existence of a critical shear rate, at which the glass separates into two dynamic bands characterized by distinct diffusion time scales. We measure a new dynamic order parameter [82] to demonstrate the coexistence of two dynamic phases. We show that this dynamic transition is accompanied by a weak, but characteristic structural modification of the glass.

6.2 Experiments

The colloidal glass consists of PMMA particles with a diameter of $\sigma = 1.3\mu m$, and a polydisperity of 7%, suspended in a density and refractive index matched solution. A dense suspension with particle volume fraction $\phi \sim 0.60$ well inside the glassy state is prepared by diluting suspensions centrifuged to a sediment. The suspension is loaded in a cell of which the top plate can move to apply shear at constant rates between $\dot{\gamma} = 1.5 \times 10^{-5}$ and $2.2 \times 10^{-4} s^{-1}$. Confocal microscopy is used to image the individual particles, and determine their positions in three dimensions. All measurements presented here are recorded in the steady-state regime, after the sample has been sheared to $\gamma \sim 1$. We use the structural relaxation time $\tau = 2 \times 10^4 s$ [81] of the quiescent glass to define the dimensionless shear rate $\dot{\gamma}^* = \dot{\gamma}\tau$; the applied shear rates then correspond to $\dot{\gamma}^*$ between 0.3 and 4.5, smaller and larger than one. While this is a natural choice in the context of this thesis, we note that this normalized shear rate is significantly lower than in previous studies of colloidal flows [74, 83]. Some more experimental details of image acquisition and particle tracking are discussed in chapter 2.

The shear-rate dependent flow behavior is summarized in Fig. 6.1. At shear rates $\dot{\gamma}^* < 1$, the glass flows homogeneously as shown by the particle displacements as a function of height in Fig. 6.1(a). At $\dot{\gamma}^* > 1$, the glass separates spontaneously into bands that flow at different rates as shown for $\dot{\gamma}^* = 2$ in Fig. 6.1(b). Linear

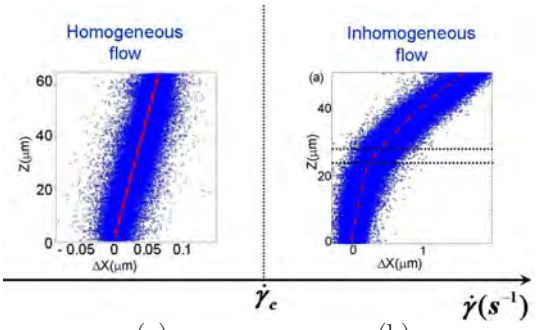

FIGURE 6.1: Deformation map of colloidal glasses at volume fraction $\phi = 0.60$. The flow is homogeneous at low shear rates (a), and inhomogeneous beyond the critical shear rate $\dot{\gamma}_c \sim 6\times10^{-5}s^{-1}$ (b). The figures show height-dependent particle displacements at shear rates $\dot{\gamma} = 3\times10^{-5}s^{-1}$ (a) and $\dot{\gamma} = 1\times10^{-4}s^{-1}$ (b). Each cross represents a particle. The Dashed horizontal lines (b) delineate the shear bands.

fits to the displacement profiles yield flow rates of $\dot{\gamma}_{\text{high}} = 2.2 \times 10^{-4}s^{-1}$ and $\dot{\gamma}_{\text{low}} = 4 \times 10^{-5}s^{-1}$ that differ by a factor of 5. We specifically checked for steady-state in our measurements as reaching steady-state may require some larger amount of strain, especially for the shear banded case. To do so, we first confirm that, after an initial transient, the slopes in Fig. 6.1(b) remain unchanged over the entire observation time. We thus observe the spontaneous transition from steady-state homogeneous to steady-state inhomogeneous flow at $\dot{\gamma}^* \sim 1$. This is in agreement with recent rheology and x-ray scattering measurements [76], revealing shear banding starting at $\dot{\gamma} \sim \tau^{-1}$.

6.3 Particle diffusion

We use the full trajectories of the particles to investigate their dynamic evolution as a function of the applied shear. For each particle i with trajectory $\mathbf{\Delta r_i}(t)$, we subtract the mean flow to compute displacement fluctuations $\mathbf{\Delta r'_i}(t) = \mathbf{\Delta r_i}(t) - \langle \mathbf{\Delta r}(t) \rangle_z$, where $\langle \mathbf{\Delta r}(t) \rangle_z$ is the average particle displacement at height z. Typical examples of the resulting mean-square displacements $\langle \mathbf{\Delta r'}^2(t) \rangle$ in the high and low shear band are shown in Fig. 6.2 (inset). The low shear band (filled circles) reveals reminiscence of a plateau, while the high shear band (open circles) exhibits a closely linear increase of $\langle \mathbf{\Delta r'}^2(t) \rangle$ similar to the mean-square displacement of particles in a liquid. This interpretation is supported by the strain correlations:

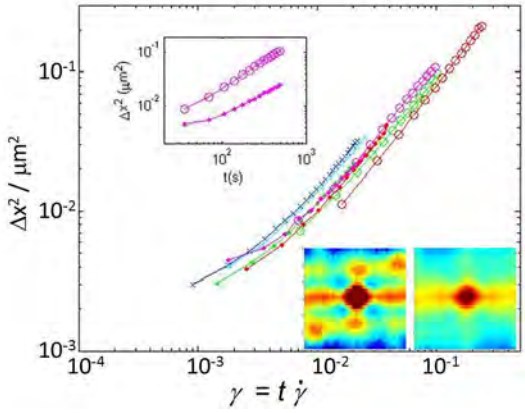

FIGURE 6.2: Mean square displacements of the particles. Upper left inset: mean square displacement in the upper (circles) and lower shear band (dots) at $\dot{\gamma}^* = 2$. Main panel: mean-square displacements as a function of rescaled time for the applied shear rates $\dot{\gamma}^* = 0.3$ (blue), 0.6 (cyan), 1.2 (green), 2 (magenta) and 5.6 (red). Lower right inset: strain correlations of low shear band for $t = 70\ s$ (left) and 350 s (right).

strain correlations computed separately for the two bands reveal coexistence of an isotropic liquid-like and an anisotropic solid-like response [81]; similar behavior is observed for all other applied shear rates with $\dot{\gamma}^* > 1$. Interestingly, we can collapse all mean-square displacements by re-scaling the time axis by $\dot{\gamma}$ as shown in Fig. 6.2, main panel. The figure compiles measurements both in the homogeneous and shear banding regime. This collapse suggests that the diffusion time scale couples directly to the local shear rate and that different dynamics of the bands is solely due to different underlying diffusion time scales. This is supported by the strain correlation function that indicates disappearance of the solid-like quadrupolar symmetry when correlations are computed on the rescaled time scale (longer by a factor of $\dot{\gamma}_{\mathrm{high}}/\dot{\gamma}_{\mathrm{low}}$), as illustrated in Fig. 6.2 (lower right insets). We thus conclude that the change of diffusion time scale causes the symmetry change of correlations.

6.4 Dynamic order parameter

To characterize the dynamics of the bands further, we search for an order parameter that is a good measure of the dynamic evolution. An appropriate measure

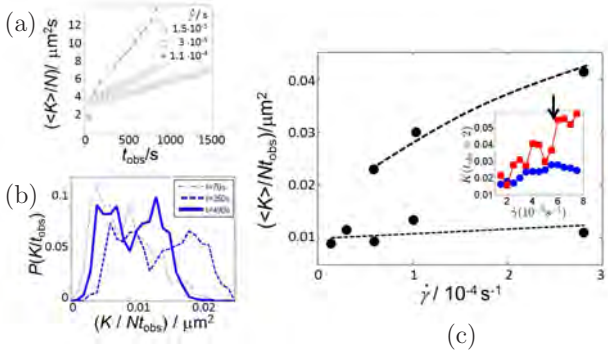

FIGURE 6.3: Dynamic order parameter and phase diagram. (a) Dynamic order parameter as a function of observation time. K is a linear measure of the system's dynamic evolution. (b) Histogram of order parameter values for increasing observation times. The emerging bimodal distribution indicates dynamic phase coexistence. (c) Corresponding dynamic phase diagram: Mean order parameter as a function of applied strain rate. The dashed lines serve as a guide to the eye. Inset shows the dynamic order parameter at continuously increasing applied shear rate, for particles in the upper (red squares) and lower region (blue dots). The arrow demarcates a sudden change of the order parameter.

of the underlying dynamic evolution is [82]

$$K = \Delta t \sum_{i=1}^{N} \sum_{t=0}^{t_{obs}} |\mathbf{\Delta r'_i}(t + \Delta t) - \mathbf{\Delta r'_i}(t)|^2, \tag{6.1}$$

the time-integrated mean-square displacement, where Δt is a short microscopic time scale. This parameter increases linearly with observation time t_{obs} (Fig. 6.3(a)); hence, K/t_{obs} measures the rate of the system's dynamic evolution, and we choose this as the dynamic order parameter. To address the transition, we determine values of K/t_{obs} in 2 μm thick horizontal subsections, and plot probability distributions for three different observation times in Fig. 6.3(b). With increasing observation time, two peaks appear and sharpen, demonstrating the coexistence of two dynamic states. The positions of the peaks demarcate the order parameter values of the coexisting shear bands. We can now construct the corresponding dynamic phase diagram from the peak positions of K for all steady-state shear rates, as shown in Fig. 6.3(c). At $\dot{\gamma}^* < 1$, only one single peak of K exists, indicating the homogeneous regime. At $\dot{\gamma}^* > 1$, two values coexist, indicating the coexisting shear bands. Similar dynamic phase coexistence is observed in

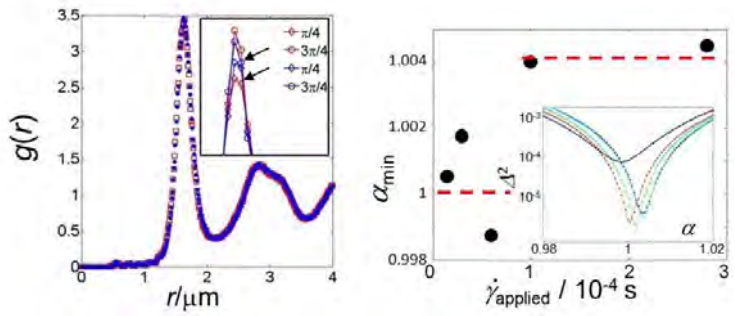

(a) (b)

FIGURE 6.4: Glass structure and density. (a) Pair correlation function of particles in the low (blue dots) and high shear band (red squares). Inset: Angle resolved $g(r)$ along the shear-shear gradient plane, extension ($\pi/4$, diamonds) and compression direction ($3\pi/4$, circles), for the low (blue) and high shear band (red). Arrows indicate decrease of $g(r)$ in the extension direction. (b) Dilation parameter, α_{min}, versus shear rate determined from the minimum of the mean-square difference of $g(r)$ (inset). Dashed lines are guides to the eye.

traffic and transport models, as described in the previous two chapters. In particular, the diagram of the order parameter for driven glasses, discussed here, has a topology reminiscent of the order parameter M diagram for the traffic flow model shown in Fig. 4.4. In the traffic flow model, cars are "driven" naturally by the protocol to acquire maximum speed.

To elucidate the sharpness as a function of the increasing shear field, we continuously ramped the shear rate $\dot{\gamma}^*$ from below to above 1, crossing the transition with a continuously increasing shear rate. The resulting values of K as a function of strain rate (Fig. 6.3(c), inset) suggest that indeed, the transition occurs rapidly, in agreement with recent x-ray measurements [84]. Because of the limited system size both spatially and along the time dimension, there are significant fluctuations; nevertheless, the data indicates a sudden jump of the order parameter at $\dot{\gamma}^* \sim 1$. The position of this jump is consistent with the steady-state measurements (main panel).

6.5 Structure of the shear bands

While the transition occurs in the dynamics, it is interesting to elucidate changes in the glass structure. Constitutive models of the flow of complex materials

suggest a coupling between flow and structure, often related to small density changes [71, 74, 85]; we therefore investigated structural differences in the two bands. We show radial distribution functions in Fig. 6.4(a). No obvious structural difference between the low and high shear band is observed, in agreement with earlier observations [74]. However, when we resolve $g(r)$ along the compression and dilation directions, a clear structural difference shows up (Fig. 6.4(a), inset). The high shear band (red symbols and line) exhibits pronounced anisotropy, while the low shear band (blue symbols and line) is more isotropic. These results reveal the structural origin of the different mechanical behavior of the two bands. This structural distortion should play an important role in the coupling of structure and dynamics in the shear banding transition. Indeed, we can measure the resulting net dilation in the shear band from the mean-square difference Δ^2 between the two angle-averaged $g(r)$ curves, as a function of a linear stretching α that transforms r to $r' = r \times \alpha$. We show Δ^2 as a function of α in Fig. 6.4(b), inset; the minima of Δ^2 at $\alpha > 1$ indicate a small amount of dilation. We evaluate the minima α_{min} for all shear rates and plot α_{min} as a function of shear rate in the main panel. These values indicate a dilation of $\sim 0.4\%$ in the high-shear band after shear banding. While the detected changes are small and affected by large uncertainty, they demonstrate a characteristic structural change accompanying the shear banding transition.

6.6 Conclusions

The direct observation of particle dynamics during shear banding of a colloidal glass reveals the coexistence of two dynamic steady-states, analogous to the coexistence of fast and slow particles in transport models, discussed in the previous chapters. The applied shear plays the role of a driving force: sufficiently high values of the applied shear rate cause coexistence of two dynamic states with different time scales for diffusion. The critical shear rate at which two dynamic bands start to coexist is the inverse relaxation time of glass. The dynamic phases differ slightly in their structure, as revealed by a careful comparison of the time averaged pair-correlation function. We believe that the presented dynamic transition should be a general feature of dynamically driven systems, as the similarity with the driven transport systems discussed in the previous two chapters suggests.

7

From collective transport behavior to the stepping dynamics of individual molecular motors

In this chapter, we study crowding effects in the motion of molecular motors along biopolymer networks. We focus on experimental observation and analysis of the motion of three motor proteins, Kinesin-1, Kinesin-II and OSM-3, along microtubule networks. We develop a new technique, based on correlations of intensities, to efficiently and accurately extract the motile properties from microscopy data. This technique has the advantage over single particle tracking that it is much faster and can achieve accurate measurements of dynamic properties, even at high densities. With the new method we find that crowding effects start to occur at low densities for Kinesin-1, while OSM-3 and Kinesin-II can function at much higher densities. The most important crowding effect seems to be a reduction of the run length, while the velocity changes only slightly with density.

7.1 Introduction

Efficient transport of nutrition and waste is of vital importance to all living organisms. For large molecules and vesicles, this task is carried out by molecular motors that move along the cytoskeleton and carry cargo. The diffusive motion of such large particles would be too slow for efficient transport, particularly in the crowded cell environment. Cells are crowded with proteins, lipids and other sorts of macromolecules [86]. Hence, molecular motors are needed to guarantee efficient transport, but even for them, crowding effects may strongly affect their motion and transport efficiency.

These molecular motors transport cargo along a network of line-like pathways, similar to the macroscopic transport by vehicular traffic, studied in chapter 4 and 5. However, while real traffic is reasonably well described by hard-core interactions, not much is known about the interactions of molecular motors. Nevertheless, models like TASEP, based on hard-core interactions, are commonly used to study the collective transport properties of molecular motors [11, 87]. We will follow this approach in the next chapter, where we use TASEP to study the collective dynamics of molecular motors on a network. In this chapter, we focus on the experimental observation of molecular motor motion. We study their crowding and interactions using TIRF microscopy to image their motion on a biopolymer network *in vitro*.

A general problem in cell biology is that *in vitro* experiments typically study idealized, uncrowded situations, while the crowded environments of cells might have a major effect on the functional properties of macromolecules [86]. The study of molecular motors moving along the cytoskeleton is not much different in that respect. The cytoskeleton is crowded with multiple types of molecular motors and other specific proteins. However, *in vitro* experiments typically study motile properties of motors at low particle densities [86]. The low densities allow for control of single particles with optical tweezers [88] or particle tracking in microscopy data [89]. Crowding effects may, however, have a major effect on transport in the real cell environment. These effects seem hence central in the understanding of transport in living cells.

In this chapter we present a new approach, based on correlations of intensities, to analyze microscopy data of molecular motors at high densities. By analyzing intensity fluctuations over space and time, the average velocity and run length are determined at once for all motors moving over a microtubule. Simultaneously, we calculate the average motor density on the microtubule using fluorescence correlation spectroscopy. We apply these techniques to the motor proteins Kinesin-1, Kinesin-II and OSM-3. We find that crowding effects start to occur at strikingly different densities for these motors. Already at low densities, when the motors are well separated, the run length of Kinesin-1 seems to decrease. Kinesin-II and OSM-3 on the other hand are able to function at much higher densities. These findings indicate a long interaction length between Kinesin-1 motors and relatively short interaction lengths between OSM-3 motors or Kinesin-II motors. The response of these motor proteins to crowding conditions seems to be detachment from the microtubule network, resulting in a reduced run length at high densities, while the velocity is only weakly dependent on density.

7.2 Experiments

A detailed description of the experimental techniques is given in chapter 2. Here, we briefly discuss the most important features of the experiments on molecular motors. We construct a stepping-assay of dynamically stabilized microtubules attached to a glass plate in a microfluidic channel. After the preparation, a solution containing molecular motors and ATP is flowed into the microfluidic channel. The motors bind to the microtubules and perform stepwise movement along the microtubules by consuming ATP [16].

We use Totally Internal Reflection Fluorescence (TIRF) microscopy to detect the motion of the molecular motors along the microtubules. The motors are labeled with a fluorophore that emits visible light after excitation with a laser. The TIRF laser excites only motors with fluorescent labels which are close to the glass/solution interface. TIRF microscopy hence creates high-quality 2D images of molecular motors that move along the microctubules attached to the glass, with minor background noise from the motors in the bulk of the solution. A reconstruction of the micrtotubule network from the time averaged fluorescent signal of molecular motors is shown in the left panel of Fig. 7.1.

To work with very high motor densities, we fluorescently label only a fraction of the motors [90, 91]. The unlabeled motors have identical properties, but are invisible. This prevents a saturated homogeneous fluorescent intensity on the microtubule from nearby motors, and thus makes it possible to study the motion of molecular motors even at high densities.

7.3 Correlation of intensities

Traditionally, molecular motor motion from TIRF microscopy data has been analyzed by single particle tracking [89]. Particle tracking is time consuming and requires spatially well separated fluorescent signals in order to distinguish individual particles clearly. Instead of pursuing this route, we analyze the complete fluorescent intensity signal using correlation techniques on the image intensities. By calculating intensity correlations in space and time, we obtain averaged dynamic motor properties, such as motor velocity and run length along microtubules.

The first step of this technique is to divide a microtubule into small slices, see the enlarged section in Fig. 7.1. Due to the motion of molecular motors, the intensity varies spatially and temporally. This is shown in Fig. 7.2, where we plot the intensity as a function of both space and time. The left panel shows low, and the right panel high motor density.

In the former, only a few particles move along the microtubule segment during the observation time. This is the typical density at which particle tracking is done;

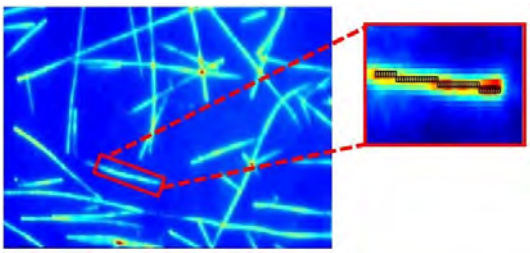

FIGURE 7.1: The 2D microtubule network measured with TIRF microscopy. The image is obtained by time-averaging the fluorescent signal from motors. Their averaged trajectories highlight the microtubule network. The enlarged section shows the division into slices of one microtubule.

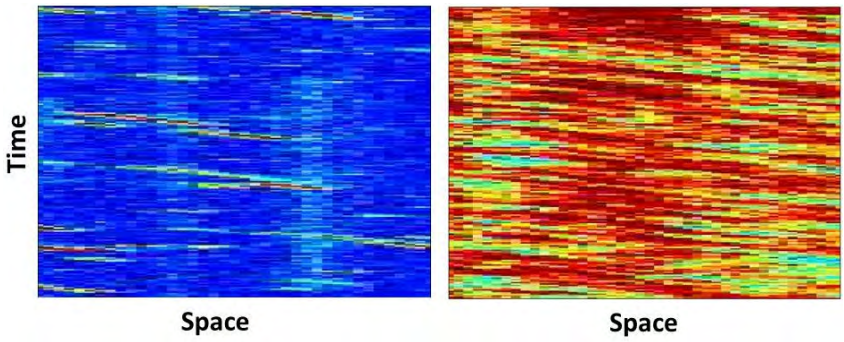

FIGURE 7.2: Space time diagrams of the fluorescent intensity along the microtubule. The color indicates the intensity level, with blue low intensity and red high intensity. Left panel: Experiment with low motor density. Right panel: Experiment with high motor density. The average velocity and run length can be determined by correlating intensity fluctuations between these extreme values of the density. Optimal performance is expected at intermediate values of the density.

particles are relatively well distinguishable. In particle tracking the information contained in Fig. 7.2(a) is basically binarized: an intensity spot at each time corresponds to a particle or not.

With the technique of intensity correlations introduced here, the full intensity profile is used. If a particle is at position x at time t, the intensity $I(x,t)$ is higher than the average intensity $\langle I(x,t)\rangle$. Some time later the particle has moved away and the intensity at x will be lower. Now the intensity at the new location of the motor will be higher. We can learn about the particle dynamics by correlating intensity fluctuations over time and space. We compute correlations of fluctuations as a function of spatial separation dx and temporal separation dt:

$$\text{Correlation}(dx,dt) = \frac{\Big\langle \big(I(x,t) - \langle I(x,t)\rangle\big)\big(I(x+dx,t+dt) - \langle I(x+dx,t+dt)\rangle\big)\Big\rangle}{\sigma\big(I(x,t)\big)\sigma\big(I(x+dx,t+dt)\big)}, \tag{7.1}$$

with,

$$\sigma\big(I(x,t)\big) = \sqrt{\Big\langle \big(I(x,t) - \langle I(x,t)\rangle\big)^2\Big\rangle}, \tag{7.2}$$

being the standard deviation of the intensity distribution, used to normalize the intensity fluctuations. The averages in Eq. 7.1, denoted by the triangular brackets, are taken over both space and time.

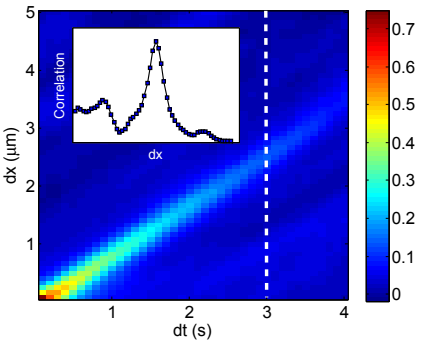

FIGURE 7.3: Correlation of intensities along a microtubule as a function of temporal separation and spatial separation. The color indicates the amount of correlation, with at the extremes red for strong positive correlation and blue for no correlation. The inset shows the cross section along the dashed line.

The correlation of intensities of an ensemble of Kinesin-1 motors moving along a microtubule is shown in Fig. 7.3. The line of positive correlation running through the origin dominates the correlation signal. This signal results from the autocorrelation of particles. The autocorrelation is large at the origin and decreases with time. Nevertheless, the autocorrelation dominates the signal also at large times, see the inset of Fig. 7.3. We will evaluate the temporal evolution of the autocorrelation in the next section to calculate the average velocity and run length of motors. This technique works well over a wide range of densities: from the low density of the left panel of Fig. 7.2 up to the high density of the right panel of Fig. 7.2. Optimal performance, however, is at intermediate densities, where the intensity fluctuations are the largest.

7.4 Motor dynamics from autocorrelation

To extract the average motor velocity and run length from the intensity correlation, we fit the autocorrelation peak with a Gaussian function for each value of dx, see Fig. 7.4(a). The autocorrelation of continuous moving point-like particles would be a delta-peaked function of positive correlation centered at the exact passage time of the particle dt. The point-like fluorescently labeled motors, however, emit a diffraction limited pattern, of which the inner ring can be approximated by a Gaussian. This gives rise to the shape of the autocorrelation peak with finite width.

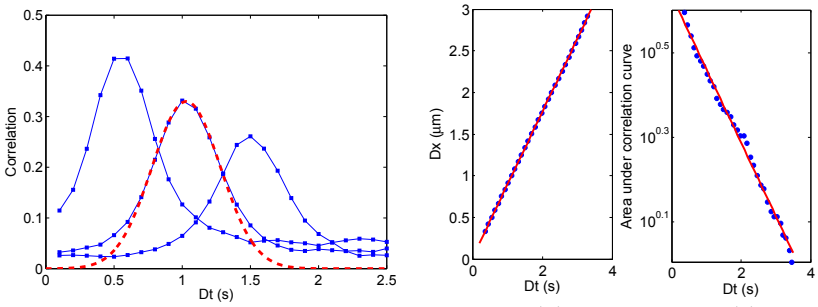

FIGURE 7.4: (a) Correlation of intensities as a function of the time separation. The blue lines and dots correspond to experimental data from different spatial separation dx. The dashed red line is a Gaussian fit to the autocorrelation peak of one of the curves. (b) Spatial separation dx versus the average dt value of the autocorrelation peak. The dt values are extracted from the Gaussian fits. The slope of the linear fit gives the average motor velocity. (c) Area under the Gaussian fit versus the average dt value of the Gaussian. The exponent of the exponential fit is the average time a motor is attached to the microtubule.

We find the average time interval dt required for particles to travel a distance dx from the mean position of the Gaussian fit. In Fig. 7.4(b) we plot the obtained time interval dt for all spatial separations dx.[1] The ratio of traveled distance and corresponding time interval gives the average velocity $v = dx/dt$; hence we obtain v from the slope of a linear fit through the data, as shown in Fig. 7.4(b).

Motors that detach from the microtubule no longer contribute to the autocorrelation signal. The area under the autocorrelation curve is proportional to the fraction of motors still attached. Its time evolution hence provides information on the fraction of particles that remain attached to the microtubule. The area under the autocorrelation peak is determined from the Gaussian fit. If all particles remained attached indefinitely, they would all travel a distance dx after some time interval. In this case, the total area A under the autocorrelation peak would be independent of dt and dx. We observe the detachment of particles as a decay of the autocorrelation signal as plotted in Fig. 7.4(c). If we a assume a constant probability of detachment for each step, the decay of the total autocorrelation is exponential with a characteristic time τ. The red line in Fig. 7.4(c) corresponds to a fit with the exponential function: $A = A_0 exp(-\tau dt)$. From

[1] In fact, we use only the data for which the Gaussian function can be fitted with reasonable small errors. We include data from increasing spatial separations into our analysis, until the 95 % confidence interval of the mean dt value exceeds half the time interval between two images.

this fit, we determine the characteristic time τ a motor remains attached to the microtubule. The average run length of motors along the microtubule follows immediately from τ and v:

$$\text{Run length} = \tau v\,. \tag{7.3}$$

In addition, information about the distribution of motor velocities, or the randomness in the stepping process, could be extracted from the change in the width of the autocorrelation peak. The width of the peak is, however, dominated by the width of the diffraction limited intensity pattern of each motor. Hence, we do not use the evolution of the peak width to learn about the randomness, but instead study the average velocity and run length dependence on density to elucidate the randomness in the stepping process.

7.5 Fluorescence correlation spectroscopy

To interpret the measured velocities and run lengths with regard to crowding effects, it is important to have a good measure of the motor density on the microtubule. However, this density is not a direct control parameter; it is the motor concentration in the surrounding solution that is controlled experimentally. Increasing this concentration enhances the number of motors attached to microtubules. Although there is some evidence [90], it is *a priori* not clear whether the relation between concentration and density is proportional. We use fluorescence correlation spectroscopy to directly determine the motor density on a microtubule.

In fluorescence correlation spectroscopy [92] the number of fluorescent particles in a certain volume is derived from the fluctuations of the total, volume integrated, intensity. The general idea is that a high number of motors in the volume results in small intensity fluctuation relative to the average intensity. In the present case the "volume" corresponds to the area of the microtubule. Care must be taken to subtract the background intensity, as the total intensity results from motors on the microtubule and background noise. The background signal can be measured easily in regions of the sample with no microtubules, see Fig. 7.1. For each pixel on the microtubule we subtract the average background intensity,

such that the total fluorescent intensity I_T of the microtubule originates from fluorescently labeled motors attached to the microtubule only.

The total intensity varies over time, because motors attach and detach from the microtubule. We assume that the attachment of motors to the microtubule is a random process.[2] In that case, the number of attached motors is Poisson distributed, and the normalized variance:

$$\frac{\sigma^2(I_T)}{\langle I_T \rangle^2} = \frac{\sigma^2(N)}{\langle N \rangle^2} = \frac{1}{\langle N \rangle}\,, \tag{7.4}$$

where in the first step we used $I_T \propto N$ and in the second step $\sigma(N) \propto \sqrt{N}$ for Poisson distributed N. From the average number of motors on the microtubule we can calculate the density $\rho = N/L$, where L is the length of the microtubule. The idea to use fluctuations in the study of molecular motors is not new. However, so far observations of high density fluorescent motors was not possible, and studies were focused on fluctuations in the dynamics of single particles [93, 94].

7.6 Results

7.6.1 Density

We study the onset of crowding effects, by measuring the density ρ of motors on a microtubule as a function of motor concentration c in the solution. The density of fluorescently labeled motors on a microtubule is measured with fluorescence correlation spectroscopy, as explained in the previous paragraph. We are able to reach high densities by fluorescently labeling only a fraction of motors. The motors only differ in the fluorescent labels, otherwise they have identical properties. In these experiments the number of labeled motors is kept constant. To reach high densities, we add increasing amounts of unlabeled motors, raising the dilution factor of labeled motors. In Fig. 7.5 we show the results for OSM-3 with a constant concentration of 40 nM labeled motors. Our fluorescence correlation measurements show that the average density of labeled OSM-3 motors on the microtubules remains constant at about 1.5 per micrometer up to a dilution factor

[2] Further, we assume that the fluorophore has identical properties that do not change with time.

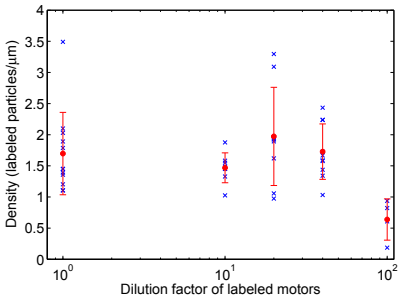

FIGURE 7.5: Density of fluorescently labeled motors on the microtubule versus motor concentration in the solution. The density is obtained with fluorescence correlation spectroscopy analysis of the intensity on the microtuble.

of 40. At this dilution, the total OSM-3 concentration in the solution is 40x40 $nM = 1600\ nM$ and the total density of OSM-3 on the microtubule is 40x1.5= 60 motors per micrometer. However, at the highest dilution, the observed density of labeled motors is significantly lower: 0.6 motors per micrometer, as shown in Fig. 7.5.

We interpret this result with crowding induced detachment of, or lack of space for, molecular motors. The idea is that when the microtubule fills up with motors, the available space for new motors to bind reduces (lower attachment rate) and/or the interactions between motors increase resulting in shorter run times (higher detachment rate). These crowding effects result in a density decrease of labeled motors on the microtubule, observed for the highest dilution with unlabeled motors in Fig. 7.5.

Interestingly, crowding effects occur at a density of 60 OSM-3 motors per micrometer. OSM-3 motors take steps of 8 nm and need twice this space to progress in their head-over-head stepping process. For 60 motors per micrometer all space is taken up since 60x2x8 $nm \approx 1\mu m$, thus the microtubule consists of one sequence of motors. In other words, around a density of 60 motors per micrometer the available space for moving motors saturates.

We note that depending on the microtubule, the measured motor density can vary strongly for a given dilution. This could arise from different attachment and detachment properties of the microtubule, fluctuations in the local concentration caused by the nearby presence of other microtubules or from a drift in the intensity due to experimental issues, resulting in an underestimate of the density.

7.6.2 Kinesin-1

Here we report the velocity and run length of the microtubule specific motor Kinesin-1 as a function of density for two buffers with a different salt concentration, PEM12 and PEM80. Density, velocity and run length are measured from correlations of the fluorescent intensities, as described above. In Fig. 7.6 we plot the run length and the velocity versus density for the two buffers.

We first focus on the measurements with low salt concentration (PEM12 buffer). Blue crosses indicate a measurement from a single microtubule in low salt concentration, and red dots are corresponding averages over a number of microtubules. The error-bars are given by the standard deviation. Over the observed density range in Fig. 7.6(a), the velocity is largely constant, around 0.8 $\mu m/s$. We observe a small decrease of velocity with increasing particle density. At the same time, the data shown in Fig. 7.6(b) suggests that the run length is about 1.2 μm and does not change over this density range.

We repeated these experiments with a high salt concentration (PEM80 buffer) and indicate the resulting velocity and run length with green symbols and error bars in Fig. 7.6(a) and (b). Clearly, velocities similar to the measurements in low salt concentration are observed. On the other hand, the run length is much reduced: the data in Fig. 7.6(b) shows that the run length is 0.7 μm for measurements with PEM80; much smaller than the run length of 1.2 μm observed for measurements with the low salt concentration buffer PEM12. In a PEM80 buffer, the run length of Kinesin-1 decreases with density. We conclude that the run length decreases due to crowding effects. The data in Fig. 7.6(b) suggests that crowding starts to occur at remarkably low densities: around 3 motors per micrometer. At this density the average distance between motors is about 300 nm, much larger than the step size of a motor 8 nm. Long-range interactions between Kinesin-1 motors have been reported before, but seemed to suggest an attractive interaction [95], in contrast to the repulsive interaction observed here.

The interaction range between Kinesin-1 motors is apparently long-ranged, while its origin remains elusive. By comparing the Kinesin-1 data using different buffers, we can elucidate the effect of salt in the surrounding solution on the motor dynamics. We observe similar velocities for both buffers, suggesting that the salt concentration does not influence the binding of ATP; a lower binding rate

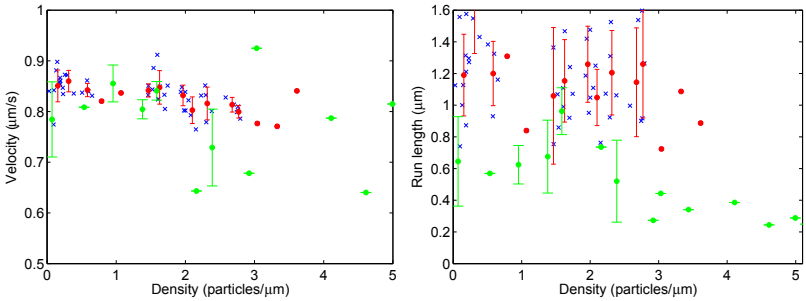

(a) (b)

FIGURE 7.6: Dynamical properties of Kinesin-1 as a function of motor density. Each blue cross correspond to a measurement of one microtubule in a PEM12 buffer. The red dots are corresponding averages over a density range of linear size. The error-bars are given by the standard deviation. The green dots and error-bars show the averaged data over multiple microtubules in a PEM80 buffer. (a) The average motor velocity. (b) The average run length of motors along the microtubule before detaching.

of ATP would result in a lower velocity. The run length is significantly increased when a low salt concentration (PEM12 buffer) is used compared to the high salt concentration in the PEM80 buffer. This could be because salt makes each head of the motor less tightly bound to the microtubule or because salt screens the microtubule from a motor-head while stepping. Both scenarios make the motor more prone to random collisions with the surrounding fluid molecules, resulting in a higher detachment rate and shorter run lengths.

7.6.3 OSM-3

We also studied the dynamic properties of OSM-3 as function of density. The experiments on OSM-3 are all performed in a relatively high salt concentration with buffer PEM80. We reached very high densities in TIRF microscopy by labeling a fraction of the motors only. We have argued above that increasing the motor concentration in the solution results in a proportional increase of the motor density on a microtubule, up to a total density of 60 motors per micrometer. At this density the available space on the microtubule becomes limited. Here we discuss the dependence of velocity and run length on density and finally arrive at a model to describe the stepping process of OSM-3.

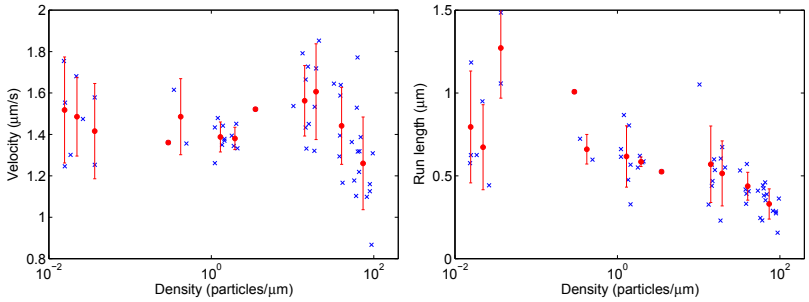

(a) (b)

FIGURE 7.7: Dynamical properties of OSM-3 as a function of motor density. Each blue cross corresponds to a measurement of one microtubule. The red dots are averages over a density range of logarithmic size. The error-bars are given by the standard deviation. (a) The average motor velocity. (b) The average run length of motors along the microtubule before detaching.

The velocity of OSM-3 as a function of motor density is shown in Fig. 7.7(a). The velocity barely changes over several decades of motor density. Only at the highest density, where the microtubule becomes saturated with motors, the velocity drops by about 20 percent. The run length, on the other hand, decreases significantly with increasing motor density. At low densities the run length is about 0.7 μm, while it decreases gradually down to 0.3 μm with 100 motors per micrometer, see Fig. 7.7(b).

Based on the observations of constant velocity and decreasing run length up to saturating motor density, we propose the following model to describe the stepping process of OSM-3. The presence of another close-by motor does not prevent OSM-3 from stepping. If an OSM-3 motor runs into another OSM-3 motor, it detaches from the microtubule. This explains the reduced run length at high densities. OSM-3 does not pause the stepping process due to interactions with another motor; pausing would reduce the average velocity, while we observe a fairly constant velocity, but decreasing run length.

Careful inspection of Fig. 7.7(a) shows that the average velocity first slightly goes up before a minor decrease at the highest densities. Although both effects are subtle and perhaps not significant, we speculate on their origin as follows. The slight reduction of the average velocity at high densities might result from a change in the distribution of velocities. Motors that move faster run into slower motors and unbind from the microtubule due to the interaction. This

biases the average velocity towards lower velocities. The small increase in the average velocity, before its decline, could arise from reinforced stepping rates of motors due to local coupling between motors. The possible coupling could be of hydrodynamic nature [96], mediated through the surrounding solution, or of electrostatic nature, mediated through the microtubule.

7.6.4 Kinesin-II

In addition to the motors Kinesin-1 and OSM-3, we studied the run length and velocity of the motor Kinesin-II as a function of density. To reach high densities in the experiments we label only a fraction of the Kinesin-II motors with a fluorophore. We use the low salt concentration buffer PEM12.

In Fig. 7.8(a) we show the velocity of Kinesin-II as a function of density. The Kinesin-II velocity of around 0.3 $\mu m/s$ is considerably lower than the velocity 1.2 $\mu m/s$ of OSM-3, but the qualitative behavior with increasing density is remarkably similar. For both motors the velocity reaches a maximum around a density of 10 motors per micrometer. At this point the average distance between motors is about 100 nm. Increasing the density beyond this maximum results in a decrease of the velocity for both motor types.

The run length of Kinesin-II, shown in Fig. 7.8(b), seems to have a maximum at the intermediate density of around 10 motors per micrometer, just like the velocity. At low density the run length is around 1.5 μm, it reaches values above 2 μm at intermediate densities and decreases gradually to around 0.4 μm at the highest measured density of around 300 motors per micrometer. Note that this crowding density of Kinesin-II is slightly higher than that of OSM-3, but significantly higher than that of Kinesin-1. The maximum in run length at intermediate densities seems to be unique for Kinesin-II; it is not observed for the other motors studied and should be confirmed by additional experiments. Moreover, we expect much lower run length when a high salt concentration buffer is used in the experiments.

Besides the observed maximum in run length, the behavior of Kinesin-II is very similar to that of OSM-3. Therefore, we assume that the interactions between motors and the stepping behavior of Kinesin-II is similar to that described for OSM-3 in the previous section. Interestingly, Kinesin-II and OSM-3 are known

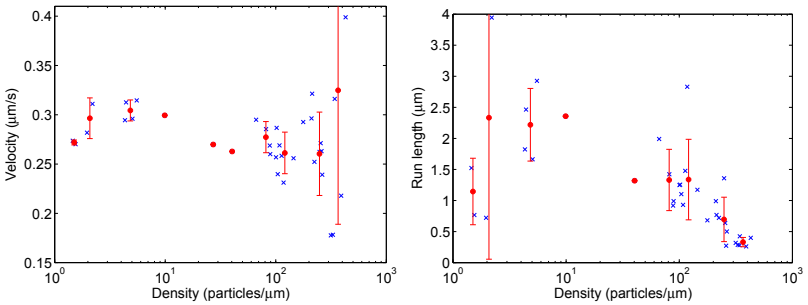

(a) (b)

FIGURE 7.8: Dynamical properties of Kinesin-II as a function of motor density. Each blue cross corresponds to a measurement of one microtubule. The red dots are averages over a density range of logarithmic size. The error-bars are given by the standard deviation. (a) The average motor velocity. (b) The average run length of motors along the microtubule before detaching.

to work together in intracellular transport of cilia [97]. Therefore, the compatible stepping mechanisms and interactions of the motors, observed here through the velocity and run length, could be beneficial for efficient transport.

7.7 Conclusions

In this chapter we reported measurements of the velocity, run length and density of molecular motors on microtubules, based on a new correlation method of fluorescent intensities. With this method, we analyzed microscopy data per microtubule, instead of tracking individual motors. This provides faster and more accurate results on the average velocity and run length, as well as information on the particle density on the microtubule.

We apply the new technique to study the velocity and run length of Kinesin-1, Kinesin-II and OSM-3, and demonstrate that crowding occurs at strikingly different densities for these motors. Under crowding conditions it is mostly the run length of the motors that significantly reduces; the velocity is less affected by density changes.

Crowding effects start to occur at remarkably low densities for Kinesin-1: already when the average distance between motors is around 300 nanometers, motors start to interact, resulting in a lower run length. To the best of our knowledge,

such long range interactions with a repulsive character have not been reported before; the nature of the interaction is therefore unclear.

For Kinesin-II and OSM-3 crowding effects occur when there are around 100 motors per micrometer: much higher motor densities than for Kinesin-1. These findings indicate the range at which the different types of motors can efficiently work and transport cargo in the presence of other motors: a Kinesin-1 motor needs much more free space to operate than OSM-3 and Kinesin-2, which keep moving along the microtubule in close-by presence of other motors. This behavior is in agreement with the way the different motor types are known to transport cargo in the cell: Kinesin-1 operates more or less alone while carrying cargo, while both Kinesin-II and OSM-3 work collectively in groups of tens of motors during cargo transportation. Interestingly, we observe an optimal density for the collectively operating motors Kinesin-II and OSM-3 at which each motor moves at maximum velocity. Kinesin-II and OSM-3 might not only tolerate the presence of other motors in their close surrounding, but perhaps even benefit from their presence.

The main response to crowding conditions of the molecular motors studied in this chapter seems to be a decrease of run length, not a reduction of their velocities. The response of particles in colloidal glasses and traffic systems to crowding, studied in the previous chapters, is actually opposite: cars tend to slow down and form traffic jams on crowded roads, while the diffusion time of colloidal particles strongly increases at high densities. This different response to crowding might be explained by the particle confinement in the two latter systems, which is not present for motors walking along microtubule networks. Motors can simply detach from the microtubules, diffuse through the cytoplasm and find another, perhaps less crowded place on the microtubule network. In contrast, cars on a crowded road cannot simply hop off, and are confined by the absence of off-ramps that could provide faster alternative roads to continue their path. If present, most drivers would probably not spent much time driving slowly in traffic jams, but continue along the fastest available road to their destination. Expanding on this analogy between traffic and molecular motor transport, we could speculate that molecular motors might hop off and find another microtubule to increase the efficiency of transport; such an interpretation would make sense from an evolutionary perspective.

8

Simulations of transport in random networks

Using the totally asymmetric simple exclusion process (TASEP) and mean-field transport theory, we investigate the transport in closed random networks with simple crossing topology - two incoming, two outgoing segments, as a model for molecular motor motion along biopolymer networks. Inspired by in vitro observations of molecular motor motion, similar to those described in the previous chapter, we model the motor behavior at the intersections by introducing different exit rates for the two outgoing segments. Our simulations of this simple network reveal surprisingly rich behavior of the transport current with respect to the global density and exit rate ratio. For asymmetric exit rates, we find a broad current plateau at intermediate motor densities resulting from the competition of two subnetwork populations. This current plateau leads to stabilization of transport currents within such networks.

8.1 Introduction

In the last chapter, we have studied the motion of molecular motors along biopolymers using microscopy. We focused on high densities to investigate effects of crowding. A popular model to describe the collective behavior of molecular motors is the Totally Asymmetric Simple Exclusion Process (TASEP) [5, 7, 28]. Due to the discrete nature of individual motors this lattice model is particularly appropriate to study molecular motor motion.

In this chapter, we use TASEP to simulate the collective motion of molecular motors on networks similar to the ones studied experimentally in the previous chapter. Recently, TASEP has been applied to transport along cytoskeleton assemblies [12, 98]. Originally formulated for one-dimensional systems, TASEP was extended to networks by defining the dynamics at crossings. Recent experimental observation of molecular motor motion along the cytoskeleton highlights the non-trivial dynamics of molecular motors at crossings: specific types of motors were found to switch between segments with specific probabilities [90, 99–101]. This preference at crossings might crucially determine the transport properties of the network. Indeed, a recent simulation of a single-crossing system highlights the heterogeneous motor density among the crossing filaments resulting from a preference in outflow directions [102, 103]. To particularly study these density heterogeneities and other crowding effects, we have assumed that the motors do not detach and stay on the network for infinite times.

Because of the characteristics of real motors to change paths at intersections in a preferred direction, we study the role of crossings with asymmetric exit rates on the transport behavior of large networks using the TASEP model. We study network structures inspired by our *in vitro* experiments (see Fig. 3.4(a)), in which typically arrays of cytoskeleton filaments are created by attachment to a surface, forming a network topology of intersecting lines in a two-dimensional plane. We show that for large networks the ratio of exit rates at crossings together with the global motor density determines the transport capacity of the network. We identify four regimes of current-density behavior: A low-density regime controlled by the relative exit probabilities and network topology, a jamming regime with heterogeneous density and resulting complex interplay of subnetwork currents,

a saturation regime and a high-density regime with local dynamics and homogeneous density. The extend of each regime and the actual value of the current is found to strongly depend on the relative exit rates at crossings. The general character of TASEP makes the simulations of driven motion on networks presented in this chapter relevant to a wider context of transport phenomena, e.g. to vehicular transport through a network of highways.

8.2 Model description

We model cytoskeleton assemblies with a two-dimensional network of intersecting segments. Inspired by *in vitro* experiments we create a network topology by projecting lines in random positions and directions on a square (Fig. 3.4(b)). We introduce periodic boundary conditions by connecting the beginning and end of every line at the boundaries of the square, thus creating a closed network. The resulting network is characterized by the number of crossings N_v, the number of segments $N_s = 2N_v$ and the density of motors ρ.

Molecular motor motion is modeled with the Totally Asymmetric Simple Exclusion Process (TASEP), in which particles perform uni-directional random sequential hops constrained by the fact that they may not overlap with each other. During a single update, a motor advances one site forward if the target site is unoccupied, otherwise no progression occurs. A detailed description of TASEP and its most important results can be found in chapter 3.

When a motor arrives at the crossing, it continues with probability γ along one outgoing segment and with probability $1-\gamma$ along the other, independent of the incoming segment. The probability γ thus defined for every crossing is a fixed property of the network. In this study, for simplicity we define equal γ for all crossings. We also neglect the possible unbinding of motors that is observed for real molecular motors [91, 99] and studied by simulations by Neri *et al.* [98]; this allows us to focus on the physical effects of jamming and flow. and obtain a simple physical picture in terms of γ. The control parameters of our simulations are thus the exit probability γ, which due to symmetry we choose as $0.5 \leq \gamma \leq 1$, and the global motor density $0 < \rho < 1$. We consider relatively large networks with $N_s \sim 500$ and uniform segment length $L = 500$. All data have been averaged

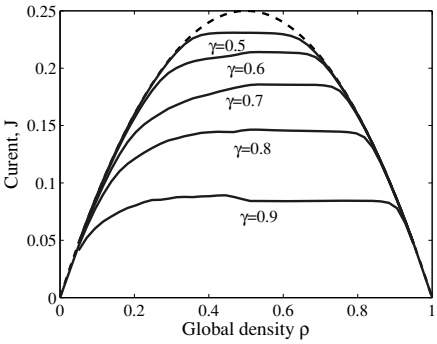

FIGURE 8.1: Transport current J dependence on global density ρ for different exit probabilities γ obtained from the TASEP simulations. For comparison, we show the current through a single segment by the dashed black line. Data is averaged over 10 000 cycles after waiting for 3000 cycles to reach steady-state.

over 10 000 cycles in steady-state, after discarding the transient (initial $\sim$ 3 000 cycles).

8.3 Results

The effect of exit probability γ on the network current is shown in Fig. 8.1, where we plot the total current versus density ρ for various values of γ (blue curves). For comparison, we also show the mean-field current through a single segment $J_s = \rho(1-\rho)$ (black dashed line) [31] that exhibits a maximum at $\rho = 0.5$ due to competition of growing density increasing the current, and density-induced jamming reducing it. The network current behaves similar to that of a single segment for symmetric exit rates ($\gamma = 0.5$, upper blue curve in Fig. 8.1): it is symmetric around $\rho \sim 0.5$, and deviates from that of the single segment only at densities around 0.5. The situation changes for asymmetric exit probability ($\gamma \neq 0.5$), where the network current becomes asymmetric and progressively reduces and flattens with increasing γ, until at $\gamma \sim 0.9$, it becomes largely independent of density. Thus, the asymmetric exit probability reduces the network current and stabilizes it at the same time.

How does this emerging current plateau arise from the interplay of currents in the network? To answer this question we investigate the distribution of individual

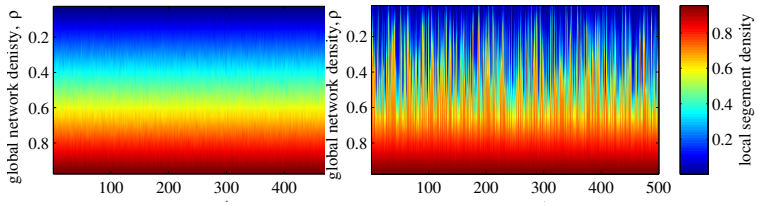

FIGURE 8.2: Local density distribution (shown by color) in segments (horizontal axis), depending on average global density ρ (vertical axis). (a) $\gamma = 0.5$, homogeneous distribution. (b) $\gamma = 0.8$, heterogeneous distribution.

segment densities ρ_s. We compare density distributions for symmetric and asymmetric exit probability in Fig. 8.2. For $\gamma = 0.5$, the density is homogeneous across the entire network: local and global densities largely coincide with only minor variation across segments (Fig. 8.2(a)). For $\gamma = 0.8$, in contrast, we find strong inhomogeneity at intermediate global density (Fig. 8.2(b)): the asymmetric exit probability leads to redistribution of paths and resulting redistribution of segment densities. Indeed, the asymmetric exit probability redistributes the motors into two subsystems: associated with the vertex exit probabilities, the network can be considered as consisting of two interconnected subnetworks, one consisting of segments with entry probability γ, and the other consisting of segments with probability $1 - \gamma$. The subnetwork with higher entry probability should populate faster, leading to the heterogeneous distribution of densities shown in Fig. 8.2(b). This is indeed confirmed in the subnetwork density distributions as shown in Fig. 8.3: at intermediate ρ, the density of the high-preferability subnetwork has grown much more, as reflected in the shift of the distribution to higher density. Due to interplay of the individual segments, the density within each subnetwork is heterogeneously distributed.

To link this density evolution to the total current, we plot average densities of the two subnetworks together with the total current in Fig. 8.4(a) and (b). Clearly, the high-preferability subnetwork takes up particles at a faster rate as shown in Fig. 8.4(b); this is a direct result of the higher entry probability. The initial slopes of the growing densities in high and low preferability subnetworks are 2γ and $2(1-\gamma)$, reflecting the two entry probabilities. When roughly half of the network sites are occupied ($\rho \sim 0.5$), high-preferability segments become saturated, and particles are increasingly taken up by the low-preferability segments. This

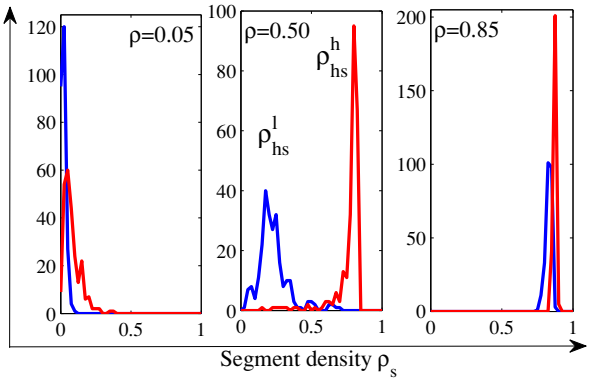

FIGURE 8.3: Histograms of density distributions for high-preferability segments (red line) and low-preferability segments (blue line) for $\gamma = 0.8$. The three panels show different global densities ρ. Large difference in the distribution occurs for the intermediate density.

interplay of the two subnetworks leads to stabilization of the total network current: as we will see below, jamming effects in the high-preferability subnetwork lead to an emerging state in the low-preferability subnetwork with rapidly changing density but constant current which ultimately leads to the current plateau as demonstrated in Fig. 8.4(a). This change of contributions is most clearly reflected in the derivatives of the densities as shown in Fig. 8.4(c). While the current is reduced, it becomes largely independent of density. At even higher density, the network becomes homogeneous and the difference between subnetworks vanishes, see Fig. 8.4(b). Hence, our approach to reduce the network into two interfering subnetworks allows us to understand the network behavior qualitatively.

We can model the network transport properties quantitatively, using basic relations for single segments, as described in chapter 3 and by Derrida *et al.* [31]. The average current through a network is given by $J = \frac{1}{N_s}\sum J_s$, with J_s the single-segment current which for a homogeneous segment with density ρ_s is $J_s = \rho_s(1-\rho_s)$. Provided segments are sufficiently long ($L >> 1$) to neglect boundary effects, the segment density ρ_s, and hence the segment current J_s, is determined solely by the incoming rate, $0 \geq \alpha \geq 1$, and outflow rate, $0 \geq \beta \geq 1$ [31], which are themselves determined by the densities at the vertices ρ_v. For the inflow rate, $\alpha = \rho_v\gamma$ or $\alpha = \rho_v(1-\gamma)$, while the outflow rate $\beta = 1-\rho_v$ is controlled solely by the availability of an empty exit vertex.

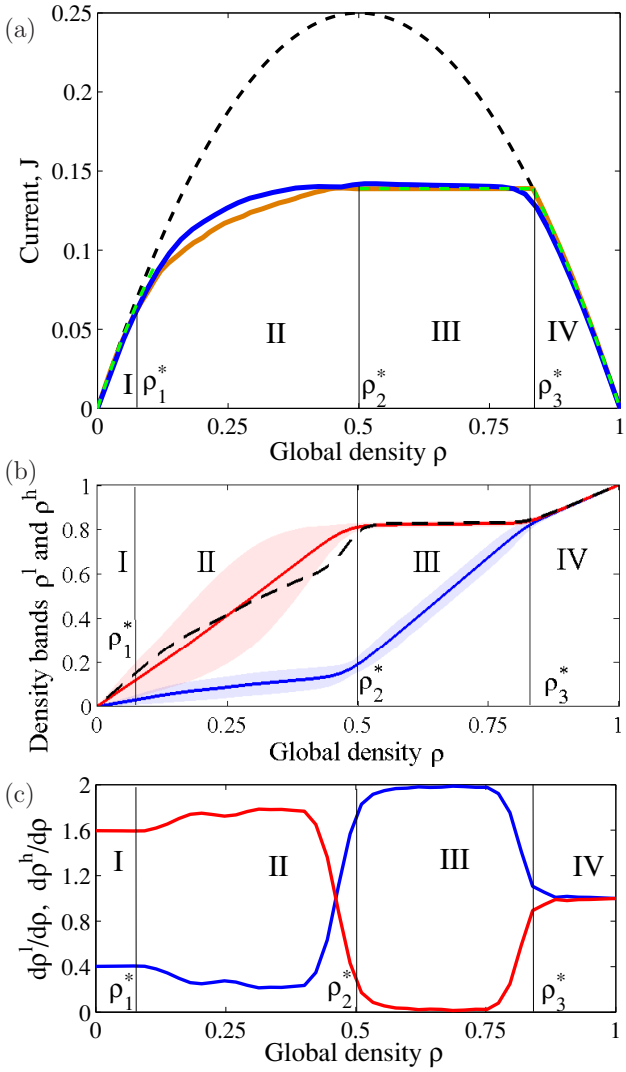

FIGURE 8.4: (a) Transport current J for $\gamma = 0.8$ calculated using TASEP model (blue curve) and iteration method (brown curve). The mean-field single segment current $J_s = \rho_s(1-\rho_s)$ is shown by the dashed black curve. Dashed green lines show approximate solutions obtained using the two subnetwork approach. (b) Dependence of mean densities in low- $\langle\rho^l\rangle$ (blue) and high-preferability $\langle\rho^h\rangle$ (red) subnetworks on the global density ρ. Shaded blue and red areas show the density distributions within the subnetworks. Dashed black curve shows the mean density of crossings $\langle\rho_v\rangle$. (c) Derivatives $\partial\langle\rho^h\rangle/\partial\rho$ (red) and $\partial\langle\rho^l\rangle/\partial\rho$ (blue) showing mean growth rates in the high- and low-preferability subnetworks. In all figures ρ_1^*, ρ_2^* and ρ_3^* indicate the transitions between different regimes.

Using these local relations for segment densities and currents, we can now compute the average steady-state current of the network. We do this by using an iterative method to converge density and current following the approach described in Neri *et al.* [12]. Segment currents J_s are controlled by the density at vertices ρ_v, while *vice versa* ρ_v depends on the currents J_s that flow through the crossings. The steady-state current and density distributions are found by iteratively computing ρ_v and J_s until the total flow into and out of each crossing is equal [12]. The resulting steady-state current (brown solid line in Fig. 8.4(a)) reproduces all features of the TASEP simulations. This close correspondence lends credence to the model, in which we apply mean-field one-dimensional TASEP theory to complex networks. We will show in the following that a further simplification to two interconnected subnetworks allows for a surprisingly good description of the network behavior. We represent the two subnetworks by their average density $\langle\rho^h\rangle$ and $\langle\rho^l\rangle$, and the corresponding subnetwork currents by J^h and J^l. This allows physical insight into the transport behavior of the network and its dependence on γ. We distinguish four regimes as a function of increasing density as discussed below.

8.3.1 Linear regime

At low density, currents in the two subnetworks are determined solely by the entry rates γ and $1-\gamma$. The average subnetwork densities grow as $\langle\rho^h\rangle = 2\gamma\rho$ and $\langle\rho^l\rangle = 2(1-\gamma)\rho$, from which we can directly compute the subnetwork currents J^h and J^l using $J_s = \rho_s(1-\rho_s)$. The resulting total current is $J = 1/2(J^h + J^l) = \rho(1-\rho) - \rho^2(1-2\gamma)^2$ (dashed green line in Fig. 8.4(a)), where the first term indicates the current for homogeneous density distribution, and the second term reflects the current reduction due to density redistribution between the two subnetworks. This term vanishes for $\gamma = 0.5$, for which the density distribution becomes homogeneous. Note that the real reduction is slightly lower than given by the term $\rho^2(1-2\gamma)^2$ due to density heterogeneities within the subnetworks.

This low-density linear regime holds up to some critical density ρ_1^*, at which the most populated high-preferability segment becomes jammed ($\alpha \geq \beta$) and the density $\langle\rho^h\rangle$ grows faster than linear as shown by the derivatives in Fig. 8.4(c). We can calculate ρ_1^* and the density distribution amongst segments in the low-density regime from the structure of the network with the help of the transition

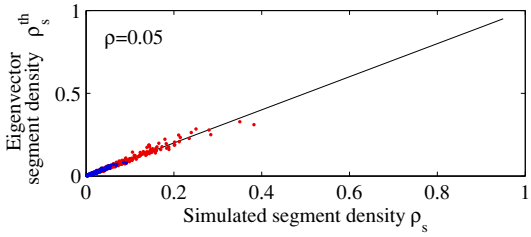

FIGURE 8.5: Comparison of segment densities obtained by TASEP simulations (horizontal axis) and transition matrix ϵ solution (vertical axis) for $\gamma = 0.8$ and $\rho = 0.05$. Every point represents the local segment density. The black identity line '$y = x$' signifies excellent agreement between TASEP simulations and transition matrix theory. Blue dots correspond to the low-preferability segments, red ones to the high-preferability.

matrix ϵ_{ij}, whose elements ϵ_{ij} denote the transition probabilities from vertex i to j. We define element $\epsilon_{ij} = 0$ when vertex j is not connected directly to vertex i through one segment, $\epsilon_{ij} = \gamma$ when j is connected to i through a high-preferability segment, and $\epsilon_{ij} = 1 - \gamma$ when j is connected to i through a low-preferability segment. This matrix specifies the transitions between vertices, giving the probability a particle continues from one vertex to the next; the eigenvector corresponding to eigenvalue 1 of matrix ϵ holds the relative distribution of densities ρ_v amongst vertices in steady-state.

Knowing the densities of all vertices we can calculate the densities of every segment ρ_s through incoming rate $\alpha = \gamma\rho'_v$ or $\alpha = (1-\gamma)\rho'_v$ and outgoing rate $\beta = 1 - \rho''_v$. At low global density $\rho \leq \rho_1^*$, the computed values of ρ_s from the transition matrix are in excellent agreement with the TASEP simulation results, as shown in Fig. 8.5. The low density regime ends when the first (high-preferability) segment becomes jammed $\alpha > \beta$. For $\gamma = 0.5$ we can find a simple analytical solution, since in this isotropic case all segments and vertices are identical. By solving $\alpha > \beta \Leftrightarrow \gamma\rho_v > 1 - \rho_v$ we get $\rho_v > 2/3$, and find the maximum global density where the linear regime is still valid $\rho_1^* = \rho_v/2 = 1/3$. For $\gamma \neq 0.5$ the network is anisotropic and the distribution of vertex densities has a finite width, so a simple analytical solution with all ρ_v equal is no longer possible. For every segment within a particular network, however, we can solve the condition $\alpha > \beta$ using matrix ϵ to find the global density ρ_1^* where jamming first occurs.

8.3.2 Jamming regime

Above ρ_1^*, jamming will spread to neighboring high-preferability segments in the direction *opposite* to the local currents, similar to jam propagation opposite to vehicle motion in traffic [50], as can be seen in Fig. 5.2(a). Since for the single segment, the transition from the unjammed ($\rho_s = \alpha$) to the jammed state ($\rho_s = 1-\beta$) is quite abrupt for $\alpha \approx \beta < 0.5$, the jam propagation is accompanied by a nonlinear growth of $\langle \rho^h \rangle$, which is compensated by a slightly stagnating growth in the low-preferability subnetwork $\langle \rho^l \rangle$, as shown by the derivatives in Fig. 8.4(c).

With the gradual propagation of jams, the density in the high-preferability subnetwork becomes increasingly heterogeneous as demonstrated by the red shaded area in Fig. 8.4(b). This heterogeneity reaches a maximum in the middle of the jamming regime and diminishes again as large fractions of high-preferability segments become jammed around one saturating density. Eventually, at the end of the jamming regime defined by $\rho = \rho_2^*$, all high-preferability segments become saturated and their density does not grow any further (see Fig. 8.4(b) and 8.4(c)).

Towards the end of the jamming regime ($\rho \to \rho_2^*$) all high-preferability segments and connected vertices are saturated with equal particle density, $\rho_s^h = \rho_v = 1-\beta$. At the same time, the low preferability segments are still unjammed. Hence, at ρ_2^*, the density difference between the two subnetworks is maximal.

8.3.3 Saturation regime

Above ρ_2^*, the density in the high-preferability subnetwork no longer increases, and further increase of ρ takes place in the low-preferability subnetwork, where consequently jams start to form. Since high- and low-preferability segments are connected by the same vertices, vertices with saturated uniform density ρ_v control the inflow ($\alpha = \rho_v(1-\gamma)$) and outflow ($\beta = 1-\rho_v$) of low-preferability segments. The only regime where the segment density ρ_s^l can rapidly change while inflow and outflow rates remain constant is during the shock phase [31], when jammed and free flow coexist within one segment and $\alpha = \beta$. Using this equality for the low-preferability segments, we obtain $\rho_v = 1/(2-\gamma)$. This allows us to calculate the saturating current of high-preferability segments: using $J^h = \beta(1-\beta)$ with

$\beta = 1 - \rho_v$, we obtain $J^h = (1-\gamma)/(2-\gamma)^2$. Since in the low-preferability segments, jam and free flow coexist, $\langle \rho^l \rangle$ changes from $\alpha = (1-\gamma)/(2-\gamma)$ to $1 - \beta = 1/(2-\gamma)$ with increasing ρ, corresponding to 1/6 and 5/6 for $\gamma = 0.8$, again in agreement with the simulations. During this rapid density change the low-preferability subnetwork current remains constant $J^l = \beta(1-\beta)$. The resulting total current is thus $J = 1/2(J^h + J^l) = (1-\gamma)/(2-\gamma)^2$ (dashed green line in Fig. 8.4(b)), independent of ρ, manifesting the current plateau.

Indeed, the TASEP simulations show plateau-like behavior with current values only slightly higher than the value $(1-\gamma)/(2-\gamma)^2$ (for $\gamma = 0.8$ in Fig. 8.4(a) the TASEP simulations plateau value is ~ 0.141 while $(1-\gamma)/(2-\gamma)^2 = 0.139$). Again this small discrepancy results from the spread in densities within the subnetworks opposed to the fixed average densities $\langle \rho^l \rangle$ and $\langle \rho^h \rangle$ assumed here.

The transition density ρ_2^* at the start of the saturation regime can be estimated from the requirement that for $\rho \geq \rho_2^*$, all high-preferability segments are jammed, i.e. $\langle \rho^h \rangle = 1 - \beta = \rho_v = 1/(2-\gamma)$. At the same point all low-preferability segments are still unjammed $\langle \rho^l \rangle = \alpha = (1-\gamma)\rho_v = (1-\gamma)/(2-\gamma)$, this leads to the mean density $\rho_2^* = (\langle \rho_s^l \rangle + \langle \rho_s^h \rangle)/2 = 0.5$ which is independent of γ.

By the end of the saturation regime at $\rho = \rho_3^*$, $\langle \rho^l \rangle$ has increased due to jamming until $\langle \rho^l \rangle = \langle \rho^h \rangle = 1/(2-\gamma)$ and the density is homogeneous throughout the whole network. This immediately gives the upper density of the saturation regime: $\rho_3^* = 1/(2-\gamma)$.

Interestingly, $\langle \rho^l \rangle$ remains much more homogeneous while rapidly increasing than $\langle \rho^h \rangle$ in the jamming regime (see blue and red shades in Fig. 8.2(b)). This difference is a direct result of the vertex densities controlling the segment densities (see black curve in Fig. 8.4(b)). During the jamming regime the crossing densities ρ_v evolve rapidly, while in saturation regime the crossing densities are saturated and fixed at $\rho_v = 1/(2-\gamma)$, thus creating density heterogeneities within segments rather than between them.

8.3.4 High density regime

For $\rho > \rho_3^*$ the density in both high- and low-preferability segments is given by the outflow rate ($\beta = 1 - \rho_v$) and becomes independent of the exit probability γ.

As a result, all segments behave identically $\rho_s^h = \rho_s^l = \rho_v = \rho$, as shown by the perfect overlap and the linear increase with slope 1 of the red and blue curves in Fig. 8.4(b). The current is then simply $J = \rho(1-\rho)$, fitting perfectly with both TASEP simulation and iteration method (see dashed green line in Fig. 8.4(a)).

8.4 Conclusions

Using TASEP simulations and mean-field theory on complex networks, we have studied the transport properties of large networks with asymmetric exit rates. We find that the transport current depends strongly on the relative exit probabilities and the global density: together they determine the transport properties and density distribution of the network. Asymmetric exit rates lead to a strong decrease of the transport current, but at the same time to the emergence of a current plateau that stabilizes the current: this plateau makes the current largely independent of variations in particle density.

The main mechanism underlying this complex network behavior is the splitting of the network into two subnetworks according to the exit probabilities γ and $1-\gamma$. This splitting into two subnetworks together with the (random) topology of the network sets the transport pathways, which, at intermediate densities, lead to heterogeneous crowding of the network. The resulting four transport regimes - linear, jamming, saturation, and high-density - are characterized by the relative densities of the two subnetworks, and the density distribution within each subnetwork. Former is determined by γ, latter by the network topology.

The topology and asymmetric exit probabilities used here mimic that of typical *in vitro* experiments in which molecular motors that walk along biopolymer networks exhibit certain preference to proceed along or switch direction at filament crossings. The work presented in this chapter hence provides insight into how local motor dynamics can result in collective transport properties of a biopolymer network. However, as seen in the experiments on molecular motors in the previous chapter, additional effects arise from the hopping-off of real motors reflected by their finite run lengths, see e.g. Fig. 7.7(b). Such detachment of motors can weaken the correlations and jamming effects we observe in the simulations, and it is currently unclear how relevant the particular network crowding effects are in

real molecular motor motion in cells. Another additional crowding effect arises from the cell background: as the cytoskeleton and the cytoplasma are crowded with different species, it remains unclear how such a diverse crowded background slows down or facilitates transport. The exclusion processes applied for modeling here, however, seems to be widely applicable in general modeling of transport and arrest phenomena; besides the molecular motors studied in the previous chapter, it also models traffic (chapter 5) and even glasses (chapter 4). Therefore, the results of this chapter may provide generic insights into traffic jams and transport capacities of highway networks and other systems with similar network based transport such as the Internet and power-grids.

Bibliography

[1] H. Jaeger and A. J. Liu, "Far-from-equilibrium physics: An overview," *ArXiv:1009.4784*, 2010.

[2] M. D. Ediger, C. A. Angell, and S. R. Nagel, "Supercooled liquids and glasses," *J. Phys. Chem.*, vol. 100, p. 13200, 1996.

[3] S. Lubeck, "Universal scaling behavior of non-equilibrium phase transtitions," *Int. J. Mod. Phys. B*, vol. 18, p. 3977, 2004.

[4] D. Chowhury, L. Santen, and A. Schadschneider, "Statistical physics of vehicular traffic and some related systems," *Phys. Rep.*, vol. 329, p. 199, 2000.

[5] A. Parmeggiani, T. Franosch, and E. Frey, "Phase coexistence in driven one-dimensional transport," *Phys. Rev. Lett.*, vol. 90, p. 086601, 2003.

[6] K. Nagel and M. Schreckenberg, "A cellular automaton model for freeway traffic," *J. Phys. I (France)*, vol. 2, p. 2221, 1992.

[7] C. T. MacDonald, J. H. Gibbs, and A. C. Pipkin, "Kinetics of biopolymerization on nucleic acid templates," *Biopolymers*, vol. 6, no. 1, pp. 1–25, 1968.

[8] D. Helbing, "Traffic and related self-driven many-particle systems," *Rev. Mod. Phys.*, vol. 73, p. 1067, 2001.

[9] S. Fielding, "Complex dynamics of shear banded flows," *Soft Matter*, vol. 3, p. 1262, 2007.

[10] P. Schall and M. Van Hecke, "Shear bands in matter with granularity," *Annu. Rev. Fluid Mech.*, vol. 42, p. 67, 2010.

[11] I. Neri, N. Kern, and A. Parmeggiani, "Exclusion processes on networks as models for cytoskeletal transport," *New Journal of Physics*, vol. 15, p. 085005, 2013.

[12] I. Neri, N. Kern, and A. Parmeggiani, "Totally asymmetric simple exclusion process on networks," *Phys. Rev. Lett.*, vol. 107, p. 068702, 2011.

[13] R. Hughes, *Colloidal Science: Principles, Methods and Applications*. Wiley-Blackwell, 2005.

[14] R. Pusey and W. van Megen, "Phase behaviour of concentrated suspensions of nearly hard colloidal spheres," *Nature*, vol. 230, 1986.

[15] R. Zargar, *Thermodynamics and Vibrational Modes of Hard Sphere Colloidal Systems*. PhD thesis, University of Amsterdam, 2014.

[16] R. D. Vale, T. S. Reese, and M. P. Sheetz, "Identification of a novel force-generating protein, kinesin, involved in microtubule-based motility," *Cell*, vol. 42, p. 39, 1985.

[17] R. D. Vale, "The molecular motor toolbox review for intracellular transport," *Cell*, vol. 112, p. 467, 2003.

[18] A. Einstein, "Über die von der molekularkinetischen Theorie der Wärme geforderte Bewegung von in ruhenden Flüssigkeiten suspendierten Teilchen," *Annalen der Physik*, vol. 322, pp. 549–560, 1905.

[19] Nobelprize.org, "The Nobel Prize in Chemistry 2014." `http://www.nobelprize.org/nobel_prizes/chemistry/laureates/2014/`, 2014.

[20] V. Chikkadi, *Spatial Correlations and Deformation Modes in Sheared Colloidal Glasses*. PhD thesis, University of Amsterdam, 2011.

[21] N. S. Claxton, T. J. Fellers, and M. W. Davidson, *Encyclopedia of Medical Devices and Instrumentation*. John Wiley and Sons, Inc., 2006.

[22] V. Prasad, D. Semwogerere, and E. R. Weeks, "Confocal microscopy of colloids," *Journal of Physics: Condensed Matter*, vol. 19, no. 11, p. 113102, 2007.

[23] J. C. Crocker and D. G. Grier, "Methods of digital video microscopy for colloidal studies," *Journal of Colloid and Interface Science*, vol. 179, no. 1, pp. 298 – 310, 1996.

[24] J. Crocker and E. Weeks, "Particle tracking using idl."

[25] Y. Rahmani, *Micromechanics and rheology of hard and soft-sphere colloidal glasses*. PhD thesis, University of Amsterdam, 2013.

[26] M. Castoldi and A. Popova, "Purification of brain tubulin through two cycles of polymerization-depolymerization in a high-molarity buffer," *Protein Expression and Purification*, vol. 32, pp. 83–88, 2003.

[27] O. Lowry, N. Rosebrough, A. Farr, and R. Randall, "Protein measurement with the folin phenol reagent," *J. Biol. Chem.*, vol. 193, 1951.

[28] C. T. MacDonald and J. H. Gibbs, "Concerning the kinetics of polypeptide synthesis on polyribosomes," *Biopolymers*, vol. 7, no. 5, pp. 707–725, 1969.

[29] V. Privman, *Nonequilibrium Statistical Mechanics in One Dimension*. Cambridge, UK: Cambridge University Press, 1997.

[30] T. M. Liggett, *Stochastic Interacting Systems: Contact, Voter and Exclusion Processes*. New York, USA: Springer, 2003.

[31] B. Derrida, E. Domany, and D. Mukamel, "An exact solution of a one-dimensional asymmetric exclusion model with open boundaries," *Journal of Statistical Physics*, vol. 69, no. 3-4, pp. 667–687, 1992.

[32] D. Chowdhury, A. Schadschneider, and K. Nishinari, "Physics of transport and traffic phenomena in biology: from molecular motors and cells to organisms," *Physics of Life Reviews*, vol. 2, no. 4, pp. 318 – 352, 2005.

[33] L. Reese, A. Melbinger, and E. Frey, "Crowding of molecular motors determines microtubule depolymerization," *Biophysical Journal*, vol. 101, no. 9, pp. 2190 – 2200, 2011.

[34] K. Nishinari, Y. Okada, A. Schadschneider, and D. Chowdhury, "Intracellular transport of single-headed molecular motors kif1a," *Phys. Rev. Lett.*, vol. 95, p. 118101, Sep 2005.

[35] T. Chou and D. Lohse, "Entropy-driven pumping in zeolites and biological channels," *Phys. Rev. Lett.*, vol. 82, pp. 3552–3555, Apr 1999.

[36] R. Barlovic, T. Huisinga, A. Schadschneider, and M. Schreckenberg, "Open boundaries in a cellular automaton model for traffic flow with metastable states," *Phys. Rev. E*, vol. 66, p. 046113, Oct 2002.

[37] D. Helbing, "Traffic and related self-driven many-particle systems," *Rev. Mod. Phys.*, vol. 73, pp. 1067–1141, Dec 2001.

[38] T. Karzig and F. von Oppen, "Signatures of critical full counting statistics in a quantum-dot chain," *Phys. Rev. B*, vol. 81, p. 045317, Jan 2010.

[39] N. Champagne, R. Vasseur, A. Montourcy, and D. Bartolo, "Traffic jams and intermittent flows in microfluidic networks," *Phys. Rev. Lett.*, vol. 105, p. 044502, Jul 2010.

[40] B. Eisenblätter, L. Santen, A. Schadschneider, and M. Schreckenberg, "Jamming transition in a cellular automaton model for traffic flow," *Phys. Rev. E*, vol. 57, p. 1309, 1998.

[41] A. Schadschneider, "Traffic flow: a statistical physics point of view," *Physica A: Statistical Mechanics and its Applications*, vol. 313, no. 1–2, pp. 153 – 187, 2002. Fundamental Problems in Statistical Physics.

[42] A. Schadschneider, "The Nagel-Schreckenberg model revisited," *Eur. Phys. J. B - Cond. Mat. and Complex Systems*, vol. 10, p. 573, 1999.

[43] M. Schreckenberg, A. Schadschneider, K. Nagel, and N. Ito, "Discrete stochastic models for traffic," *Phys. Rev. E*, vol. 51, p. 2939, 1995.

[44] F. Ritort and P. Sollich, "Glassy dynamics of kinetically constrained models," *Adv. in Phys.*, vol. 52, pp. 219–342, 2003.

[45] L. Roters, S. Lübeck, and K. D. Usadel, "Critical behavior of a traffic flow model," *Phys. Rev. E*, vol. 59, p. 2673, 1999. and comments: D. Chowdhury, J. Kertesz, K. Nagel, L. Santen, A. Schadschneider, Phys. Rev. E. **61**, 3270 (2000), L. Roters, S. Lübeck, and K. D. Usadel, Phys. Rev. E **61**, 3272 (2000).

[46] N. Boccara and H. Fuks, "Critical behaviour of a cellular automaton highway traffic model," *J. Phys. A: Math. Gen.*, vol. 33, p. 3407, 2000.

[47] S.-P. Chen and D.-W. Huang, "Noise properties in the nagel-schreckenberg traffic model," *Phys. Rev. E*, vol. 63, p. 036110, 2001.

[48] B. S. Kerner, S. L. Klenov, and D. E. Wolf, "Cellular automata approach to three-phase traffic theory," *J. Phys. A: Math. Gen.*, vol. 35, p. 9971, 2002.

[49] K. Nagel and M. Paczuski, "Emergent traffic jams," *Phys. Rev. E*, vol. 51, p. 2909, 1995.

[50] M. Gerwinski and J. Krug, "Analytic approach to the critical density in cellular automata for traffic flow," *Phys. Rev. E*, vol. 60, p. 188, 1999.

[51] S. Whitelam, L. Berthier, and J. P. Garrahan, "Dynamic criticality in glasss-forming liquids," *Phys. Rev. Lett.*, vol. 92, p. 185705, 2004.

[52] J. P. Garrahan, R. L. Jack, V. Lecomte, E. Pitard, K. van Duijvendijk, and F. van Wijland, "First-order dynamical phase transition in models of glasses: an approach based on ensembles of histories," *J. Phys. A: Math. Theor.*, vol. 42, p. 075007, 2009.

[53] M. Merolle, J. P. Garrahan, and D. Chandler, "Space-time thermodynamics of the glass transition," *PNAS*, vol. 40, p. 10837, 2005.

[54] L. Berthier, G. Biroli, J.-P. Bouchaud, and R. L. Jack, *Overview of different characterisation soft dynamic heterogeneity*, vol. 150 of *International Series of monographs on physics*, ch. 3. Oxford University Press, 2011.

[55] C. Donati, S. C. Glotzer, and P. H. Poole, "Growing spatial correlations of particle dispacements in a simulated liquid on cooling toward the glass transition," *Phys. Rev. Lett.*, vol. 82, p. 5064, 1999.

[56] C. Bennemann, C. Donati, J. Baschnagel, and S. C. Glotzer, "Growing range of correlated motion in a polymer melt on cooling towards the glass transition," *Nature*, vol. 399, p. 246, 1999.

[57] O. Dauchot, G. Marty, and G. Biroli, "Dynamical heterogeneity close to the jamming transition in a sheared granular material," *Phys. Rev. Lett.*, vol. 95, p. 265701, 2005.

[58] R. Candelier, O. Dauchot, and G. Biroli, "Building blocks of dynamical heterogeneities in dense granular media," *Phys. Rev. Lett.*, vol. 102, p. 088001, 2009.

[59] F. Lechenault, O. Dauchot, G. Biroli, and J. P. Bouchaud, "Critical scaling and heterogeneous superdiffusion across the jamming/rigidity transition of a granular glass," *Europhys. Lett.*, vol. 83, p. 46003, 2008.

[60] A. Coniglio, T. Abete, A. de Candia, E. D. Gado, and A. Fierro, "A review of the dynamical susceptibility in different complex systems," *Eur. Phys. J. Special Topics*, vol. 161, p. 45, 2008.

[61] A. M. C. Souza and L. C. Q. Vilar, "Traffic-flow cellular automaton: Order parameter and its conjugated field," *Phys. Rev. E*, vol. 80, p. 021105, 2009.

[62] M. R. Evans and T. Hanney, "Nonequilibrium statistical mechanics of the zero-range process and related models," *J. Phys. A: Math. Gen.*, vol. 38, p. 195, 2005.

[63] F. Spitzer, "Interaction of markov processes," *Adv. Math.*, vol. 5, p. 246, 1970.

[64] D. Vigil, R. Ziff, and B. Lu, "New universality class for gelation in a system with particle breakup," *Phys. Rev. B*, vol. 38, p. 942, 1988.

[65] S. Rajesh and S. Krishnamurthy, "Kang-redner small-mass anomaly in cluster-cluster aggregation," *Phys. Rev. E*, vol. 66, p. 046132, 2002.

[66] J. Kaupužs, R. Mahnke, and R. Harris, "Zero-range model of traffic flow," *Phys. Rev. E*, vol. 72, p. 056125, 2005.

[67] E. Levine, G. Ziv, and D. Mukamel, "Phase transitions in traffic models," *J. Stat. Phys.*, vol. 117, p. 819, 2004.

[68] K. Nagel, "Life times of simulated traffic jams," *Int. J. Mod. Phys. C*, vol. 5, p. 567, 1994.

[69] A. S. de Wijn, D. M. Miedema, B. Nienhuis, and P. Schall, "Criticality in dynamic arrest: Correspondence between glasses and traffic," *Phys. Rev Lett.*, vol. 109, p. 228001, 2012.

[70] R. Barlovic, A. Schadschneider, and M. Schreckenberg, "Random walk theory of jamming in a cellular automaton model for traffic flow," *J. Phys. A: Math. Gen.*, vol. 294, p. 525, 2001.

[71] F. Spaepen, "A microscopic mechanism for steady state inhomogeneous flow in metallic glasses," *Acta Met.*, vol. 25, pp. 407–415, 1977.

[72] F. Spaepen, "On the fracture morphology of metallic glasses," *Acta Met.*, vol. 23, p. 615, 1975.

[73] J. S. Langer, "Dynamics of shear-transformation zones in amorphous plasticity: Formulation in terms of an effective disorder temperature," *Phys. Rev. E*, vol. 70, p. 041502, 2004.

[74] R. Besseling, L. Isa, P. Ballesta, G. Petekidis, M. Cates, and W. Poon, "Shear banding and flow-concentration coupling in colloidal glasses," *Phys. Rev. Lett.*, vol. 105, p. 268301, 2010.

[75] A. L. Greer, Y. Q. Cheng, and E. Mad, "Shear bands in metallic glasses," *Mater. Sci. Eng. R*, vol. 74, 2013.

[76] D. Denisov, T. Dang, B. Struth, G. H. Wegdam, and P. Schall, "Resolving structural modifications of colloidal glasses by combining x-ray scattering and rheology," *Sci. Rep.*, vol. 3, p. 1631, 2013.

[77] P. Schall, D. A. Weitz, and F. Spaepen, "Structural rearrangements that govern flow in colloidal glasses," *Science*, vol. 318, pp. 1895–1899, 2007.

[78] E. R. Weeks, J. C. Crocker, A. C. Levitt, A. B. Schofield, and D. A. Weitz, "Three-dimensional direct imaging of structural relaxation near the colloidal glass transition," *Science*, vol. 287, p. 627, 2000.

[79] W. van Megen, T. C. Mortensen, S. R. Williams, and J. Müller, "Measurement of the self-intermediate scattering function of suspensions of hard spherical particles near the glass transition," *Phys. Rev. E*, vol. 58, p. 6073, 1998.

[80] J. P. Bouchaud, "Weak ergodicity breaking and aging in disordered systems," *J. Phys. I France*, vol. 2, p. 1705, 1992.

[81] V. Chikkadi, G. Wegdam, D. Bonn, B. Nienhuis, and P. Schall, "Long-range strain correlations in sheared colloidal glasses," *Phys. Rev. Lett.*, vol. 107, p. 198303, 2011.

[82] L. O. Hedges, R. L. Jack, J. P. Garrahan, and D. Chandler, "Dynamic order-disorder in atomistic models of structural glass formers," *Science*, vol. 323, p. 1309, 2009.

[83] C. Eisenmann, C. Kim, J. Mattsson, and D. A. Weitz, "Shear melting of a colloidal glass," *Phys. Rev. Lett.*, vol. 104, p. 035502, 2010.

[84] D. Denisov, T. Dang, B. Struth, G. H. Wegdam, and P. Schall, "Particle response during the yielding transition of colloidal glasses," *arXiv:1401.2106*, 2014.

[85] E. Bouchbinder and J. S. Langer, "Nonequilibrium thermodynamics of driven amorphous materials. I. internal degrees of freedom and volume deformation," *Phys. Rev. E*, vol. 80, p. 031131, 2009.

[86] R. J. Ellis and A. P. Minton, "Join the crowd," *Nature*, vol. 425, p. 27, 2003.

[87] C. Leduc, K. Padberg-Gehle, V. Varga, D. Helbing, S. Diez, and J. Howard, "Molecular crowding creates traffic jams of kinesin motors on microtubules," *Proceedings of the National Academy of Sciences*, vol. 109, no. 16, pp. 6100–6105, 2012.

[88] K. Svoboda, C. F. Schmidt, B. J. Schnapp, and S. M. Block, "Direct observation of kinesin stepping by optical trapping interferometry," *Nature*, vol. 365, p. 721, 1993.

[89] A. Yildiz, M. Tomishige, R. D. Vale, and P. R. Selvin, "Kinesin walks hand-over-hand," *Science*, vol. 303, p. 676, 2003.

[90] L. Conway, D. Wood, E. Tuzel, and J. L. Ross, "Motor transport of self-assembled cargos in crowded environments," *Proc. Natl. Acad. Sci.*, vol. 109, p. 20814, 2012.

[91] I. A. Telley, P. Bieling, and T. Surrey, "Obstacles on the microtubule reduce the processivity of kinesin-1 in a minimal in vitro system and in cell extract," *Biophysical Journal*, vol. 96, p. 3341, 2009.

[92] D. Magde, W. W. Webb, and E. Elson, "Thermodynamic fluctuations in a reacting system - measurement by fluorescence spectroscopy," *Phys. Rev. Lett.*, vol. 29, p. 705, 1972.

[93] K. Svoboda, P. P. Mitra, and S. M. Block, "Fluctuation analysis of motor protein movement and single enzyme kinetics," *Proc. Natl. Acad. Sci.*, vol. 91, p. 11782, 1994.

[94] J. W. Shaevitz, S. M. Block, and M. J. Schnitzer, "Statistical kinetics of macromolecular dynamics," *Biophysical Journal*, vol. 89, p. 2277, 2005.

[95] E. Muto, H. Sakai, and K. Kaseda, "Long-range cooperative binding of kinesin to a microtubule in the presence of ATP," *Journal of Cell Biology*, vol. 169, p. 691, 2005.

[96] P. Malgaretti, I. Pagonabarraga, and D. Frenkel, "Running faster together: Huge speed up of thermal ratchets due to hydrodynamic coupling," *Phys. Rev. Lett.*, vol. 109, p. 168101, Oct 2012.

[97] X. Pan and J. M. Scholey, "Mechanism of transport of ift particles in c. elegans cilia by the concerted action of kinesin-ii and osm-3 motors," *Journal of Cell Biology*, vol. 174, p. 1035, 2006.

[98] I. Neri, N. Kern, and A. Parmeggiani, "Modeling cytoskeletal traffic: An interplay between passive diffusion and active transport," *Phys. Rev. Lett.*, vol. 110, p. 098102, 2013.

[99] J. L. Ross, H. Shuman, E. L. F. Holzbaur, and Y. E. Goldman, "Kinesin and dynein-dynactin at intersecting microtubules: Motor density affects dynein function," *Biopysical Journal*, vol. 94, p. 3115, 2008.

[100] R. P. Erickson, S. P. Gross, and C. C. Yu, "Filament-filament switching can be regulated by separation between filaments together with cargo motor number," *PLos One*, vol. 8, p. 54298, 2013.

[101] H. W. Schroeder, A. G. Hendricks, K. Ikeda, H. Shuman, V. Rodionov, M. Ikebe, Y. E. Goldman, and E. L. Holzbaur, "Force-dependent detachment of kinesin-2 biases track switching at cytoskeletal filament intersections," *Biopysical Journal*, vol. 103, p. 48, 2012.

[102] B. Embley, A. Parmeggiani, and N. Kern, "Understanding totally asymmetric simple-exclusion-process transport on networks: Generic analysis via effective rates and explicit vertices," *Phys. Rev. E*, vol. 80, p. 041128, 2009.

[103] A. Raguin, A. Parmeggiani, and N. Kern, "Role of network junctions for the totally asymmetric simple exclusion process," *Phys. Rev. E*, vol. 88, p. 042104, 2013.

Summary

In this thesis we study collective effects in many-particle systems driven by some external force. The driving force results in large scale transport, while crowding due to frustration of the constituent particles leads to dynamic slow-down and arrest. It is this competition between driving force and crowding in the transport properties that we study for a few systems in this thesis. The driven systems under study, however, are of very different nature; we study traffic on highways, sheared colloidal glasses and molecular motors moving along the cytokeleton. The transport properties of complex driven systems is not yet understood at this point, and new methods and techniques are needed. We contribute to the understanding of driven systems by connecting fundamental interactions between particles in the different systems and developing techniques to analyze the transport properties.

We make a connection between the dynamics in traffic and glasses by comparing the fundamental interactions between particles. In both cases activity of one particle is only possible if it is not constrained by other particles nearby. This simple interaction principle lies at the origin of both the sharp increase of viscosity in glass forming liquids upon cooling and the emergence of traffic jams on crowded roads. Taking advantage of the established analogy, we apply mathematical tools developed in the glass community to traffic flow models, and numerically identify a critical point in a deterministic limit of the well-known Nagel-Schreckenberg model. Lattice models for glassy dynamics predict a similar critical point, strengthening the analogy between driven systems further. The critical point in traffic demarcates the onset of phase coexistence of free flowing and jammed traffic. Interestingly, our experimental study of colloidal glasses reveals similar phase coexistence when a critical shear force is applied. At low applied shear rates the colloidal glass flows homogeneously, while above a critical

shear rate two bands with different dynamical properties emerge. With confocal microscopy we observe the trajectories of individual particles in the colloidal glass under applied shear. Particles in the spatially separated flow bands have different translational velocities as well as different diffusion time scales. Motivated by these observations of phase coexistence in driven systems we develop an analytical criterion for the occurrence of phase coexistence in one-dimensional transport models. We analyze the size of clusters of arrested particles by quantifying the growth rates at their boundaries. In these one-dimensional models we can hence find the conditions under which a cluster can grow indefinitely and true phase coexistence occurs. We apply this criterion to the Nagel-Schreckenberg model, to analytically confirm phase coexistence in the deterministic limit.

In the last part of this thesis we study the transport properties of molecular motors moving along the cytoskeletal network. We develop a new method to extract and analyze the motion of molecular motors from microscopy experiments. The method is based on correlations of intensities from fluorescence microscopy data, and is designed to give a fast and accurate estimate of the dynamic parameters of molecular motors. Simultaneously, we measure the density of motors on a microtubule from the fluctuations in the spatially averaged intensities. Using this method we study the velocity and run length of the microtubule specific molecular motors Kinesin-1, Kinesin-II and OSM-3 as a function of motor density. At high densities, the run length of all motors significantly decreases, while the velocity seems to depend only weakly on motor density. These crowding effects start to occur at surprisingly low densities for "the lone walker" Kinesin-1, indicating a long-ranged repulsive interaction for this motor, which is known to carry cargo more or less alone. The collectively operating motors Kinesin-II and OSM-3, on the other hand, seem to have much smaller interaction lengths. Our results on all motors thus nicely fit their cellular transport function. In the final chapter we simulate the transport properties of many particles moving along complex networks and find an intriguing relation between particle density, network structure and transport current. The network structure in simulations, consisting of crossing lines in a plane, is inspired by our *in vitro* microscopy experiments where microtubules are randomly attached to a glass plate. Our approach to take simple hard-core interactions between particles, however, gives the simulations general relevance to driven systems, for example to model vehicular transport through networks of highways. While moving through the network,

particles need to choose a direction in which to continue their motion at each crossing. We find that anisotropy in the network, resulting from a preferred exit direction at crossings, leads to a density redistribution through the network. As a function of global motor density on the network, various stages of homogeneous and heterogeneous density distributions are identified. The properties and boundaries of each stage can be understood by analyzing the local flow rates.

The diversity of driven systems we encountered in this thesis is enormous, and only represents a small fraction of systems that are driven far from equilibrium. Nevertheless, one goal of studying the physics far from equilibrium is to find common underlying principles of flow and dynamic arrest that can be used to describe all those different systems. This search for universal principles is inspired by the physics of systems in equilibrium, which is understood on a general level by the theories of thermodynamics and statistical physics. The work described in this thesis gives a few insights on commonalities of driven systems, which can be used towards a general understanding. The fundamental interactions between particles already create an analogy between different systems, which can be used to transfer techniques between systems and ultimately demonstrate common behavior, such as the analogous critical point in models of glasses and traffic. We have focused on the competition between driving force and crowding effects in determining transport properties. It turns out that this competition can be understood reasonably well by comparing local flow rates. As a final remark, we note that the dimensionality of a system is important in determining how much the transport current is reduced by crowding: on a highway, cars have no escape paths upon encountering traffic jams and crowding thus does immediately reduce the transport current. Molecular motors, on the other hand, can avoid crowding by detaching from the cytoskeleton and moving through the cytoplasm. While similarly, particles in the three dimensional colloidal glasses have frustrated dynamics, but can still relax to a certain extend by collective rearrangements of particles. This rich behavior once again indicates the complexity of transport in driven systems.

Samenvatting

In dit proefschrift onderzoeken we de transport eigenschappen van verkeer op snelwegen, van gedreven colloïdale glazen en van moleculaire motoren die over het cytoskelet in biologische cellen bewegen. Deze ogenschijnlijk totaal verschillende systemen hebben gemeen dat het transport door veel "deeltjes" tegelijk wordt uitgevoerd en dat er een externe kracht of energiebron nodig is om de deeltjes gericht te verplaatsen. Door de drijvende kracht zijn zulke systemen niet in evenwicht, en daardoor nog maar slecht begrepen. De drijvende kracht doet de deeltjes in een systeem bewegen, terwijl afstotende interacties tussen de vele deeltjes de doorstroming juist verlagen. De afstotende krachten worden belangrijker naarmate de dichtheid van deeltjes hoger wordt: meer deeltjes betekent simpelweg meer interactie. Het is deze competitie tussen de drijvende kracht en de ophoping van afstotende deeltjes die de transport eigenschappen van een systeem bepalen en die wij nader bestuderen in dit werk om tot een beter begrip van gedreven systemen te komen. Hieronder volgt een korte samenvatting van onze bevindingen in ieder van de bestudeerde systemen.

Colloïdale glazen zijn dichte verzamelingen van deeltjes met micron grootte die eigenschappen van een vaste stof hebben, maar de structuur van een vloeistof. Het vaste karakter van glazen komt voort uit de afstotende krachten tussen de dicht op elkaar gepakte deeltjes. Deze afstotende krachten tussen deeltjes geven het materiaal als geheel rigiditeit. De colloïdale deeltjes bewegen echter nog wel een beetje in glazen. Door een schuifkracht op een colloïdaal glas te zetten gaan de deeltjes nog meer bewegen. Met een microscoop kunnen we de dynamica van deeltjes in 3D volgen en bepalen wanneer de externe kracht de transport eigenschappen van het colloïdale glas gaat domineren. Een sterke schuifkracht resulteert in een heterogene verdeling van stroomsnelheden: deeltjes dichtbij de plek waar de kracht wordt aangebracht bewegen snel, terwijl de deeltjes verder

weg langzaam bewegen. Men zou kunnen zeggen dat het colloïdale glas breekt boven een bepaalde schuifkracht.

Bestuurders van auto's proberen botsingen te voorkomen; dit kan men opvatten als een afstotende kracht tussen de "auto-deeltjes". De afstotende kracht op korte afstanden tussen deeltjes is analoog aan die in colloïdale glazen. Deze fundamentele interactie geeft glazen hun vaste karakter en zorgt voor de vorming van files op snelwegen. Wanneer er veel auto's op een drukke weg zijn ontstaan files die de doorstroming aanzienlijk verlagen. Wij analyseren, door verkeersmodellen analytisch en numeriek te bestuderen, wanneer files stabiel zijn en hoe groot ze kunnen worden. Alleen onder bijzondere condities, als alle fluctuaties in het rijgedrag verdwijnen en bestuurders extreem voorzichtig zijn, kan een file oneindig groot worden. Dankzij de analoge afstotende krachten in modellen voor verkeer en glazen zijn we deze bijzondere limiet op het spoor gekomen. Dit illustreert het belang van een algemene aanpak van gedreven systemen.

Tenslotte bestuderen we moleculaire motoren die vracht transporteren in biologische cellen. Deze motoren binden aan het cytoskelet, een netwerk van biopolymeren dat cellen structuur geeft. Door consumptie van ATP wandelen moleculaire motoren langs het cytoskelet en verplaatsen zo vracht van de ene naar de andere kant van de cel. Wij bestuderen het transport van moleculaire motoren zowel experimenteel als met simulaties. De simulaties leren ons hoe de netwerk structuur en de motor dichtheid de doorstroming bepalen. We nemen simpele (wederom) afstotende interacties tussen motoren aan, waardoor we grote netwerken met veel deeltjes kunnen simuleren. We vinden interessante stromingspatronen met heterogene of homogene verdelingen van motoren en stroomsnelheden, afhankelijk van de netwerk structuur en de totale motor dichtheid. Experimenteel bestuderen we de daadwerkelijke interacties tussen motoren door te observeren hoe de transport eigenschappen veranderen bij hoge motor dichtheden. Hiertoe ontwikkelen we eerst een techniek die microscopische beelden van bewegende moleculaire motoren tot hoge dichtheden kan analyseren, en bovendien snel en accuraat is. Voor het eerst meten we met deze techniek de interactie lengte tussen motoren en vinden resultaten die uitstekend in overeenstemming zijn met de specifieke rol van ieder type motor in de cel: interacties tussen coöperatief werkende moleculaire motoren blijken de nabijheid van andere motoren te tolereren, terwijl individueel werkende motoren andere motoren sterk afstoten.

Publications

- Criticality in Dynamic Arrest: Correspondence between Glasses and Traffic, A. S. de Wijn, D. M. Miedema, B. Nienhuis and P. Schall, Phys. Rev. Lett. **109**, 228001 (2012); (Chapter 4).

- Structuur in de wanorde op de snelweg, D. M. Miedema, A. S. de Wijn, B. Nienhuis and P. Schall, Nederlands Tijdschrift voor Natuurkunde (2013); written in Dutch (Chapter 4).

- Criterion for condensation in kinetically constrained one-dimensional transport models, D. M. Miedema, A. S. de Wijn and P. Schall, Phys. Rev. E **89**, 062812 (2014); (Chapter 5)

- Shear Banding of Colloidal Glasses: Observation of a Dynamic First-Order Transition, V. K. Chikkadi, D. M. Miedema, M. T. Dang, B. Nienhuis and P. Schall, Phys. Rev. Lett. **113**, 208301 (2014); (Chapter 6)

- From collective behavior to individual stepping of molecular motors, D. M. Miedema, V. S. Kushwaha, D. V. Denisov, S. Acar, B. Nienhuis, E. J. G. Peterman and P. Schall; manuscript in preparation (Chapter 7).

- Simulations of transport in random anisotropic networks, D. V. Denisov, D. M. Miedema, B. Nienhuis and P. Schall; submitted (Chapter 8).

- Free Energy of Sheared Colloidal Glasses, M. T. Dang, V. K. Chikkadi, R. Zargar, D. M. Miedema, D. Bonn, A. Zaccone, and P. Schall; submitted (not related to this thesis).

- Continuous-wave EPR at 275 GHz: Application to high-spin Fe3+ systems, G. Mathies, H. Blok, J.A.J.M. Disselhorst, P. Gast, H. van der Meer,

D.M. Miedema, R.M. Almeida, J.J.G. Moura, W.R. Hagen, E.J.J. Groenen, Journal of Magnetic Resonance, **210**, 126-132 (2011); (not related to this thesis).

Acknowledgements

The completion of this thesis comes with a feeling of pride as well as new opportunities. Here I would like to look back though, and thank all the people who have supported me over the years. First of all I would like to thank my father. Without your profound interest in science and passion to transfer this to my brother and me (our first lessons on the fundamentals of mathematics started well before we could read) this thesis would probably not have been completed or even initiated. Papa, mijn dank is groot. My first real steps in scientific research at Leiden University were supervised with great enthusiasm by Martin van Hecke. Thank you Martin, you inspired me to do more.

This thesis comprises the work I have done over the last four years at the University of Amsterdam working with many great people. Thanks to my promotores Peter and Bernard; it has been an interesting time in which I have learned a lot. Peter, you were a positive and very accessible daily supervisor, thank you for that. Together we pursued your idea to explore "the universality of dynamic arrest", which resulted in more than I could have hoped for. I always enjoyed scientific discussions with you, Bernard. Your rigorous approach to science has its beauty.

I greatly thank the post-docs Astrid and Dmitry, from which I have learned so much. Working close together makes scientific research much more fun and productive. Astrid, the few months we worked together during your time in Amsterdam were probably the most productive of my PhD. Discussing science and politics has been a great opportunity to learn from you and get to know you, Dmitry. You have been the silent power behind the soft matter group these last four years. I hope you forgive me for ruining part of that precious silence with Russian child songs.

Various experiments have been described in this thesis - none were performed by me. I greatly acknowledge the people who provided me with high quality experimental data, so I could completely focus on the analysis.
Thanks to Triet and Vijay for doing the experiments on colloidal glasses. Vijay, your data was very useful - thank you for the on-line support. Working with Triet to explore the physics of colloidal glasses was a great pleasure.
Thanks to the people at AMOLF for introducing Dmitry and me to experimental biophysics. Special thanks to Magdalena Lopez and particularly Sophie Roth for teaching us the art of pipetting. Your patience is greatly appreciated and we can only blame ourselves for our lack of skills in the lab.
Great masters of biophysical experiments are Vandana and Seyda at the VU. Combining your outstanding experimental skills with our analysis and Erwin's ideas and enthusiasm created a very fruitful collaboration. Thank you for the excellent data and interesting discussions.

Thanks to all the members of the soft matter group for the scientific discussions, lunches and coffee breaks. Special thanks to Henri, for spending the better part of the last four years within less than 10 meters range, and to Thanh, who stayed a true friend also after completing your PhD and moving back to Hanoi. Visiting you and your family in Vietnam was very special, I hope to see you again soon.

The Institute of Physics has been a pleasant place to work. A big thanks to the members of the PhD/post-doc council, working with you on scientific and social events has been a lot of fun. Thanks to Joost, Rita, Ineke and all others, for the non-scientific support.

A great thanks to all my friends: playing sports, having drinks and (board)gaming together provided plenty relaxing moments and is always fun. Special thanks to Fredric and Bart for being my paranimfen, and to Niels for designing the cover of this thesis. Lieve Gratia, met jou werd het leven nog veel leuker. Ik ben dankbaar voor je steun de afgelopen maanden.

Most of all I would like to thank my family for their unconditional and unlimited support. Growing up (and getting old) in such a warm and loving environment gives me so much strength. Arthur, jij hebt me door de moeilijkste periode van de afgelopen vier jaar heen getrokken, dat zal ik nooit vergeten. Mama, je bent voor altijd in mijn hart. Dank Frederike, Linda, Céline en, nogmaals, papa - ik houd van jullie allemaal.